NOVEL NONLINEAR INTERACTIONS AND SYNCHRONIZATION DYNAMICS IN MICRO-RESONATORS

A Dissertation

Presented to the Faculty of the Graduate School

of Cornell University

in Partial Fulfillment of the Requirements for the Degree of

Doctor of Philosophy

by

Yanan Henry Wen

Aug 2015

NOVEL NONLINEAR INTERACTIONS AND SYNCHRONIZATION

DYNAMICS IN MICRO-RESONATORS

Yanan Henry Wen, Ph.D.

Cornell University 2015

This thesis investigates two systems in chip-based nonlinear optical micro-resonators.

First is the generation of broadband frequency combs through parametric four-wave mixing and the associated phenomenon of cavity soliton formation in micro-resonators. We begin by investigating the relationship between cavity soliton based modelocking and traditional saturable absorber based modelocking. We find that a saturable absorber based modelocked laser with stimulated emission gain on only one cavity mode is dynamically equivalent to a parametrically driven cavity soliton comb. We also study the phase dynamics of the cavity soliton formation process for which we derive a set of phase equations from the governing Lugiato-Lefever equation which exhibit synchronization mechanisms akin to the Kuramoto model for coupled oscillators. These equations predict that phase anti-symmetrization preceeds phase synchronization in the cavity soliton formation process and explains the origin of the pump phase offset seen in parametrically driven cavity solitons. We then extend the concept of synchronization to systems of multiple cavity soliton frequency combs. We show that cavity solitons in evanescently coupled micro-resonators can synchronize to one another, generating synchronized pulses in the time domain and frequency locked combs lines in the spectral domain.

Second is the demonstration of all-optical switching using nonlinear loss in

micro-resonators. We achieve this through two means. The first is through the stimulated Raman response of silicon. Here we fabricate a silicon micro-ring that is co-resonant with both a pump field and the anti-Stokes field of the silicon material. The presence of the pump field stimulates optical loss at the anti-Stokes field, modulating the cavity resonance across all three regimes of coupling and demonstrating a single resonance all-optical switch. Secondly we use the two-photon absorption process of highly nonlinear organic dye molecules embedded in a polymer host. We achieve nonlinear loss induced decoupling of a cavity resonance of more than 7 dB and demonstrate the on-chip nonlinear loss of 18 cm/GW of the organic polymer.

BIOGRAPHICAL SKETCH

My first memories are of walking down dirt roads and sitting against thatch fencing in the small village in which I grew up in rural China. My parents had gone abroad to study and to make a new life for us in the West and I stayed behind with my grandparents. I was told that they were scientists and that my father was pursuing a Ph.D. (Bo-Shi), the highest degree that could be awarded to a person. He was the first in his village to go to college let alone go overseas. I was very proud of them, though I had no memory of them. I finally joined them in the United States when I was 7 years old. I remember the days before my father's Ph.D. defense. He was nervous and I was nervous with him.

When I was 12 I read Stephen Hawking's "A Brief History of Time". That book baptised my mind with the weirdness of relativity and quantum mechanics and visions of wormholes and the big bang. I saw in physics a view into the true nature of things, a peek beyond the veil of mundane familiarity. The appetite for the profound eventually carried me into the Engineering Physics program at Cornell University and into the field of optical physics: the study of light. It began with an introductory course to Laser & Photonics, followed by two research internships working on optical microscopy and optical trapping. I remained at Cornell for my Ph.D., attracted by the fascinating optical devices created by Alexander Gaeta's Quantum and Nonlinear Optics group.

Half-way through my Ph.D. I took a fateful trip to warm sunny Ghana where I fell for a Chinese-American girl in a African dress. I eventually got her to marry me and join me in bitter cold Ithaca, certainly my greatest achievement. Iris and I are now in Oxford, UK where she is pursing an MBA and I a post-doc. After my nearly 10 years at Cornell the departure is bittersweet, Ithaca has become a home and a community and Cornell truly my alma mater.

To the Light that shines in dark places. And to Iris, through whom the Light

does shine.

ACKNOWLEDGEMENTS

First I thank the maker of the light which I have been privileged to study. Secondly I thank Moses and James Clerk Maxwell for writing this down in the respective ways in which it was revealed to them: "In the beginning, God created the heavens and the earth. Now the earth was without form and void, and darkness was over the face of the deep. And the Spirit of God was hovering over the face of the waters. And God said,

$$\nabla \cdot \mathbf{E} = \frac{\rho}{\epsilon_0}, \tag{1}$$

$$\nabla \cdot \mathbf{B} = 0, \tag{2}$$

$$\nabla \times \mathbf{E} = \frac{-\partial \mathbf{B}}{\partial t}, \tag{3}$$

$$\nabla \times \mathbf{B} = \mu_0 \left(\mathbf{J} + \epsilon_0 \frac{-\partial \mathbf{E}}{\partial t} \right), \tag{4}$$

and there was light [1, 2]." I also thank Albert Einstein for making clear to us how central light is to the very fabric of the universe: it is neither space or time, but the speed of light which is absolute. To the Creator and Redeemer of all things, all praise, honor and glory. To the great prophets of faith and science, my deepest honor and respect.

I thank my mother and my father for instilling in me an appreciation for science and hardwork. They struggled out of humble origins in rural China to bring me to a place of opportunity and in the process became capable scientists themselves. They sacrificed for many years to allow me to take advantage of these opportunities. Thank you mom and dad, there have been some hard years behind us but I trust that better days are ahead.

I thank my doctoral advisor, Prof. Alexander Gaeta, for giving me a chance to be a part of your world-class research group, for opportunities to learn, grow and rise to the occasion. Alex, I especially thank for those keys words of praise

when I rose to the occasion with good science and also of rebuke when I fell short of my best. I thank you for your humility and approachability in the way you go about your science. Along with my advisor I also thank the rest of my committee: Prof. Michal Lipson and Prof. BenDaniel. Michal, I'm grateful for your comments of appreciation and encouragement early in my Ph.D. they helped me build a early sense of confidence. Also I'm grateful for your can-do attitude, which I take away with me. Prof. BenDaniel for your example as physicist in the world of entrepreneurship, I've learned a great deal from your class.

I thank my group members past and present for their companionship in the lab and help along the way. I feel particularly indebted to Dr. Onur Kuzucu who was my first supervising post-doc and who left behind several good ideas which eventually became my first two papers. I'm deeply grateful to Dr. Yoshit-omo Okawachi for his tireless management of the day-to-day affairs of the lab and help along the way. I thank Dr. Michael Lamont, who's simulations both inspired and enabled much of my work on frequency comb and cavity soliton formation. I also thank all the fantastic collaborators with whom I've had the privilege to work, especially Joel Hales, Sei-Hum Jang, Joseph Perry, Taige Hou, Austin Griffiths, Lian-Wee Luo, Isabel Kloumann and Steven Strogatz.

I thank the countless friends that have walked with me throughout the years: In Florida, Lawrence, Mike, Dan, Andrew, Glenn, Richard, Dat & Leah, Dan & Rhoda, and especially Ying-Yuan & Chai-Li who first told me about the Light. In Ithaca, Dave & Eileen, Stan & Allison, Ray & Gretchen, J.W. & Stephanie, Chuck & Ann, Edith and the countless friends from the Chinese Bible Study and other fellowships, especially Ronny, Shawn, Mike, Ray, Behzad and Larry. And, our church family from Corning and Watkins Glens, The Hinterburgers,

TABLE OF CONTENTS

LIST OF FIGURES

CHAPTER 1

INTRODUCTION

Optical resonators enable the modern telecommunications infrastructure and have key applications in sensing and detection[3], precision time-keeping [4, 5], and defense [5, 6]. Recently we have witnessed the miniaturization of optical resonators through the power of nanofabrication, leading to new dynamics, and enabling new architectures and applications [8, 9]. The reduced volume of the devices enables nonlinear effects at much lower pump powers than possible in bulk resonators enabling a wide range of new scientific and technological applications [10]. My doctoral research can be divided into two major parts, the first is the development of nonlinear loss-based optical switching in micro-resonators and the second is the investigation of phase synchronization and cavity soliton dynamics in micro-resonator frequency combs. With the help of hindsight it seems appropriate to present the latter part first and the former part second.

1.1 How I became involved with micro-resonator frequency combs

In 2011 our group showed that broadband phase-locked frequency combs states appeared to exist stably inside silicon nitride micro-rings that were parametrically driven by a narrow linewidth and phase stable pump field [10]. However single pulse states could not be generated repeatably. It is well known that single pulses can be generated in modelocked lasers which require a saturable

absorption [11] but it was not clear how modelocked pulses could be generated in a parametric oscillator without a saturable absorber.

I became personally interested in combs during this time and, inspired by saturable absorber modelocked laser, I proposed that we introduce a saturable absorber (graphene evanescently coupled to the cavity) to induce modelocking in the microresonator combs. Around the same time our research group, and later other groups, demonstrated modelocking in silicon nitride microresonators without a saturable absorber [12, 13]. Though at first a surprise, it was quickly realized that this self-stable pulsing behavior was made possible by the formation of cavity solitons, a coherently driven localized structure akin to the classic nonlinear Schrodinger soliton but generalized to include gain and loss. Cavity solitons had already been observed in parametrically driven fiber-cavity systems [14] and now in micro-resonators.

However, many facets of the comb dynamics remained unclear such as 1) the relation between type I (natural mode spacing) and type II (multiple mode spacing) combs, 2) the role of chaotics states in soliton formation, 3) the observation of a pump phase offset and of phase steps between various parts of the comb spectra and 4) the formation dynamics of cavity solitons. In addition there was the existing literature on cavity solitons which predicted that many cavity solitons can co-exist in the same cavity and have complex interactions with each other, effects which had not been considered in microresonators.

Between 2011 and the spring 2013 I was not actively involved in frequency comb research but kept an interested ear open to the exciting developments in this field. My curiosity was piqued again in March 2013 when I came across a seemingly unrelated paper on the synchronization dynamics of power-grid networks wherein a network of power stations with non-identical oscillations

2

of their A.C. voltages would spontaneously phase synchronized for a specific range of system parameters. It turns out that various types systems of coupled oscillator ranging from populations of fireflies to arrays of coupled Josephson junctions to neural networks and chemical oscillators [15, 16] all exhibited similar synchronization dynamics and which are all described by a set of equations known as the Kuramoto model. In all these systems oscillators with similar but unequal resonant frequencies could phase-lock to one another in a fairly abrupt fashion if their mutual coupling was stronger than a certain threshold. I could not fail to notice the profound similarities between the phase-locking phenomena occurring in the combs and those described in other systems throughout nature.

With the encouragement and guidance of my advisor Prof. Alexander Gaeta and help from Prof. Steven Strogatz, Michael Lamont and Isabel Kloumann I proceeded on an analytical investigation of the phase dynamics of the modelocking process. This led to the derivation of a set of phase equations from the Lugiato-Lefever equation which provided a link between synchronization theory and cavity soliton modelocking, among other interesting results. As the synchronization work came to fruition two new ideas arose, the first regarding the relation between saturable absorber modelocking in lasers and cavity soliton modelocking in OPOs, and the second regarding the interaction and synchronization of multiple cavity soliton frequency combs. These two ideas have become two additional chapters of this thesis.

I'm very proud and humbled to present this work as the bulk of my thesis, especially as it was not my originally assigned area of research. Rather it came about through a chance encounter, some seemingly wild conjectures, timely guidance and a good bit of persistence.
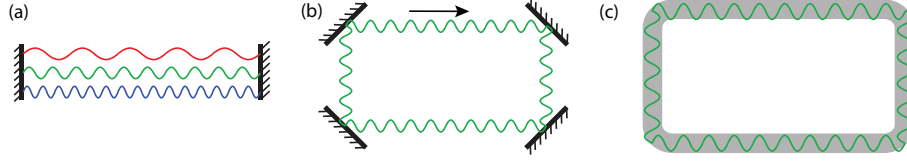
Figure 1.1: Conceptual schematic of (a) a standing wave optical cavity and (b) a travelling wave optical cavity. (c) a waveguide travelling wave cavity. The mirrors/waveguide impose a boundary condition on the electro-magnetic field for beam paths along the optical axis of the cavity allowing only wavelengths which are integer fractions of the cavity length to propagate.

1.2   Optical cavities and resonators

An optical resonator is formed by highly reflective boundary conditions along an optically confined axis which discretizes the modes of the eletromagnetic field inside the cavity volume. These boundary conditions require that the electric field parallel to the boundary and the magnetic field perpendicular to the boundary be null. Generally, this boundary condition can have an arbitrary geometry, though technologically interesting cavities typically have geometries that are mathematically tractable such as rectangular boxes, cylinders, spheres or toroids [7]. We are specifically interested in cavities that are single mode in the two transverse directions and have a periodic boundary condition in the longitudinal direction resulting in a comb of travelling wave modes (Fig.1.1), which includes all waveguide and fiber cavities (Fig.1.1c). The transverse spatial mode profiles have been solved for many waveguide geometries of interest and will not be developed in this work [21].
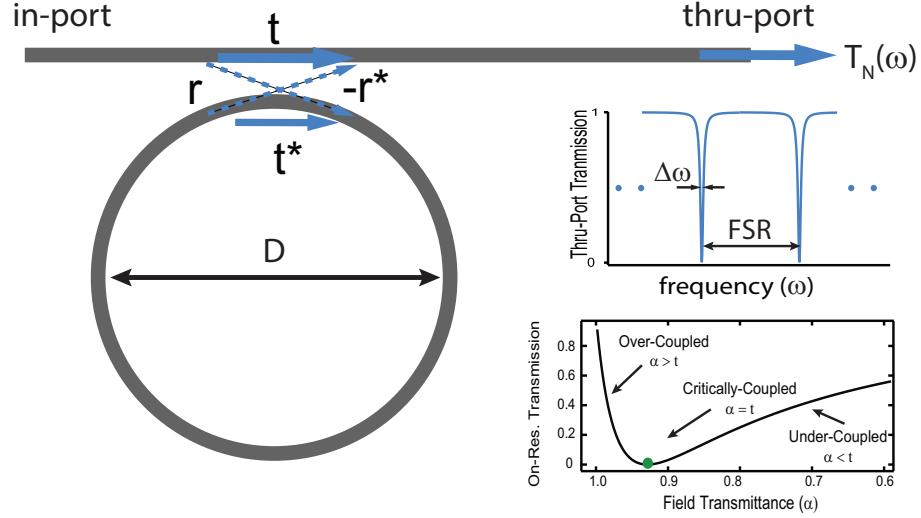
Figure 1.2: Ring-resonator cavity coupled to a bus waveguide. The coupling region can be considered an asymmetric beam splitter with reflection and transmission coefficients r and t. (inset-top) Through-port transmission reveals cavity resonances with a free spectral range (FSR) related to the cavity diameter D and resonance linewidth related to the intra-cavity loss. (inset-bottom) The on-resonance transmission shows that the transmission of a resonant field can be tuned between full extinction to full transmission by adjusting the intra-cavity loss

1.2.1 Micro-ring resonators

Micro-ring resonators are a type of toroidal waveguided travelling wave optical cavity with cavity lengths typically between 50 μm and 1 mm and guiding is achieved through index contrast total internal reflection between the waveguide material and the cladding material. Such micro-resonators have been applied to modulators [22, 23], routers [24], optical delays [25, 26], detectors [27] and recently to FWM based multiple-wavelength sources [28] and frequency combs [10].

This type of microresonator has been demonstrate in a variety of material platforms and all can be described by a general model defined by the cavity

length L, the effective intra-cavity loss $a(\omega)$ and refractive index $n(\omega)$, and external coupling t. The through-port transmission spectra can be modelled by considering a signal delivered through the bus waveguide to the cavity. The coupling region can be modelled as an asymmetric beam splitter with field amplitude transmissivity t_1 and reflectivity $r_1 = i\sqrt{1 - t_1^2}$. Following the analysis in [20] we obtain the normalized through-port intensity transmission for the signal.

$$T_N = \frac{t^2 - 2te^{-a(\omega)L/2}cos(\phi(\omega)) + e^{-a(\omega)L}}{1 - 2te^{-a(\omega)L/2}cos(\phi(\omega)) + t^2e^{-a(\omega)L}}, \tag{1.1}$$

where $a(\omega)$ is the loss coefficient and $\phi(\omega) = n(\omega)\omega L/c$ is round-trip phase, respectively, for a cavity of length L, and $n(\omega)$ is the frequency dependent refractive index. Transmission on resonance ($\phi(\omega) = m2\pi$) can be solved from Eq.1.1 as a function of the waveguide coupling and the intrinsic resonator loss.

$$T_N(\omega_{\text{res}}) = \left[\frac{t - \alpha}{1 - \alpha t}\right]^2, \tag{1.2}$$

where $\alpha = e^{-a(\omega)L/2}$. We can see that the on-resonance transmission is related to the difference of the intra-cavity loss (α) and the external coupling rate (t) and can reach complete extinction when the two are exactly equal, which is referred to as critical coupling. The on-resonance transmission is plotted in Fig.1.2(c). The case when $t < \alpha$ is the undercoupled regime and $t < \alpha$ is the overcoupled regime.

Furthermore the linewidth $\Delta\omega$ of the resonance feature can be obtained by solving for the full-width at half-max frequency via the cavity phase $\phi(\omega)$ from which we can express the cavity quality factor Q. The FSR is derived from the cavity length and together with the linewidth we can express the finesse $\mathcal{F} = FSR/\Delta\omega$ of the cavity.

Parameter	symbol	expression
linewidth	$\Delta\omega(\omega)$	$2a(\omega)$
quality factor	$Q(\omega)$	$\frac{\omega}{2a(\omega)}$
free spectral range	$FSR(\omega)$	$\frac{c}{n(\omega)L}$
finesse	$\mathcal{F}(\omega)$	$\frac{c}{2n(\omega)a(\omega)L}$

Due to dispersion and frequency dependent loss in the cavity all parameters will also be frequency dependent. The nearly equidistant spacing of the cavity resonances makes micro-resonators ideal for generation of frequency combs.

1.2.2 Materials and geometries for microresonators

Micro-ring resonators have been fabricated out a large variety of materials, from silicon to lithium niobate [34, 29]. In this thesis we are mainly concerned with material platforms that are capable of generating broadband frequency combs through nonlinear wave-mixing. These include silica micro-toroids [30], silica micro-rods [31], silicon nitride micro-rings [28], calcium fluoride (CaF_2) and magnesium fluoride (MgF_2) micro-toroids [30, 32], diamond micro-rings [33] and silicon micro-rings [34](Fig.1.3).

Figure 1.3 compares the major material platforms for frequency comb generation. Each system has particular strengths and weaknesses making each better suited for certain applications. Most materials are compatible with operation in the near-IR with CaF_2, MgF_2 and silicon having extended range into the mid-IR [30, 32]. They fall into two categories based on size. The micro-rod systems have significantly larger cavity size (~1 mm) and smaller FSR (10's GHz) than the micro-ring and micro-toroid systems (~100's μm, 100's GHz). CaF_2, MgF_2

	CaF2/MgF2	Silica-Rod	Silica-μToroid	Silicon Nitride	Diamond	Silicon
Transpar-ency (µm)	0.16-8	0.2-3	0.2-3	0.4-6	1-3, 5-20	1-8
FSR (GHz)	10-50	10-50	100s	20-200	100s	130
Q Factor	~1e10	~1e8	~1e8	~1e6	~1e6	~0.5e6
n_2 (cm²/W)	1e-16	4e-16	4e-16	2.5e-15	1.3e-15	1e-13
Fab Time	~1 day	<1 min	~ 1 day	~1 day	~1 day	~1 day
Monolithic?	No	No	No	Yes	Yes	Yes
Pump wave-length (µm)	1.55, 2.45*	1.55	1.55	1.562, 1.064	1.6	2.5
Bandwidth (nm|THz)	50|5, 200|10*	50|5	1180|164	1200|128 250|55	120|14	1400|57
Power/mode (mW)	~10	>1	~1	<1	<1	<0.1
Mode-locked?	Yes* (Kippenberg)	Yes (Diddams)	No	Yes (Gaeta, Kippenberg)	No	No
Participating groups	Matsko, Maleki, Kippenberg,	Diddams	Vahala, Kippenberg	Gaeta, Lipson, Weiner, Kippenberg	Loncar	Gaeta, Lipson

Figure 1.3: Overview of microresonator based frequency combs. Blue-highlight text indicates devices with octave spanning bandwidth, red-highlighted text indicates devices that operate in the mid-IR. Of particular importance are those devices which are capable of modelocking which include CaF_2 micro-rods, silica micro-rods and silicon nitride microrings.

and silica have weaker nonlinear indices (~1e-16 cm²/W) than the other materials but compensate for this with much higher Q factors. Fabrication time is on the order of a day for most platforms with the notable exception that silica micro-rods can be fabricated with CO_2 laser thermal annealing in just minutes. Coupling to micro-rod and micro-toroid systems are still performed with tapered fiber which can not be considered monolithic. But this disadvantage can

eventually be overcome with improved fabrication development and engineering. But currently only the micro-ring systems have fully integrated coupling waveguides.

The platform with the largest generated bandwidths are silica micro-toroids and silicon nitride micro-rings, both having demonstrated octave-spanning comb spectra. Silicon nitride micro-rings, along with the fluoride micro-rods have also demonstrated soliton mode-locking, which is scientifically and technologically important. Silicon nitride's dual capacity for octave spanning spectra and soliton modelocking gives it an arguable lead over the other platforms. However, a notable advantage of the micro-rods is the much larger power-per-mode which makes external amplification and spectral broadening more feasible in these systems [13].

1.3 Frequency comb generation

A comb of optical frequencies can be generated at the resonances of a microresonator through the nonlinear optical process of four-wave mixing (FWM). A strong pump field initially generates frequency sidebands through the modulational instability (a spontaneous degenerate four-wave mixing process) which interact with the pump field and each other to generate yet more frequency sidebands through nondegenerate four-wave mixing [36]. These FWM frequencies will naturally emerge at the resonances of the cavity due to the cavity's strong enhancement of resonant frequencies and suppression of non-resonant wavelengths [28]. Due to the phase-matched nature of FWM the dispersion of the cavity becomes very important to both the dynamics of the comb formation and to its final bandwidth and stability [37].

1.3.1 Nonlinear optical effects

Four-wave mixing and other nonlinear optical processes in dielectric material arise from the anharmonic response of the bound electrons and is described by the nonlinear polarization,

$$\mathbf{P} = \epsilon_0 \left(\chi^{(1)} \mathbf{E} + \chi^{(2)} \mathbf{EE} + \chi^{(3)} \mathbf{EEE} + \cdots \right), \tag{1.3}$$

The coefficients $\chi^{(j)}$ parametrizes the strength of the interaction proportional to the jth order in the driving field $\mathbf{E}$. The second-order interaction is the strongest but exists only in non-centrosymmetric materials or geometries such as at surfaces. The largest universally present interaction is the third-order nonlinear response represented by $\chi^{(3)}$ known as the Kerr nonlinearity. The real part of $\chi^{(3)}$ is proportional to the nonlinear refractive index $n_2 = 3/8n_0 Re(\chi^{(3)})$ while the imaginary part is proportional to the two-photon absorption coefficient $\alpha_2 = 3\omega_0/4ncIm(\chi^{(3)})$. The nonlinear parameter is $\gamma = n_2\omega_0/cA_{eff}$ where A_{eff} is the effective mode area.

Following the analysis detailed in [35] the basic dynamics of four-wave mixing can be resolved from the third-order polarization by considering a field with four frequencies ω_1, ω_2, ω_3 and ω_4, $\mathbf{E} = \frac{1}{2}\hat{x} \sum_{j=1}^{4} E_j e^{i(k_j z - \omega_j t)} + c.c.$. The component at ω_4 can be expressed as,

$$P_4 = \frac{3\epsilon_0}{4} \chi^{(3)} [|E_4|^2 E_4 + (|E_1|^2 + |E_2|^2 + |E_3|^2)E)4 + 2E_1 E_2 E_3 e^{i\theta_+} + 2E_1 E_2 E_3^* e^{i\theta_-}] + \cdots, \tag{1.4}$$

The first four terms in Eq.1.4 are responsible for the self-phase and cross-phase modulation processes and are automatically phase-matched where as the last two terms are the FWM terms whose efficiency depends very sensitively on their respective phase-mismatch $\theta_+ = (k_1 + k_2 + k_3 - k_4) + (\omega_1 + \omega_2 + \omega_3 - \omega_4)$ and $\theta_- = (k_1 + k_2 - k_3 - k_4) + (\omega_1 + \omega_2 - \omega_3 - \omega_4)$. The highest efficiency occurs when the
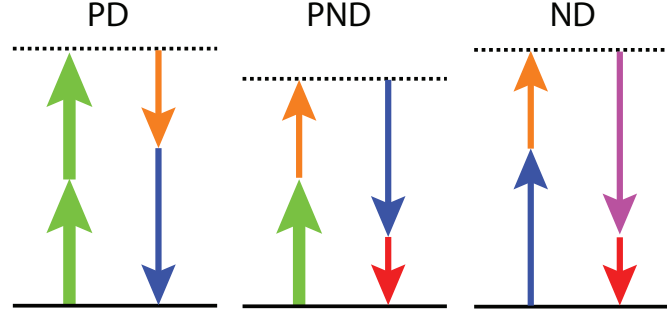
Figure 1.4: The FWM process relevant to frequency combs generation. The pump degenerate (PD) process annihilates two pump photons to generate two symmetrically sidebands. The pump non-degenerate (PND) process annihilates one pump photon and one sideband photon to generate two other sideband photons. The nondegenerate process does not involve the pump and annihilates two sideband photons and generates two different sideband photons.

phase-mismatch is zero. The first FWM term, governed by θ_+, is responsible for frequency addition processes ($\omega_4 = \omega_1 + \omega_2 + \omega_3$) such as third-harmonic generation ($\omega_1 = \omega_2 = \omega_3$). In the photon picture this corresponds to the annihilation of three photons at the pump wavelength and the creation of one photon at the third-harmonic wavelength. The second term with a phase-mismatch of θ_- corresponds to the case where two photons are annihilated at the pump wavelength and one photon each is generated at symmetric frequencies to either side of the pump, which are referred to as the signal and idler. It is this latter process that is responsible for the broadband frequency comb generation from a single strong pump field.

Figure 1.4 shows the three types of FWM (along with their time reversed processes) that are responsible for the generation of the parametric frequency comb. The first type, labeled PD for pump-degenerate, involves the annihilation of two pump photons and the creation of two sideband photons who's energies add to twice the pump photon energy. As the name suggests, this process

is degenerate in the pump. Second is the pump-nondegenerate and as the name suggests involves the annihilation of one pump photon and one non-pump photon to create two photons at the energetically appropriate sidebands. The third annihilates two non-pump photons to generate two other non-pump photons.

The phase-matched nature of FWM requires that the cavity waveguide have anomalous dispersion ($\beta_2 < 0$) for broadband frequency comb generation. It is well know from fiber soliton theory that anomalous dispersion is required in optical fibers to maintain solitons, also in modelocked laser anomalous dispersion is required for the stable existence of bright single pulse operation. In the context of micro-ring resonators the waveguide material typically has normal dispersion in the wavelength range of interest, but engineering of the waveguide geometric dispersion is sufficient to compensate for normal dispersion of the material and cause the total dispersion to be anomalous. In particular a weakly anomalous dispersion results in the broadest frequency combs [37].

Figure 1.5 shows the conceptual schematic for the generation of frequency combs in a micro-resonator. Experimentally the combs are generated by tuning the pump field into the pump resonance from the blue detuned side of the resonance. This simultaneously increases the intra-cavity pump power and decreases the pump detuning. As the intra-cavity pump power increases the first process to occur is the PD-FWM process whereby the CW pump spontaneously generates symmetric sidebands. In the time domain picture this process is referred to as the modulational instability because it is equivalent to the instability of the CW field to the exponential growth of periodic modulations. The gain spectrum of modulational instability is given by:

$$g(\Omega) = |\beta_2\Omega| \sqrt{\Omega_{MI}^2/2 - \Omega^2}. \tag{1.5}$$
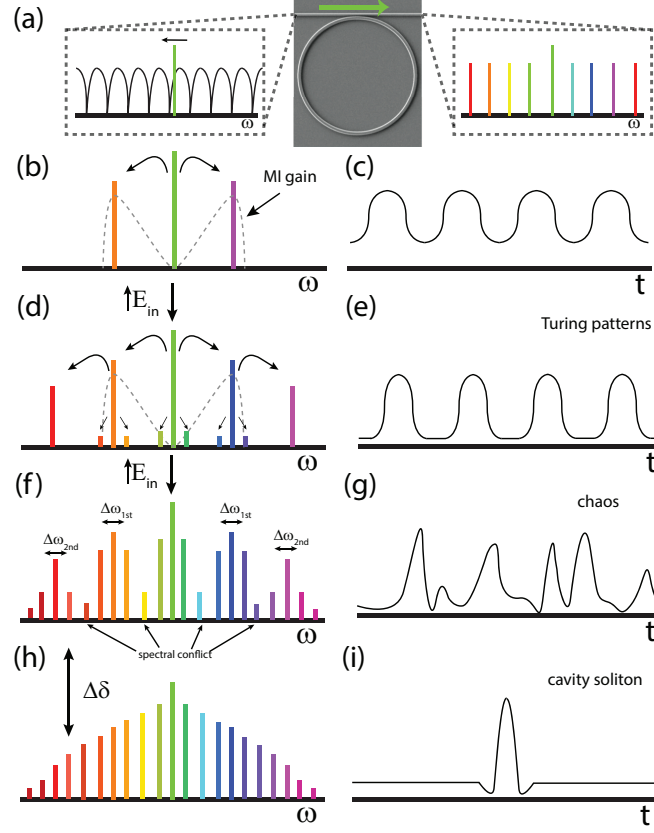
Figure 1.5: Diagram of the evolution of frequency comb generation and cavity soliton formation. (a) the schematic of the device, a single wavelength field is tuned into a cavity resonance from the blue-detuned side and generates a frequency combs through FWM. (b) The first process to occur is modulational instability which generates sidebands at the MI gain peak through PD-FWM. (c) Cascading of FWM generates more sidebands at the MI spectral separation through PND-FWM. (d) Spectral lines around the intials comb lines fill in creating mini-combs (Turing patterns in time) and encounter spectral conflict as mini-combs merge leading to chaos in time. (e) In specific parameter regimes cavity solitons can be generated.

13

where the peak MI gain occurs for $\Omega_{MI} = \sqrt{2\gamma P_0/|\beta_0|} = \sqrt{2/|\beta_0|L_{nl}}$, P_0 is the power of the CW field and $L_{nl} = \gamma P_0$ is the nonlinear length.From the expression of Ω_{MI} it can be seem that the peak of the MI gain depends on the balance between the phase shifts resulting from nonlinearity and dispersion. This balance is also at the heart of pulse formation in parametrically driven frequency combs and certain types of lasers.

The gain spectrum has the shape shown in the dotted gray curve in Figure 1.5(b) where the first sidebands are shown to emerge at the peak of the modulational instability gain. In the temporal domain this leads to modulation of the CW with a period equivalent to the number of FSRs between the pump and the first sidebands (Fig.1.5(c)). The new sidebands then mix with the pump through the PND process to generate sidebands at $2\text{x}\Omega_{MI}$. The addition of wider spectral components leads to a sharpening of the modulations into pulse-like features (Fig.1.5(d,e)). This extended modulations are commonly called Turing patterns due to their conceptual equivalence to patterns formed in chemical reactions which Alan Turing investigated as the source of spotting and stripping on animal coats [38].

As the pump is tuned yet further in the sideband closer to the main MI peaks are generated, resulting in mini-combs centered around the main MI peaks. Each mini-comb has internal phase matching of its oscillating modes but are not necessarily phase-matched to the modes of adjacent mini-comb. This results in spectral and phase conflict as the mini-combs merge, leading to chaotic behavior (Fig.1.5(f,g)) [39, 40, 41].

1.3.2 Cavity soliton formation

The spectral conflict and the associated spatiotemporal chaos can be resolved if all the comb lines are constrained to have a fixed phase relationship and equidistant frequency separations. This state corresponds to the cavity soliton regime (Fig.1.5(h,i)). Cavity solitons in parametric microresonators were first observed by tuning the pump field further into resonance, past the chaotic stage. Foster, Okawachi, Saha and co-workers first achieved this in Si_3N_4 micro-rings where they observed a sudden reshaping of the spectral profile accompanied by a drop in the RF noise of the optical intensity [10, 39, 12]. In the temporal domain they measured 200 fs pulses. Further work by Coen and co-workers [42] and Herr and co-workers [13] confirm that this was indeed cavity soliton formation.

In all cases the cavity solitons could not be directly accessed by tuning the pump power and detuning to the values appropriate for supporting cavity solitons [39, 12, 13]. The comb had to pass through a chaotic stage before cavity solitons could be observed [40]. This has recently been linked to the subcritical nature of cavity solitons [46, 43]. The pump powers that stably sustain cavity solitons are below the normal oscillation threshold and unable to generate cavity solitons directly out of the background fluctuations. Thus the system either requires seeding of the soliton formation or passage through a high intensity stage out which a pulse can be carved. The region of stability for subcritical structures greatly expands for system that exhibits bistability at the oscillation threshold [43]. This correspond to a finite blue detuning of the pump field from the cavity resonance corresponding to,

$$\frac{2\sigma}{\Delta\omega} > \sqrt{3}. \tag{1.6}$$

where σ is the frequency detuning of the pump field from the center of the cavity resonance and $\Delta\omega$ is the linewidth of the resonance.

Conceptually, cavity solitons are disspative structures that arise from the balance of nonlinearity and dispersion on the one hand and between gain and loss on the other. They are similar to conservative solitons in that they require the balance of nonlinearity and dispersion, but unlike conservative solitons which have a continuous family of solutions for given values of nonlinearity and dispersion, the additional balance of gain and loss results in a collection of fixed point solution which does not depend microscopically on the initial conditions. Whereas conservative solitons are solutions to integrable equations with analytic solutions, dissipative solitons are solutions of an non-integrable equation without an exact analytical form [44].

Specifically, cavity solitons are the parametrically driven subclass of dissipative solitons which means that the pump drives the system coherently and the system is sensitive to both the amplitude and phase of the pump field. Thus cavity solitons are a manifestion of an optical parametric oscillator whereas dissipative solitons driven by incoherent pumps, such as stimulated emission, arise in modelocked lasers. Furthermore, the cavity solitons observed in parametric microresonators are temporal cavity solitons since they are one-dimensional structures in the time domain whereas spatial cavity solitons which have transverse degrees of freedom.

The framework of dissipative structures along with bifurcation theory and stability analysis has elucidated fruitful paths for the design of laser and OPO cavities that operate in various regimes of interest, ranging from regimes that optimize stability or power of a single circulating pulse, regimes which exhibit multi-pulse interaction and bound states and regimes which exhibit spatiotem-

poral chaos [45]. Often all three categories of phenomena can be achieved in the same cavity design by tuning the pump power and frequency [46, 43]. Broadly speaking, dissipative structures are a universal concept having manifestations in biology, chemistry, physics, hydrodynamics, ecological and social systems[44]. These ideas were given a thermodynamic framework through the pioneering work of Ilya Prigogine on self-organization in systems far from equilibrium where he showed that the internal entropy of a system can decreased or equilibrated by a constant flow of energy in the system [47].

Cavity solitons were first observed in the spatial domain as localized structures in planar optical cavities [48]. In this context they were CW beams of light where the intra-cavity nonlinearity balanced diffraction. Temporal cavity solitons were first observed in a coherently driven fiber cavity by Leo and co-workers [14]. In addition to demonstrating isolated cavity solitons they were able to write and erase individual cavity solitons with an addressing laser and demonstrate the cavity as an optical buffer for 45,000 bits operating at 25 Gbits rate.

1.3.3   The Lugiato-Lefever equation

At this point its helpful to integrate all the parameters of the system (E_{in}, β_2, σ, and γ) into an equation of motion that governs the dynamics of the system. Here we use A instead of E to represent the field,

$$T_r\frac{\partial A}{\partial t} = A_{in} - [\frac{\alpha}{2} + i\delta_o]A + iL\Big[\sum_{k\geq 2}^{3}\frac{\beta_k}{k!}\Big(i\frac{\partial}{\partial \tau}\Big)^k + \gamma|A|^2\Big]A. \tag{1.7}$$

and $\alpha = \Delta\omega/FSR$ is the loss coefficient, $\delta = \sigma/FSR$ represented the pump detuning, L is the cavity length and $T_r = 1/FSR$ is the cavity round trip time. The

sum on β_k represents various orders of dispersion.

This equation was first developed by Lugiato and Lefever to describe de-localized transverse pattern formation in parametrically driven cavities and is commonly called the Lugiato Lefever equation (LLE)[49]. Evidence that parametrically driven dissipative solitons (i.e. cavity solitons) could be sustained in such a cavity without a saturable absorber was fully worked out by Barashenkov and Smirnov [50]. In the context of microresonators a detailed analysis has been done by Godey [46]. It is similar to the nonlinear Schrödinger equation (NLSE) in that it describes the time evolution of the field envelope with effects from chromatic dispersion (β_k) and the Kerr nonlinearity (γ). Unlike the NLSE it has both gain and loss which makes it a dissipative system thus nonintegrable and without analytic solutions.

Nevertheless, the equation can be accurately and efficiently solved using a split-step Fourier method as described in [35]. The method assumes that on a short enough time scale the nonlinearity and dispersion effects are separable. This means they can be separately applied in the temporal and spectral domains, respectively, with an acceptable upper bound on the error from the true evolution.

$$\hat{D} = \frac{1}{T_{rt}}\left(\frac{iL}{2}\beta_2\frac{\partial^2}{\partial T^2} - \frac{\alpha}{2} - i\delta_o + A_{in}\right), \qquad (1.8)$$

$$\hat{N} = \frac{i\gamma}{T_{rt}}|A|^2, \qquad (1.9)$$

$$A(t + dt, \tau) = e^{\hat{D}dt/2}e^{\hat{N}dt}e^{\hat{D}dt/2}A(t, \tau), \qquad (1.10)$$

where dt is typically on the order of T_{rt}. In the above implementation the dispersion operator has been symmetrically applied half way before and after the nonlinear operator. This allows the error to be reduced to third-order in the step size dt. This method has been extensively used throughout laser physics and nonlinear dynamics and recently implemented in microresonators combs

by [42, 40].

1.4   Thesis outline

This thesis focuses on three facets of the cavity soliton phenomenon in micro-resonators and on two implementations of nonlinear loss in all-optical switching using micro-resonators.

In chapter 2 we investigate the relationship between cavity soliton based modelocking and traditional saturable absorber based modelocking. The two types of systems have been largely studied independently of each other and understood through separate frameworks. We bridge this gap by numerically modelling a silicon nitride microresonator with a strong Kerr nonlinearity similar to the one described in [40, 39] driven by a narrowband laser gain rather than a coherent field. We vary the linewidth of this laser gain and observe the regimes in which solitonic pulses can be sustained. In particular we show that as the gain bandwidth is reduced below the modulational instability bandwidth that the systems enters into a modelocking regime with strong similarities to the cavity soliton regime of a parametrically driven system.

In chapter 3 we investigate the phase dynamics of the cavity soliton formation process. Much attention has been paid to the initial formation of the frequency comb, the origin of the Turing patterns, chaos, and the final stable cavity soliton state. However, there is little understanding of the dynamics as the system transitions into the soliton state and how various FWM process contribute to this transition. To achieve this goal we focus on the spectral phase. We find that a set of modal phase equations can be derived from the LLE that

are amenable to an order parameter formulation akin to the Kuramoto synchronization model of coupled oscillators. These equations provide an intuitive explaination for the pump phase offset observed in cavity solitons and also predict the dominance of PD- and PND-FWM processes in cavity soliton formation. Specifically the PD-FWM process has the effect of anti-symmetrizing the modal phases which allows the PND-FWM process to synchronize the modal phases into the cavity soliton state.

In chapter 4 We extend the ideas of synchronization to systems of multiple cavity soliton frequency combs. We find that soliton in weakly coupled microresonators can synchronize with each other to produced synchronized pulses in the time domain and phase-locked comb lines in the frequency domain. We find that the solitons attract each other with dynamics similar to the attraction of multiple solitons in the same cavity. We develop protocols for highly repeatable synchronization of multiple cavities and we test the robustness of the synchronization to a variety of perturbations. Lastly, we demonstrate interactions between multi-soliton state in two cavities and extend the synchronization protocols to systems of more than two cavities.

In chapters 5 and 6 I describe a novel approach to all-optical switching and routing using induced loss in an optical resonator towards the realization of a wavelength-selective reconfigurable (all-)optical add-drop multiplexer. The rationale is drawn from the fact that the on-resonance transmission of an optical cavity (Eq.1.2) depends sensitively on the balance between the evanescent coupling rate and the intra-cavity loss and can be tuned between full extinction to full transmission by tuning the intra-cavity loss. This approach is conceptually equivalent to the Zeno effect observed in atomic two-level systems wherein repeated measurement or decoherence can inhibit or enhance the transition rate

between levels depending on the frequency of the measurement or strength of decoherence. The traditional, and extensively studied, approach for active control of semiconductor micro-rings is by a refractive index mechanism whereas the loss-based approach has received very little attention. Additionally, the refractive approach is inherently broadband due to the broadband nature of both the free-carrier refraction and the Kerr refraction whereas its fairly straight forward to generate narrowband optical loss. Chapter 5 describes the implementation of Zeno switching using stimulated Raman loss in silicon micro-rings and chapter 6 describes the implementation using two-photon absorption in organic-silicon hybrid micro-rings.

Appendix part B provides a detailed derivation of the parametric synchronization equations described in chapter 3 from the Lugiato-Lefever equation.

CHAPTER 2

MODELOCKING REGIMES AND CAVITY SOLITON FORMATION IS LASER-GAIN DRIVEN MICRORESONATOR FREQUENCY COMBS

In this chapter our purpose is to understand the relation between saturable absorber based modelocking in lasers and cavity soliton based modelocking in parametric oscillators. In the introduction we have discussed the origins of cavity solitons in parametrically driven cavities. Below we briefly discuss the historical origins and understanding of saturable absorber based laser modelocking followed by our investigation of a saturable absorber based micro-resonator laser. We find that as the laser (stimulated emission) gain bandwidth is tuned to the width of a single resonance the system generates continues to generate a stable modelocked pulse where in the single mode acts as pump for the rest of pulse spectra in close correspondence to parametrically driven cavity soliton systems.

2.1   Modelocking and dissipative solitons in lasers

Modelocking of lasers has an extensive history with the first demonstrations in ruby and He-Ne lasers in the early 1960s [51]. Since then it has been demonstrated in various types of lasers including dye lasers, solid state lasers, semiconductor lasers and fiber lasers. Modelocking in each type of laser have developed into full fledged achieving ever shorter and stronger modelocked pulses. The chord that unifies laser modelocking is the necessity for a intra-cavity loss modulator to prefer the high intensity pulse mode over the low-intensity CW mode [11].
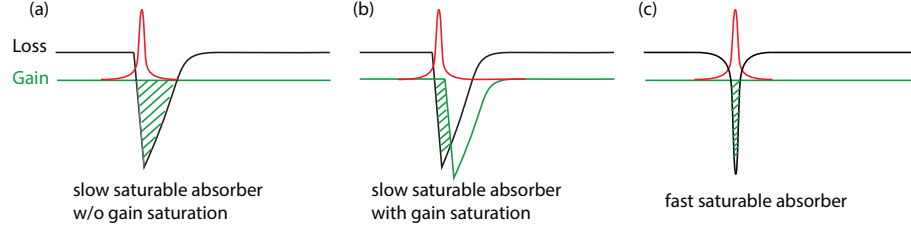
Figure 2.1: Different types of modelocking schemes. (a) Slow saturable absorbers recover slower than the pulse width of the system. In such a system the the back of the pulse is prone to instabilities unless soliton formation us strong enough to stabilize the pulse. (b) Slow saturable absorbers can also be stabilized by saturation of the gain which can shorten the net gain window. (c) Fast saturable absorbers respond instantaneously to the pulse, in which Kerr effects must be considered.

The theory of saturable absorber based modelocking was worked out most completely by Hermann Haus in a series of also now-classic papers [11]. He distinguished between the case of a slow saturable absorber wherein the response time of the saturable absorption is slower than the pulse width and a fast saturable absorber wherein the response time is faster than that of the pulse width. In both cases the resulting pulse form is a hyperbolic secant. In the case of slow SA the saturation of the gain compliments the saturation of the absorption to produce a gain window narrower than could be achieved by saturation of the absorption alone with the strict requirement that the absorber saturate more than the gain in order for this gain window to exist.

In the case of the fast saturable absorber consideration must be made for the effect of chromatic dispersion which introduces the possibility of chirp and carrier-evelope offset and the Kerr effect which leads to self-phase modulation and FWM. Haus pointed out that in the case of weak saturable absorption and anomalous dispersion the solution is chirp-free and is soliton-like (i.e. an approximate solution of the nonlinear Schrödinger equation). This distinction is

23

insightful as it makes clearer that the pulse-shaping process is not the saturable absorber, rather it is the soliton-process, namely the balance between chromatic dispersion and temporal self-phase modulation. In this case the role of the saturable absorber is to stabilize the soliton against the growth of noise and of the CW component.

However, this soliton can not be exactly a conservative soliton in the sense of being the solution to the lossless and gainless nonlinear Schrödinger equation. Similar to the cavity soliton, it is also the result of a two-dimensional balance between dispersion and nonlinearity along one axis and of gain and loss along the second axis, thus also a dissipative soliton. The concept of dissipative solitons in lasers has been extensively explored, especially in fiber lasers where various dispersion, nonlinearity and gain regimes are easier to realize than in free space cavities[45].

2.2   Cavity solitons in a laser gain driven system

The principle difference between dissipative soliton lasers and cavity soliton optical parametric oscillators(OPOs) arises from their respective gain processes. In cavity soliton OPOs the parametric pumping is a coherent process. The pump field is one of the spectral lines and the new spectral lines generated through FWM are phase-locked to the pump field and to each other. In dissipative soliton lasers the spectral lines arise from a combination of stimulated emission, which does not impose phase relations between the different spectral lines, and from FWM, which does.

While it's clear the two systems are similar it is not clear how the difference in gain process leads to different dynamics in the two systems, how the two gain

processes interact in systems that exhibit both and at what level the systems are conceptually the same and at what point they part ways. Broadly speaking we wish to understand how fundamental is their relationship by developing a unified theory that quantitatively describes both systems.

2.2.1 Laser-gain driven nonlinear Si_3N_4 micro-resonator

To that end we numerically investigate a laser-gain driven Si_3N_4 microresonator with anomalous dispersion and strong Kerr nonlinearity similar to those studied by Levy, Foster, Saha, Okawachi and co-workers [28, 10, 12, 39]. When parametrically driven this system is capable of cavity soliton formation. Stimulated emission gain could be realized in such a system through Erbium doped of silicon nitride waveguides [52, 53]. To study the interaction between parametric gain and laser gain we tune the bandwidth of the gain between the typical broadband gain of Erbium (FWHM = 30 nm @ 1550 nm), where a large number of spectral lines experience gain, to an extremely narrowband gain (FWHM < 1 nm @ 1550 nm) where only a few spectral lines at the gain center experience gain.

We find that such a system, in the presence of a sufficiently strong fast saturable absorber, is capable of modelocking for a broad range of linewidths and specifically for gain linewidths as narrow as one spectral mode. In such a case the central mode, the only mode that sees laser gain, acts as a pump field for generation of a cavity soliton-like pulse entirely through parametric gain with no help from laser gain. In fact, we find that there are two distinct modelocking regimes with respect to the gain bandwidth which are separated by the modulational instability bandwidth of the nonlinear waveguide. We find that in such
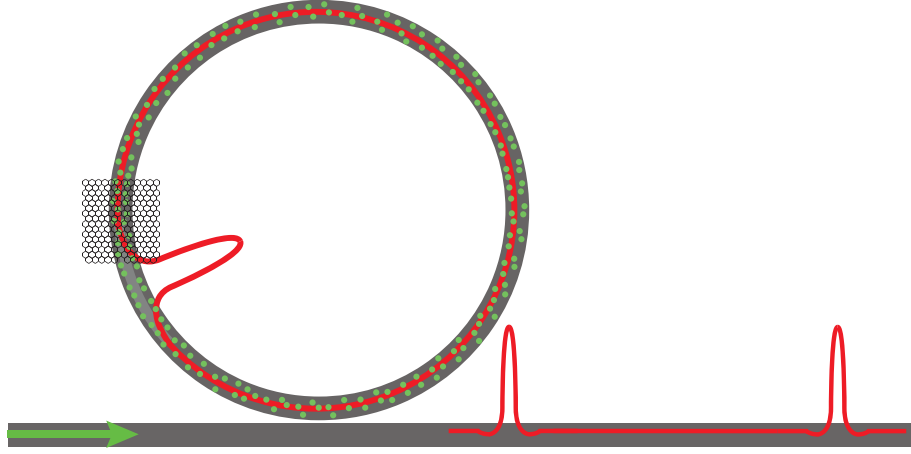
Figure 2.2: Schematic of laser-gain driven microresonator. Optical gain could be realized through erbium-doped silicon nitride waveguide, which can be optically pumped, or through integrated photodiodes which can be electrically pumped. A saturable absorber is necessary to stabilize the system against the growth of the CW component. This system is conceptually similar to erbium-fiber lasers but with a larger nonlinear parameter which enhances the cavity soliton effects.

a system cavity solitons can be generated with bandwidths far exceeding the laser gain bandwidth.

We use a dynamically symmetrized split-step Fourier method on the Lugiato-Lefever equation to model the evolution of the device shown in Fig.2.1. The waveguide material is doped with an optical gain medium and a saturable absorber is evanescently coupled to the mode of the waveguide. For the gain medium we use 5.2 cm/GW and 18 pJ for the gain coefficient and saturation energy, respectively, which are similar to that of erbium doped fiber. For the saturable absorption we use values of between a_s = 1.18-5.89 dB/cm, and 1 GW/cm^2 for the saturation intensity. As a reference, a strip of evanescently coupled single-layer graphene covering half of the top of the waveguide at a height of 1.875 μm above the waveguide center corresponds to 1.12 dB/cm of
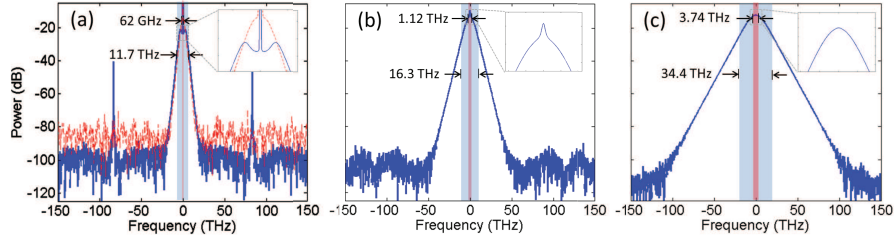
Figure 2.3: Soliton spectra for varying gain bandwidths for saturable absorption of a_s = 5.89 dB/cm. (a) δ_G = 62 GHz, only the center mode sees gain. a cavity soliton-like pulses is generated entirely from FWM. The bandwidth is simialr to that of a true cavity soliton including the strong central field. (b) δ_G = 1.12 THz, more mode see gain and the central peak merges into the main spectrum. (c) δ_G = 3.74 THz, The peak is completely smooth and system is equivalent to a dissipative soliton laser.

saturable loss whereas 3 layers of graphene covering the entirely top surface of the waveguide corresponds to 6.71 dB/cm of saturable loss. For the waveguide itself we use the nonlinearity (n_2 = 25 cm^2/GW) and dispersion (β_2 = -62.9 ps^2/km) of a Si_3N_4 microresonator similar to those demonstrated in [39] and modelled in [40].

We assume a lorentzian gain profile and vary the FWHM between 62 GHz (0.5 nm) and 3.74 THz (30 nm) and find the maximum pulse energy for which the cavity can stably support a single soliton state. Figure 2.3 shows for a_s = 5.89 dB/cm the spectral power for gain bandwidths of 62 GHz, 1.12 GHz and 3.74 THz, which result in soliton-like spectra with -10 dB bandwidths of 11.7 THz, 16.3 THz, and 34.4 THz using pump powers of 0.438 W, 5.6 W, and 12.5 W, respectively.

Closer inspection of the center of the spectrum reveals qualitatively different behaviour of the central wavelength. In the case of 62 GHz gain bandwidth, which is significantly narrower than the FSR of the cavity, only the central mode see gains. Yet a soliton-like spectra is generated that matches that of a paramet-

27

rically driven cavity soliton (PCS, dotted-red trace) at similar driving powers (0.42-0.45 W for the parametric cavity soliton). The stable presence of the strong central mode with has a close correspondence with the coherent pump of the parametric cavity soliton system. We emphasize that the rest of the soliton spectrum is generated entirely through parametric four-wave mixing without help from stimulated emission gain. We call this soliton a **laser cavity soliton** (LCS) in contrast to both the **parametric cavity soliton** (PCS) found in purely parametrically driven cavities and to the **laser dissipative soliton** (LDS) which are the modelocked pulse typically found in lasers where the stimulated emission gain is significantly wider than the modulational instability bandwidth.

Both the parametric cavity soliton and the laser cavity soliton have a strong central mode and the same spectral shape. The main deviation between the LCS and PCS spectra is in the area near the pump where in the LCS the frequencies near the central mode are depressed revealing two lobes. These lobes correspond to the modulational instability (MI) sidebands of the strong central mode. This suggests what modulational instability plays a dominant role in sustaining the transfer of power from the central mode to the rest of the soliton spectrum. As the gain bandwidth is increased more modes experiences gain and the central peak merges with the main soliton spectrum. The frequencies near the pump also fill in and the MI sidebands are no longer visible.

2.3 The OPO/CS- and laser/DS-like modelocking regimes

Figure 2.4 shows the maximum stable pulse energy as a function of the gain bandwidth for several values of the saturable absorption (a_s = 1.18 dB/cm-red,
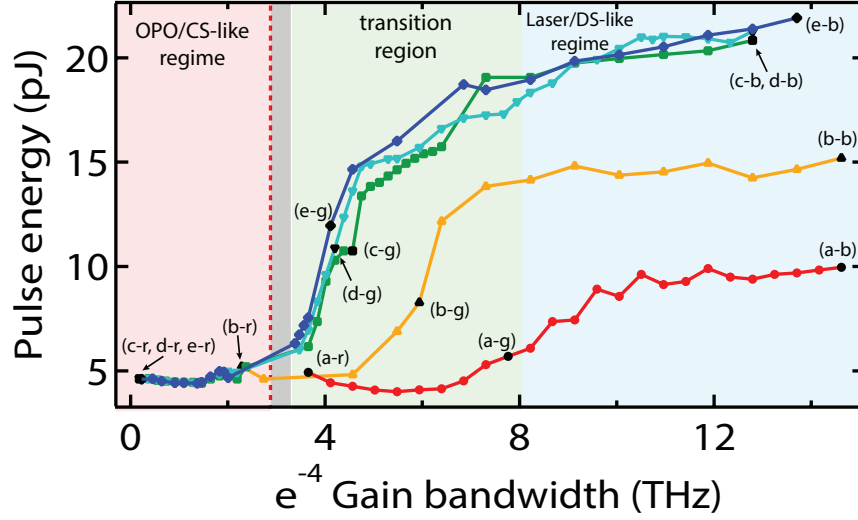
Figure 2.4: Maximum stable pulse energy with respect to gain bandwidth for several values of saturable absorption (a_s = 1.18 dB/cm-red, 3.02 dB/cm-orange, 5.24 dB/cm-green, 5.57 dB/cm-cyan, 5.89 dB/cm-blue). Red region - cavity soliton like modelocking regime where only a single or very few modes see gain thus soliton mainly generated through FWM. Gray region - region of instability where the system does not have a stable single pulse solution. Red line indicates the modulational instability bandwidth. Green region - transition region where more modes see gain and the central modes merge into main pulse spectrum. Blue region - laser-like modelocking regime where pulse formation dynamics are equivalent to disspative soliton formation.

3.02 dB/cm-orange, 5.24 dB/cm-green, 5.57 dB/cm-cyan, 5.89 dB/cm-blue). For weaker values of saturable absorption ($a_s \leq$ 3.02 dB/cm) the system loses stability for narrower gain bandwidths. But for stronger saturable absorptions ($a_s \geq$ 5.24 dB/cm) the system is stable for gain bandwidths down to a single mode.

However, even for stronger values of saturable absorptions the cavity is not continuously stable over the entire range of bandwidths. The gray region of Fig. 2.4 indicates a range of bandwidths for which the cavity has no stable solution. Inspection of the spectral power profiles in Figure 2.3 suggests that the

discontinuity is related to the interaction between the laser-gain spectra and the modulational instability gain. When the bandwidth axis is plotted for the $1/e^4$ bandwidth (Fig. 2.4) the frequency corresponding to the peak of the modulational instability bandwidth (red-dotted vertical line) falls within the region of instability. This suggests that the instability region corresponds to a regime of finite but weak gain-MI interaction. The cavity stabilizes again once the gain spectra becomes wider than the MI bandwidth where the strong central mode merges into the main pulse spectrum and the spectrum becomes identical to a traditional laser modelocked pulse (Fig.2.3b,c).

These observations suggest the existence of two distinct modelocking regimes and a transition region in between. In the regime where the gain is much less than the MI bandwidth corresponds to cavity soliton-like modelocking (red shaded region) wherein the pulse spectra is generated through optical parametric oscillation (OPO). The regime where the gain bandwidths is wider than the MI bandwidth corresponds to the more common laser modelocking regime wherein dissipative solitons (DS) are generated predominantly through stimulated emission (blue shaded region). In the OPO/CS-like regime the pulse energy has a relatively flat dependence with the gain bandwidth. Beyond the instability region the pulse energy increases rapidly with increasing gain bandwidth in a transition region and flattens out again into a positive linear dependence in the laser-like regime. The spectra in Figure 2.3 correspond to each of the three regions.

Likewise, Figure 2.5 plots the spectral power in (a-e)-i, temporal pulse form in (a-e)-ii and spectral phase in (a-e)-iii for in each of the three regions (OPO/CS like-red, transition-green, laser/DS like-blue) for each value of saturable absorption (a-1.18 dB/cm, b-3.02 dB/cm, c-5.24 dB/cm, d-5.57 dB/cm, e-5.89
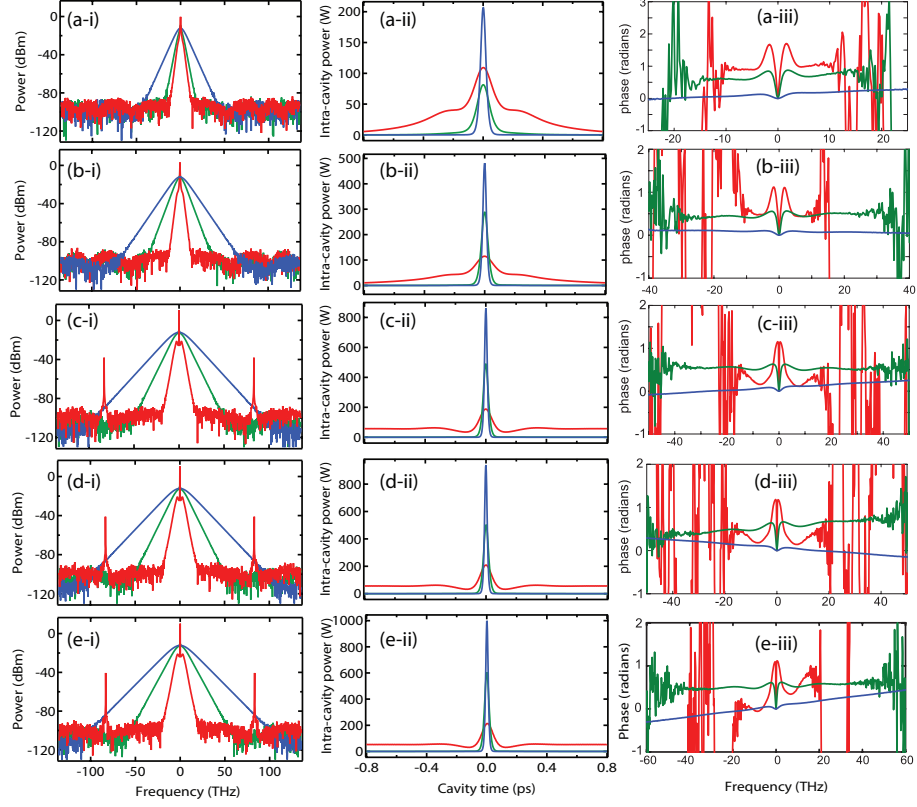
Figure 2.5: Spectral power (a-e)-i, temporal power (a-e)-ii, and spectral phase (a-e)-iii of pulses from the three regions (red, green, blue) indicated in 2.4, for different values of saturable absorption (a_s = (a) 1.18 dB/cm, (b) 3.02 dB/cm, (c) 5.24 dB/cm, (d) 5.57 dB/cm, (e) 5.89 dB/cm)

dB/cm). The phase plots are particular interesting because they show for narrow gain bandwidths a characteristic phase offset of the central mode that is very similar to that of PCS's. This phase offset is indicative of a detuning of all populated spectral modes from the center of the cavity resonance to which they belong. This is remarkable since the system is not constrained externally to have detuned modes but is self-constrained in order to achieve this CS-like state. This phase offset is reduced for broader gain bandwidths and becomes essentially flat phased for broader gain bandwidths. In the temporal domain the key observation is that for sufficiently strong saturable absorption ($a_s \geq 5.24$
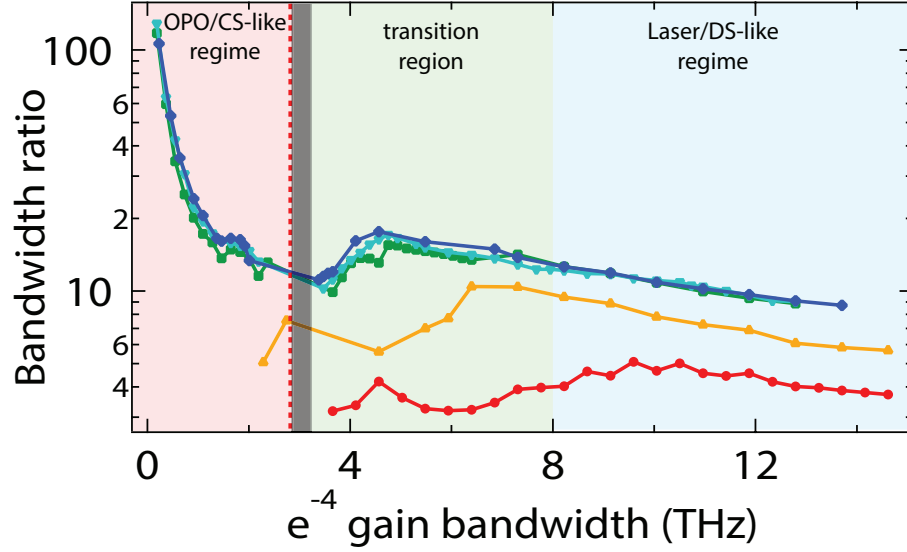
Figure 2.6: Ratio of the generated soliton bandwidth to the gain bandwidth.(a_s = 1.18 dB/cm-red, 3.02 dB/cm-orange, 5.24 dB/cm-green, 5.57 dB/cm-cyan, 5.89 dB/cm-blue). For weaker values of saturable absorption ($a_s \leq$ 3.02 dB/cm) the ratio is less than 10x. But for stronger saturable absorptions ($a_s \geq$ 5.24 dB/cm) the can be greater than 100x.

dB/cm) the narrow gain bandwidth result has a pulse form similar to that of a cavity soliton with the constant background corresponding to the central mode.

These results show the connection between traditional laser modelocking and parametric cavity soliton modelocking. They show, for the first time, that the dynamics of dissipative laser soliton systems and cavity soliton systems are qualitatively similar when the laser gain bandwidth is significantly narrower than the modulational instability bandwidth. Additionally the observation that for broader gain bandwidths the central peak merges into the main spectrum and the phase offsets flatten suggests that for narrow gain bandwidths the central modes which see greater gain serve as pump fields which generate the rest of the spectrum through parametric FWM. This also suggests that in the case of modelocked frequency combs with multiple phase offset modes, which have

been observed in parametrically driven silicon micro-rods [], the phase offset modes serve as secondary pump fields for the rest of the comb spectra.

These results show the connection between traditional laser modelocking and parametric cavity soliton modelocking. They show, for the first time, that the dynamics of dissipative laser soliton systems and cavity soliton systems are qualitatively similar when the laser gain bandwidth is significantly narrower than the modulational instability bandwidth. Additionally the observation that for broader gain bandwidths the central peak merges into the main spectrum and the phase offsets flatten suggests that for narrow gain bandwidths the central modes which see greater gain serve as pump fields which generate the rest of the spectrum through parametric FWM. This also suggests that in the case of modelocked frequency combs with multiple phase offset modes, which have been observed in parametrically driven silicon micro-rods [31], the phase offset modes serve as secondary pump fields for the rest of the comb spectra.

2.4   Ultrabroadband comb formation using narrowband gain

Lastly, we note that the resulting soliton pulse spectra (Fig.2.3) have 10 dB bandwidths exceeding 10 times the gain bandwidths. Figure 2.6 plots the ratio of the 10 dB bandwidth of the resulting solitons to the 3 dB bandwidth of the laser gain. In particular, for system which are stable in the CS-like regime the ratio increases significantly such that the soliton bandwidth is more than 100 time the gain bandwidth. This is to our knowledge the first scheme for the generation of broadband modelocked combs using ultra-narrowband laser gain. These results strongly motivate the development of laser-gain medium doped and dispersion engineered nonlinear waveguide and of sources of strong saturable absorption

as a path to realizing chip-based modelocked frequency comb generation without a coherent external pump [52, 53].

CHAPTER 3

SYNCHRONIZATION THEORY OF SOLITON MODELOCKING

In this chapter we investigate the phase dynamics of the soliton formation process in the Lugiato-Lefever equation(LLE) through the lens of self-organization. We find that phase equations derived from the LLE show that the pump-degenerate four-wave mixing (PD-FWM) and pump-nondegenerate four-wave mixing (PND-FWM) processes dominate the phase dynamics of soliton formation and display self-organization features akin to the Kuramoto model for synchronization of coupled oscillators [54], including the existence of meaningful order parameters and coherence-coupling feedback that describes the soliton formation process. These equations also predict that the pump phase is offset from the rest of the modal phase profile in the soliton state.

Additionally our analysis predicts that phase anti-symmetrization, where the phase profile becomes anti-symmetric about the pump phase, occurs before phase synchronization and soliton formation can occur. We compare the evolution of these equations to that of the full LLE system and observe a strong correspondence between the two, indicating that our model captures the dynamics leading to the cavity soliton formation process.

3.1 The Kuramoto synchronization model of coupled oscillators

A large collection of coupled oscillators with slightly different natural frequencies can undergo a transition to a phase-locked state with identical frequencies.

This phenomenon appears in many systems spanning biology, chemistry, neuroscience, and physics [54, 16]. Examples include power grid networks, neural networks, chemical oscillators, and arrays of Josephson junctions and semiconductor lasers [15, 55, 56, 57, 58]. Self-organization in such systems has been modeled by the Kuramoto model, which describes the time-evolution of the phase $\phi_p(t)$ of an oscillator p as an interaction between its natural frequency ω_p and its coupling to the phases of all the other N-1 oscillators.

The governing equations are $\dot{\phi}_p = \omega_p + \kappa \sum_m^N \sin(\phi_m - \phi_p)$, where κ is the coupling strength [16]. This model can be recast in an order-parameter formulation, where an average phase ψ and a coherence $R(t)$ are defined via $R(t)e^{i\psi} = \frac{1}{N} \sum_m^N e^{i\phi_m}$ (Fig. 3.1a,b). Then the Kuramoto model becomes $\dot{\phi}_p = \omega_p + \kappa R(t) \sin(\psi - \phi_p)$. Viewed this way, ϕ_p is no longer coupled to every individual oscillator's phase, but only to the average phase ψ. Moreover the effective strength of the coupling is proportional to the coherence R. This proportionality between coupling and coherence creates a positive feedback which, for a sufficiently large κ, gives rise to an abrupt transition in which the frequencies of a macroscopic fraction of the oscillators spontaneously synchronize.

3.2   Phase-locking in nonlinear optical cavities

In optics an alternative form of phase locking can occur in lasers and parametric oscillators between a large collection of cavity modes with nearly equidistant frequency separations. In these systems the nearest-neighbor spacing across the modes varies due to dispersion within the cavity. In the presence of nonlinearity within the cavity, the system can spontaneously modelock such that the frequency spacings between the oscillating modes become identical (Fig. 3.1c,d).
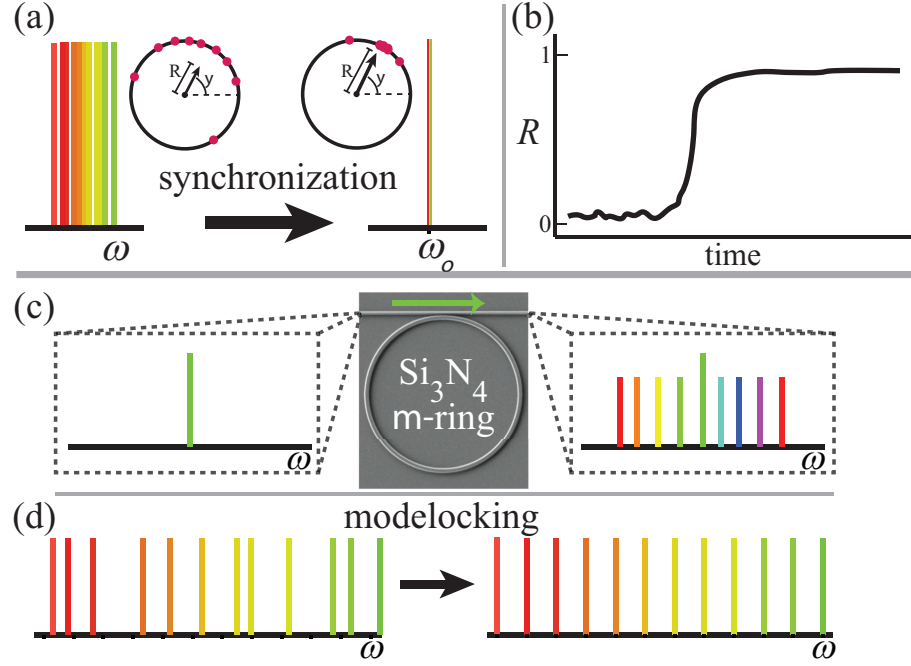
Figure 3.1: (a) Synchronization of a population of oscillators with non-equal natural frequencies to a phase-locked state with an identical frequency. A large fraction of the oscillator phases lock to ψ, the average of all phases. (b) Abrupt transition of the coherence R to synchronization. (c) CW-pumped FWM generation of broadband frequency comb in silicon nitride micro-rings. (d) Modelocking of cavity modes results in equidistant frequency spacings between adjacent modes.

This behavior has been studied extensively in the context of ultrashort pulse generation via dissipative soliton formation in lasers [11, 59] and in fiber and micro-resonator-based four-wave mixing (FWM) parametric oscillators via cavity soliton formation [12, 13].

While several theoretical [60, 61] and experimental studies [31, 62] have provided insight into the phase dynamics of the initial formation of parametric combs, no analysis exists for the phase dynamics of the soliton modelocking process. Although Kerr-based parametric frequency combs have been suggested as the most fundamental example of self-organization in nonlinear optics

[63, 14], no direct connection has been made to the concepts of synchronization and self-organization. Here we develop a theory for the phase dynamics of cavity soliton formation by deriving a set of phase equations from the Lugiato-Lefever equations which exhibit features of self-organization akin to the Kuramoto model and which elucidate several aspects of cavity soliton formation.

3.3   Phase equations from the Lugiato-Lefever equation

The governing equation of modelocked parametric frequency combs is the LLE (a damped, driven nonlinear Schrödinger equation inside a cavity) with periodic boundary conditions [42]:

$$T_r\frac{\partial A}{\partial t} = A_{in} - [\frac{\alpha}{2} + i\delta_o]A + iL\Big[\sum_{k\geq2}^{3}\frac{\beta_k}{k!}\Big(i\frac{\partial}{\partial\tau}\Big)^k + \gamma|A|^2\Big]A. \tag{3.1}$$

Here A is the intra-cavity field, t and τ are the slow and fast times of the system, respectively, A_{in} is the pump field coupled into the cavity at frequency $\omega_0 + \delta_o$ where δ_o is the detuning of the pump field from the center of the cavity resonance, β_k are dispersion coefficients, γ is the nonlinear coefficient, α represents the total linear loss per round trip of the cavity of length L, and $T_r = L/v_g$ is the round trip time. We consider the intra-cavity field as a sum of the discrete cavity modes and define a phase $\phi_p(t)$ for each mode at the frequency corresponding to the equidistant comb defined by the detuned pump field such that $A(t, \tau) = \sum_p^{N+1} A_p e^{i(\omega_p + \delta_o - \omega_0)t - i(\Omega_p - \Omega_0)\tau} e^{i\phi_p(t)}$. By letting the pump mode index $p_0 = 0$, where N is even and $-N/2 \leq p \leq N/2$, the slow and fast frequencies of the field become $\omega_p = 2\pi v_g p/L + \omega_0$ and $\Omega_p = 2\pi v_g p/L + \Omega_0$, where ω_0 and Ω_0 denote the frequencies at the center of the pump resonance and v_g is the corresponding group velocity. For a sufficiently strong pump field $A_{in}(t, \tau) = A_0 e^{i(\phi_0 + \delta_o t)}$ with appropri-

ate cavity detuning δ_o and constant phase ϕ_0, a broadband comb of frequencies is generated near the modes of the cavity (Fig.3.1c). After an initial build-up period, the amplitudes of the cavity modes reach a near constant state, thus we are able to neglect the amplitude variations of the modes and consider only the phases. By employing a slowly varying envelope approximation for the total intra-cavity field and normalized dispersion coefficients $\xi_k = (2\pi v_g/L)^k v_g \beta_k$, we derive the following general dynamical phase equation from the LLE, with time dependency of the phases made implicit:

$$\dot{\phi}_p = \frac{\xi_2}{2}p^2 + \frac{\xi_3}{3}p^3 - \Gamma \sum_{l,m,n=-N/2}^{N/2} \mathcal{A}_{mp}^{ln} \cos(\phi_l - \phi_m + \phi_n - \phi_p), \qquad (3.2)$$

where $\Gamma = \gamma L/T_r$ and $\mathcal{A}_{mp}^{ln} = A_l A_m A_n / A_p$. This equation has functional similarities to the Kuramoto model wherein each optical mode can be considered an individual oscillator. The spread in natural frequencies of the oscillators is represented by the second- and third-order dispersion terms in the right-hand side, while the nonlinear term gives rise to the coupling among oscillators in the last term in the right-hand side.

3.4 The parametric synchronization equations

In the absence of a strong pump mode, this equation has no stable solutions. The cosine coupling term has an equilibrium point at $\pi/2$, which results in the phase mismatch for various FWM processes being pulled to this value. However, this condition cannot be simultaneously satisfied for all combinations of modes. For a pump η times stronger than an average comb (non-pump) mode, the coupling term can be decomposed, via the amplitude factor $\mathcal{A}_{mp}^{ln}$, into 4 categories of processes with relative strengths η^2, η, 1, η^{-1}. In our analysis we

keep only the largest coupling terms that scale as η^2 and η. The terms that scale as η^2 are a result of the pump-degenerate (PD) FWM processes, where two pump photons are annihilated to create a photon pair at modes symmetric about the pump mode. Alternatively, the terms that scale as η are due to the pump-nondegenerate (PND) FWM processes, in which one pump photon and one comb photon are annihilated and create two photons at the energetically appropriate modes. Under this approximation we find that the most natural variables to describe the system are not the individual phases ϕ_p of the modes, but rather the phase average and difference for pairs of modes symmetric about the pump mode, that is $\bar{\phi}_p = (\phi_p + \phi_{-p})/2$ and $\theta_p = (\phi_p - \phi_{-p})/2p$, respectively.

We transform to this basis and obtain the following pair of equations, which we term the parametric synchronization equations (PSE):

$$\dot{\bar{\phi}}_p = \frac{\xi_2}{2}p^2 - 2\Gamma\eta^2 A_c^2 \cos[2(\phi_0 - \bar{\phi}_p)] - \Gamma\eta A_c^2 N_o R(t) \cos(\phi_0 - \bar{\phi}_p) \cos[p(\theta_p - \theta_o)] \quad (3.3)$$

$$\dot{\theta}_p = \frac{\xi_3}{3}p^2 - \frac{2\Gamma\eta A_c^2 N_o}{p} R(t) \sin(\phi_0 - \bar{\phi}_p) \sin[p(\theta_p - \theta_o)], \quad (3.4)$$

where we have made the simplifying assumption that modes $-N_o/2$ to $N_o/2$ have amplitude $A_c = A_0/\eta$ and all other modes have zero amplitude. In this transformed basis, the symmetric character of the system is separated from the anti-symmetric character. The phase-average equation describes the symmetric behavior of the system while the phase-difference equation describes its anti-symmetric behavior. The pump-degenerate processes manifest themselves only in the phase-average equation as the second term on the right-hand side of Eq.(3.3). The pump-nondegenerate processes have both symmetric and anti-symmetric contributions and appear as the last terms in the phase-average and

phase-difference equations. $R(t)$ and $\theta_o(t)$ represent the order parameters of the systems and are given by $R(t) = \frac{2}{N_o} | \sum_{m=1}^{N_o/2} e^{im(\theta_m - \theta_o)} |$ and $\theta_o(t) = \frac{8}{N_o^2} \sum_{m=1}^{N_o/2} m\theta_m$. Here θ_o is the normalized average phase difference. It serves the same role as the average phase ψ in the Kuramoto model. It also measures the linear slope of the phase profile which yields a translation of the temporal pulse profile along the cavity length. $R(t)$ is the coherence; it measures the extent to which the population of the phase differences, θ_m, aligns to the average phase difference θ_o. The triple sum reduces to a single sum since the PND term is only a single sum and the phase-average and phase-difference parameters are separable due to the phase symmetry induced by the PD term.

We consider the evolution of the PSE system by introducing an initially random phase profile into the equations. Since the PD term scales as η^2 it initially dominates the dynamics, and its presence in the phase-average equation has the effect of anti-symmetrizing the phase profile about the pump phase ϕ_0. The PND term does not initially play a role since the coherence $R(t)$ is zero due to the initially random phases and since it is inherently η/N_o times smaller than the PD terms. Eventually anti-symmetrization of the phases occurs and the coherence becomes non-zero, which allows the PND terms to become non-negligible. This has the effect of synchronizing all the normalized phase differences to their average. This results in a near-linear spectral phase profile, which is consistent with evolution to a cavity soliton as predicted by the LLE model and illustrates its connection to self-organization behavior. Thus, the PD term entrains the phase averages to a fixed input phase, and the PND term employs the coherence-coupling feedback to self-organize around a non-fixed normalized average phase difference. We numerically model the temporal evolution of the PSE and the full LLE systems using systems parameters presented in [40]

41
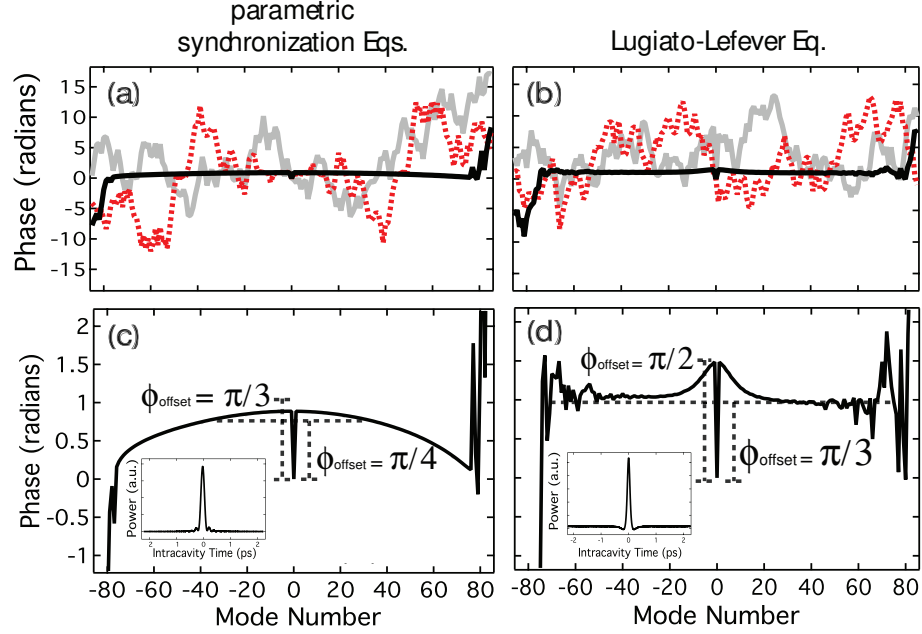
Figure 3.2: (a,b) Three stages of evolution of the phase profile of the intra-cavity field as predicted by (a) the parametric synchronization equations (PSE) and (b) the Lugiato-Lefever equation (LLE): The grey curves represent the initial random phase profile. The red-dotted curves show the phase evolution after 370 (PSE), 308 (LLE) round trips; the phase profiles in both models illustrate the anti-symmetrization of the spectral phase due to the pump degenerate FWM processes. The black curves show the final phase profile after 3394 (both) round trips in which the phases have become completely synchronized, which is a result of the pump non-degenerate terms. In addition, a slight offset of the phase of the pump from the phases of the other cavity modes is observed. (c,d) The final spectral phase profiles of the PSE and LLE systems showing deviations from a pure linear profile, including the pump phase offsets. (insets) Temporal pulse shapes of the PSE and LLE.

and verify this prediction through the selected phase profiles in Fig. 3.2(a,b). Both models show the progression from initially random phase profiles to an anti-symmetric profile and finally to a fully synchronized profile. We find that synchronization in the PSE is only stable for $185 > N_o > 155$. Choosing the most stable $N_o = 170$ results in the synchronization of 152 modes, in close correspondence to the LLE where 155 modes are synchronized. Conceptually, synchronization of a nearly equidistant multimode distribution of oscillators can also be appropriately called a form of optical syncopation.

3.5   The pump phase offset

One of the notable features of the LLE cavity soliton phase profile is a static offset of the pump phase from the rest of the phase profile and have recently been measured by Del'Haye and co-workers. As it is a static offset it cannot be explained by time-constant phase shifts such as the pump field detuning, self-phase modulation or cross-phase modulation, rather it must be a result of certain FWM phase matching conditions. This pump phase offset is also predicted by the PSEs in which it is a explicit result of the co-sinusoidal dependence of the PD term and arises directly from the real nature of the FWM process. In order for this term to act as a restoring force on the phase averages, as in the Kuramoto model, it must have a sinusoidal dependence on the phase averages. Thus the PSE show that the pump phase offset is fundamentally related to the stability of the phase averages. The PD term only entrains the phase averages to the pump phase and no self-organization has yet occurred.

We compare in detail the synchronized spectral phase profiles in Fig. 3.2(c,d). Both systems stabilize to a broadband phase-locked state with an off-

set of the pump phase from the rest of the phase profile. Due to the factor of 2 in the argument of the PD term, this offset should be $0 < \phi_{offset} < \pi/2$ and centered at $\pi/4$ in order for the cosine to have a significant sine-like contribution. Both the PSE and the LLE predict pump phase offsets within these bounds. The LLE system has a slightly larger pump phase offset due to self-phase and pump-induced cross-phase modulation effects which were not accounted for in the PSE. This is, to our knowledge, the first theoretical prediction and explanation of the origin of the pump phase offset of the soliton-modelocked states in a parametric frequency comb. We confirm in Fig. 3.2(c,d insets) that the broadband phase-locked state results in a solitary pulse in the time domain. The exact pulse shape for the PSE is not quantitatively meaningful since all the modes have equal amplitude resulting in a Sinc-like pulse without a CW background.

3.6 Phase symmetry and coherence

The evolution of the order parameters confirm the validity of the two conjectures: 1) amplitude dynamics are, to first order, neglible and 2) the PD-FWM processes anti-symmetrize the phases prior to the onset of phase synchronization. Figure 3.3(a,b) compares the evolution of the the coherence and the normalized average phase difference in the PSE and LLE systems. Despite slight quantitative differences, both systems exhibit abrupt transitions from a disordered state to an ordered state as indicated by the sharp rise and subsequent stabilization of the coherence. The normalized average phase difference also exhibits dynamical similarities in the initial rapid increase and subsequent decline and stabilization to a constant value. Closer inspection of the two parameters (insets) reveal relaxation behavior on the order of 1 ns, close to the cavity lifetime
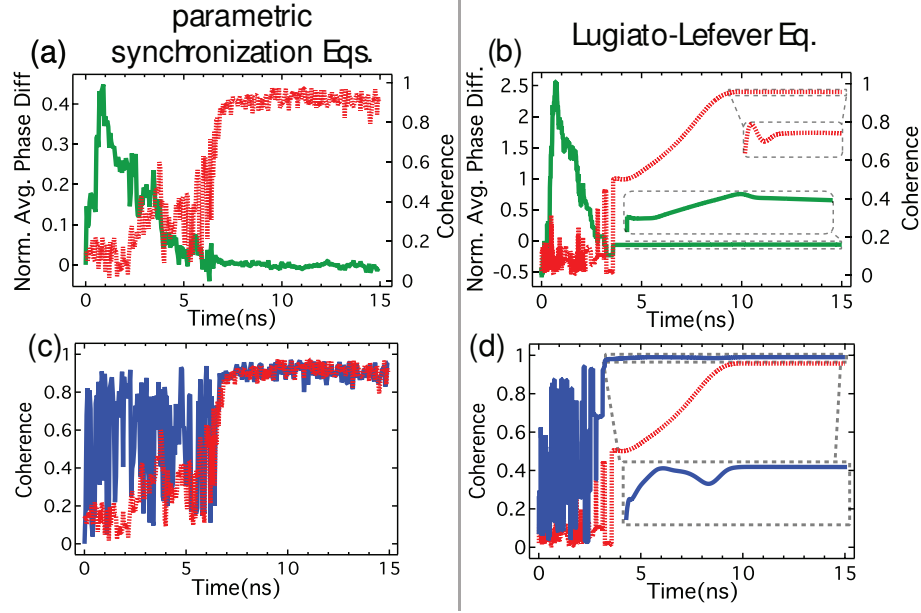
Figure 3.3: (a, b) Coherence R (red-dotted) and normalized average phase difference θ_o (green). An abrupt transition to a stable phase-synchronized state is observed in both systems. (c, d) Coherence R (red-dotted) and phase symmetry R_{sym} (blue). The close macroscopic correspondence indicates that PD- and PND-FWM process dominate the pahse transition dynamics. The noisiness of the PSE signal indicates that the ND-FWM, which are not included in the PSE, act to damp out fluctuations.

of 1.42 ns. The remarkable quantitative similarity of dynamics indicates that the cavity soliton formation process is truly dominated by phase rather than amplitude dynamics.Furthermore, figure 3.4 plots the coherence for the PSE for values of $N_o = 140$ (blue), 170 (red), and 200 (orange), showing that the synchronization is only stable for 185> N_o >155. For $N_o = 170$ the PSE result in 152 synchronized modes. The close correspondence to the LLE with 155 synchronized modes indicates that the PSE synchronization bandwidth, just as the LLE cavity soliton bandwidth, depends on the balance of disorder and coupling and not simply constrained to N or N_o. Next we consider the phase symmetry of the two systems as quantified by $R_{asym} = \frac{2}{N_o}|\sum_{m=1}^{N_o/2} e^{i(\bar{\phi}_m - \phi_0)}|$. This value is a mea-

sure of the extent to which the phase profile is anti-symmetric about the pump phase and is equivalent to a coherence of the phase averages. Figure 3.3(c,d) compares the coherence and the phase anti-symmetry for the two systems. In both systems phase anti-symmetry occurs before coherence is achieved, and the coherence cannot grow until the phase anti-symmetry has reached a high value. This confirms our initial prediction that the PD term must anti-symmetrize the phase profile before the PND term can synchronize the phases to a near linear profile. These dynamics are only observed in cavity soliton formation and not observed in the Turing pattern states or chaotic states. Furthermore, the phase symmetry does not fully stabilize until the coherence has reached a high value, and in turn, the coherence does not stabilize until the phase symmetry has fully stabilized. These results illustrate the necessity of phase anti-symmetrization to precede phase synchronization in soliton formation and the complex interplay between phase symmetry and phase coherence. Additionally, the remarkable correspondence between the LLE dynamics and the PSE dynamics indicate that the simplification taken to obtain the PSE retains the majority of the phase dynamics.

3.7   Role of chaotic states of soliton formation

Lastly, the phase evolution modeled in the LLE is the stage after it evolves from the chaotic state and enters a soliton state. Passage through a chaotic state has been suggested as necessary for soliton modelocking to occur [40, 64]. This has been linked to the subcritical nature of cavity solitons in they exist for pump powers for which the system is bistable. Below threshold it must compete with the flat homogeneous solution while above threshold Turing patterns typically
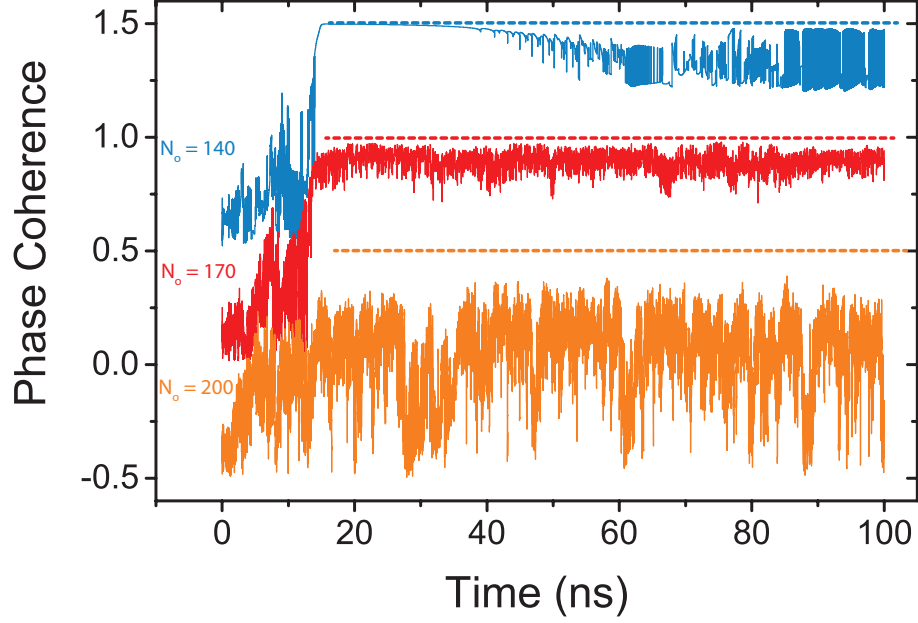
Figure 3.4: Phase coherence of the PSE for values of N_o = 140-blue, 170-red, 200-orange indicating that the PSE is only stable for a small range of values 185> N_o >155. For N_o =170 results in 152 synchronized modes in close correspondence to the LLE with 155 synchronized modes.

dominate. This means the comb lines which contribute to the cavity soliton can not have arbitrarity small amplitudes and must be "excited" by a seed pulse or through a preexisting pulse in the cavity such as chaotic spikes [46, 43].

From the phase-matching point of view the chaotic stage is necessary in soliton formation for the purpose of randomizing the phase profile to prevent Turing pattern and mini-comb-related FWM processes from dominating the phase matching of the comb [60, 13]. Turing states and the associated mini-combs have phase profiles that inherently lack global symmetry about the pump phase and thus cannot directly enter into a soliton state.

CHAPTER 4

SYNCHRONIZATION OF MULTIPLE PARAMETRIC FREQUENCY COMBS

The concept of many-body interactions and synchronization can be extended from the phase-locking of spectral lines in single microresonator comb to the coupling and synchronization of solitons between multiple microresonator combs. Synchronization of modelocked laser cavities have been demonstrated in both solid state- and fiber-based systems and has been important to applications such as time resolved spectroscopy [17], coherent combination of laser beams and few cycle pulse generation [65]. However the majority of these demonstrations were achieved using either active feedback or in a master-slave scheme.

The coupling of mutually-synchronized parametrically-driven cavities have not been explored and could exhibit dynamics not available with coupled laser-gain driven system. Additionally, implementation on a chip-based platform could enable scalable systems with topologies unfeasible with bulk cavities such as synchronized pulse sources for on-chip time-resolved nonlinear spectroscopy [17, 19]. Configured in a long-distance fiber-coupled arrangement, such a system can provide an integrate solution for synchronization and stabilization of atomic clocks [18].

We theoretically investigate systems of two and three evanescently-coupled microresonators under conditions in which parametric frequency combs are being generated in each microresonator. We observe that each system can exhibit passive, stable synchronization of their intra-cavity fields which results in time-locked pulses in the temporal domain and frequency and phase-locked comb lines in the spectral domain. We find the coupling threshold for synchroniza-
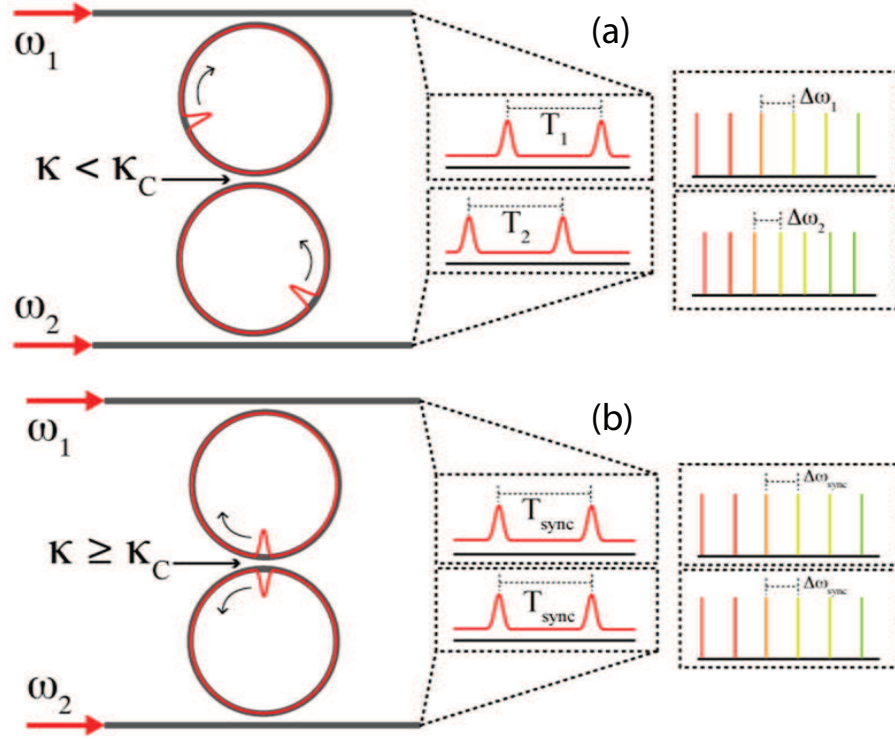
Figure 4.1: Schematic of evanescently coupled microresonators. (a) For coupling κ less than κ_c the critical inter-cavity coupling rate, the solitons cannot synchronize to each other. (b) For inter-cavity coupling κ greater than κ_c, the solitons are able to synchronize to each other if they are within a certain time delay of each other, resulting in synchronized pulses in the time domain and phase-locked comb lines in the frequency domain.

tion to occur and develop protocols for achieving this synchronization with high repeatability. Finally we study the robustness of the synchronization to perturbations.

4.1 Soliton interactions in nonlinear cavities

In certain regimes cavity solitons in single microresonators can interact with each other in complex ways such as attraction, repulsion, collision and fusion of two or more solitons and the formation of stable multi-soliton bound states (soliton molecules). Also, certain regimes of operation mimic condensation and precipitation phenomena where solitons emerge spontaneously out of a noisy background but are eventually condense into a bound state of many solitons [45].

Of particular interest to this thesis are the attractive interactions between two or more solitons. It's reasonable to surmise that solitons in coupled microresonators would also attract each other. Akhmediev and co-workers [66] showed that in the case of a laser-gain driven, saturable absorber stabilized, dissipative soliton system, that two solitons can either form a bound state or undergo soliton fusion depending on their initial relative phase and temporal distance.

Parametrically-driven systems without saturable absorption also exhibit both multi-soliton bound states and pair-wise soliton fusion. Barashenkov and co-workers [50] showed that the parametrically-driven NLSE exhibits stable complexes of two and more solitons but who's phase relation now depends also on the ratio of the strength of the parametric drive and the strength of damping. Alternatively, Clerc and co-workers [67] showed that "coalescence" (i.e. fusion) of pair-wise solitons occur in a variety of parametrically-driven systems including vertically chain of pendula, magnetic wires and troughs of Newtonian fluid. However, a general description similar to that of Akhmediev and co-workers encompassing both the fusion and bound state regimes, to the best of my knowledge, has not been performed for parametrically driven cavities.

Such a unifiying analysis would be a valuable contribution to the field of cavity soliton dynamics.

Nevertheless, Clerc and co-workers, using the dimensionless LLE, were able to develop the following soliton pair interaction law which shows that interaction for a pair of in-phase solitons is overdamped.

$$\dot{\Delta} \approx -\mathcal{R}\sigma e^{-\delta\Delta}, \tag{4.1}$$

where $\mathcal{R}$ represents the interaction strength between the two solitons which for large interaction distances simplifies to $\mathcal{R} = 8\delta^3/\mu$ where δ represents the amplitude of the solitons, and μ is the damping rate. The factor σ is the relatively polarity of the two soliton, $\sigma = 1$ for in-phase solitons and $\sigma = -1$ for out-of-phase solitons. Out of phase solitons will repel until their interactions becomes neglible whereas in-phase solitons will attract and their distance decrease monotonically. In particular they show this decrease is logarithmic as a function of the instantaneous delay between the two solitons.

$$\Delta(\tau) \approx \frac{1}{\delta}ln[\delta\mathcal{R}(\tau_0 - \tau)], \tag{4.2}$$

where $\tau_0 = \rho e^{\delta\Delta_0(\tau=0)}/\delta R$ is the initial time delay between the two solitons corresponding to the initial distance $\Delta_0(\tau = 0)$.

These results can be directly extended to the interaction between two solitons in two linearly coupled cavities since the the attraction strength $\mathcal{R}$ has a simple dependence on the amplitude of the participating solitons δ. The linear coupling of the two cavities suggests that the attraction between the two solitons will be qualitatively identical but the strength reduced by the cavity-cavity coupling rate.

4.2 Synchronization of evanescently coupled cavities

We first consider the geometry shown in Fig.4.1 with two silicon nitride microresonators with waveguide cross-sections and dispersion profiles according to [37] that are evanescently coupled weakly such that coupling does not induce splitting of degenerate modes. We first consider the case where cavity-A has a stable single soliton state achieved through the protocol detailed in [40], and we seek to generate a single soliton in cavity-B that is synchronized to that in cavity-A.

We find that this can be achieved with near 100% repeatability through a two-stage protocol wherein cavity-B is first pumped into a brief chaotic stage followed by reduction of the pump-B power to a level consistent with the single soliton regime. The coupled field of cavity-A seeds the formation of a synchronized soliton in cavity-B as it transitions from the chaotic regime into the soliton regime. Figure 4.2(a,b) show the temporal evolution of both cavities where the initial chaotic stage lasts 500 ps and the coupling coefficient is 0.04%. We find for pump power of 450 mW in the single soliton regime the cavities must have a field coupling coefficient of at least 0.02% in order for the synchronization to occur consistently. A field coupling of 0.01% led to synchronized soliton formation 16 times in a series of 50 trials (32%) whereas 0.02% resulted in synchronization 50 out of 50 times. This lower bound on the coupling rate appears to be set by the quantum noise amplitude which is equivalent to 0.001% of the intra-cavity coupled amplitude. For coupling coefficients greater than 0.1% the dynamics of cavity-A become significantly affected during the initial chaotic stage and the synchronization process. This leads to greater susceptibility to perturbations. Figures 1(c) plots the synchronization success rate as a function of the coupling
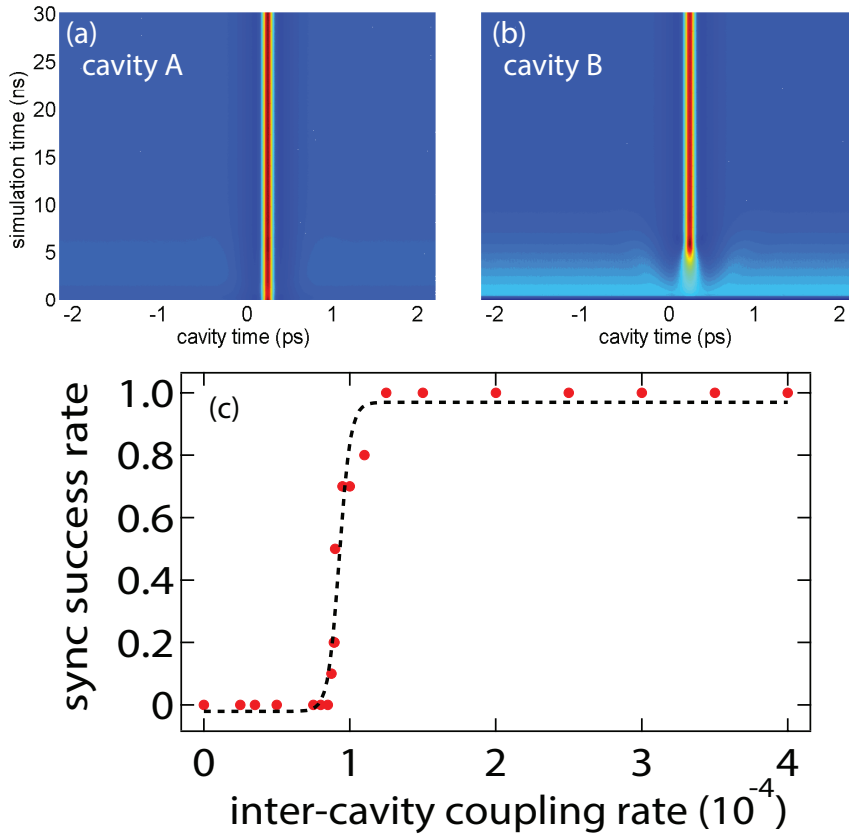
Figure 4.2: Success Rate of repeatability with respect to the coupling rate κ. The critical coupling rate is determined to be $\kappa_c = $ 1e-4. Below the critical inter-cavity coupling

coefficient.

4.3 Robustness to perturbations I: Temporal offset

Next we investigate the robustness of the synchronization to three types of perturbations: 1) a single large temporal translation of one soliton with respect to the other, which tests the maximum temporal reach of the soliton-soliton interaction and gives the upper-bound on the timing offsets from which the system can be expected to recover; 2) a random temporal walk of the two solitons with
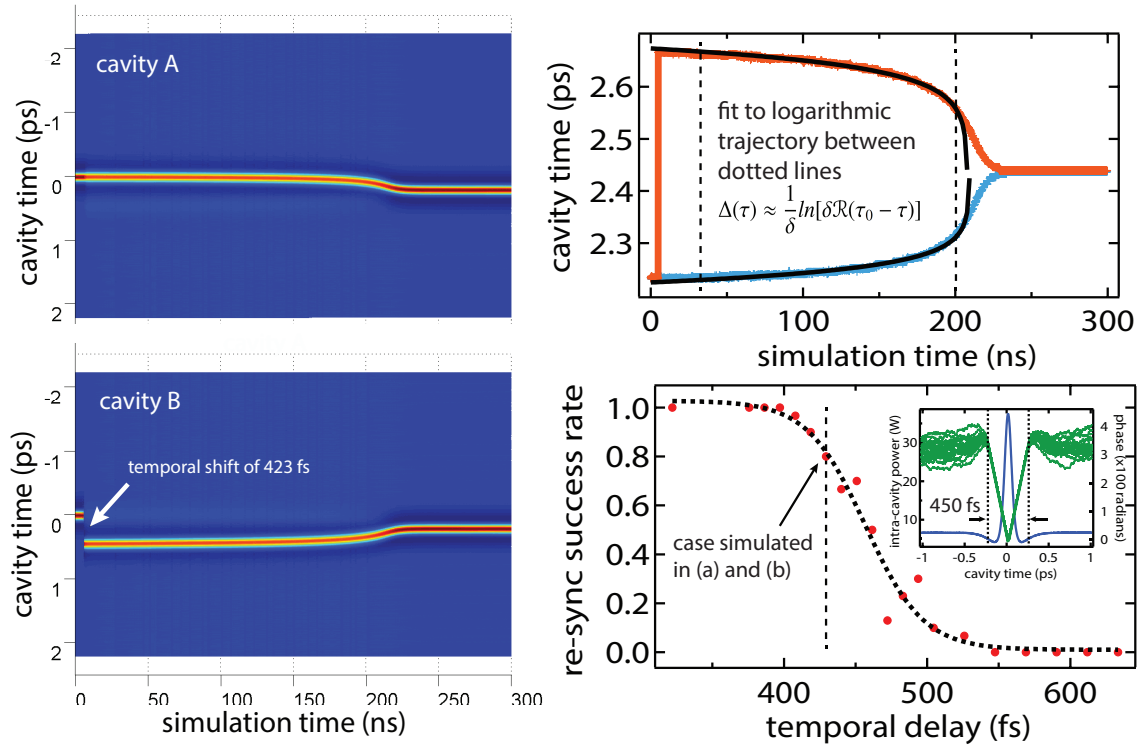
Figure 4.3: Resynchronization of solitons after sudden time delay. (a,b) The temporal evolution of two initially synchronized solitons offset by 423 fs. (c) Trajectory of the soliton peaks (soliton A-blue, soliton B-orange). Black curves are the fit of the logarithmic trajectories from [67]. (d) The resynchronization success rate as a function of the temporal delay.

respect to one another, which models timing jitter due to dynamics noise sources such as pump field noise and shows the ability of the coupled-cavity system to reduce the overall noise of the system; and 3) a steady temporal shift of one soliton with respect to the other, which models variations in static parameters between the two cavities such as the FSR, group-velocity or pump detuning.

In the first case we begin with two initially synchronized solitons-, A and B in cavities-A and -B. We shift soliton-B by a time $\Delta\tau$ and observe the evolution of the system over the next 300 ns. We find that the two solitons are able to resynchronize themselves for translations less a delay of the solitons which

54

is defined by the width of the trapping potential given by the temporal phase profile of the solitons and which also corresponds to the temporal translation for which we get 50% resynchronization success. We term this value $\Delta\tau_0$ the interaction delay. For the solitons in consideration the interaction delay is $\Delta\tau_0$ = 450 fs. This phenomenon is consistent with previous reports that solitons can be trapped and stabilized to the maxima of the temporal phase profile [68, 69]. Figure 4.3(a,b) shows the evolution of the systems in response to a time delay of soliton-B of 423 fs, which has a success rate of 80%. Figure 4.3(c) shows a fit of the logarithmic trajectory for the pair-wise interaction predicted by Clerc and co-workers which is valid for the majority of the interaction but deviates as the solitons finally fuse. In part (d) the inset is plotted the resynchronization success rate for various delays in units of the soliton pulse FWHM τ_0. The interaction delay corresponds to 3.5 times the FWHM.

4.4 Robustness to perturbations II: dynamic noise and long distance coupling

To model the dynamic noise we introduce a random temporal walk of the two solitons with respect to each other which can be quantified as timing jitter corresponding to a frequency ω_{tj} = 50 MHz. Every round-trip each soliton take a $\pm 1/\omega_{tj}$ shift with 50% chance either way. Figure 4.4 plots the dependence of the inter-soliton drift (i.e. the distance between the two initially synchronized solitons) after 50 ns of evolution under the influence of this dynamic noise. The plot has two parts. The shaded region shows the effect of the coupling strength
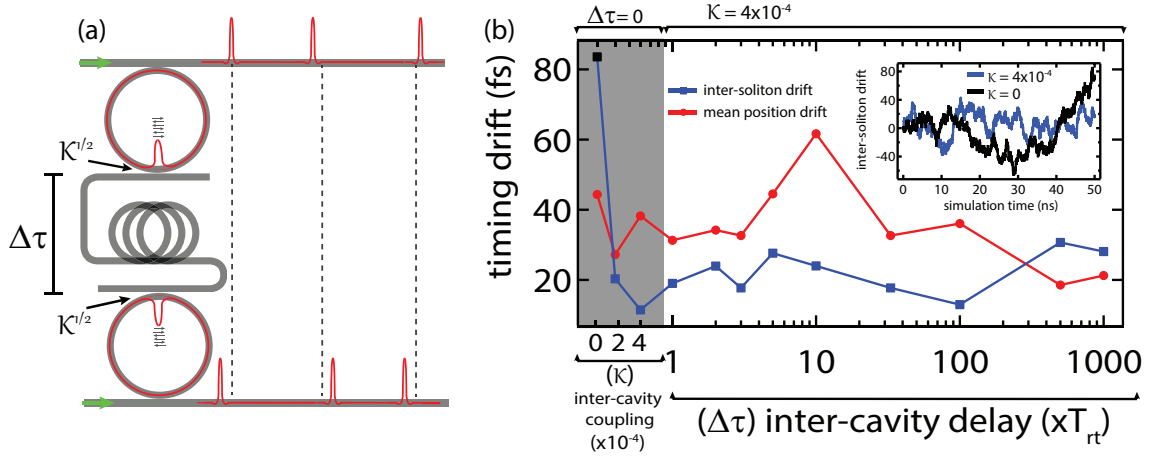
Figure 4.4: Effect of inter-cavity coupling and inter-cavity delay on dynamic noise. (a) (shaded region) Inter-soliton timing drift of two solitons perturbed by random walks of their temporal location in the cavity. Coupling of 4e-4 reduces the average inter-soliton drift a factor of 4. (unshaded region) Timing drift as a function of inter-cavity delay. Inter-soliton drift suffers no degradation. The mean position drift appears to be enhanced for certain time delays ($10 \times T_{rt}$) but is unenhanced for shorter and longer delays. (inset) Temporal evolution of the inter-soliton drift two zero coupling and 4e-4 coupling. The coupled drift value is constrained close to zero.

on the inter-soliton timing drift. For no coupling the timing inter-soliton drift is on average (for 10 trials) greater than 80 fs. For coupling strength $\kappa \geq 2$ the drift is reduced significantly, to below 20 fs.

The unshaded region of Figure 4.4 plots the timing drift with respect to a fixed temporal delay between the two cavity. This temporal delay models two cavities that are far apart from each other and coupled through a length of optical fiber. The inter-cavity delay is given in units of the cavity round trip time. The inter-soliton drift reduction is maintained for temporally delayed cavities and does not degrade as the delay is increased. The red curve plots the drift of the mean position of the two solitons. The coupling does not constrain this degree of freedom however there is some indication that this drift may be en-
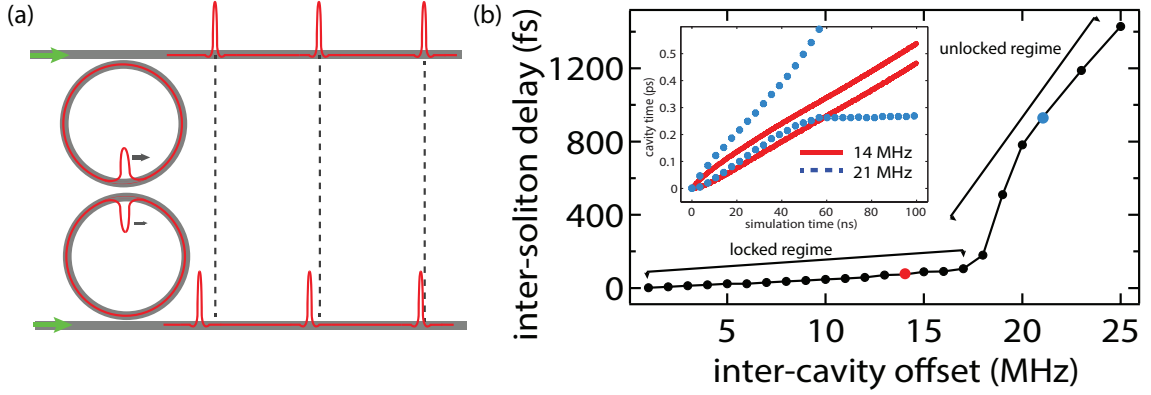
Figure 4.5: Inter-solion delay as a function of the inter-cavity frequency offset. Solitons are able to remain locked for offsets up to 17 MHz but diverge for higher offsets. (inset) Comparison of temporal evolution of soliton peaks for offset of 14 MHz (red-solid) and for 21 MHz (blue-dotted)

hanced for delays around 10 (xT_{rt}) which may be due the fact that the coupling preserves the effect of random fluctuations for more than one round trip of the cavity. This apparent enhancement is an interesting topic for further investigation. However this effect does not persist for longer or shorter time delays.

4.5 Robustness to perturbations III: FSR, group velocity and pump frequency offsets

To model a frequency offset between the two cavities we introduce a small translation every round trip to soliton-B, which can arise from several experimental parameters such a difference between the FSRs of the two cavities, a difference between the pump wavelength a difference in the group velocities of the two cavities or a combination of all three. The result in the time domain is a offset in
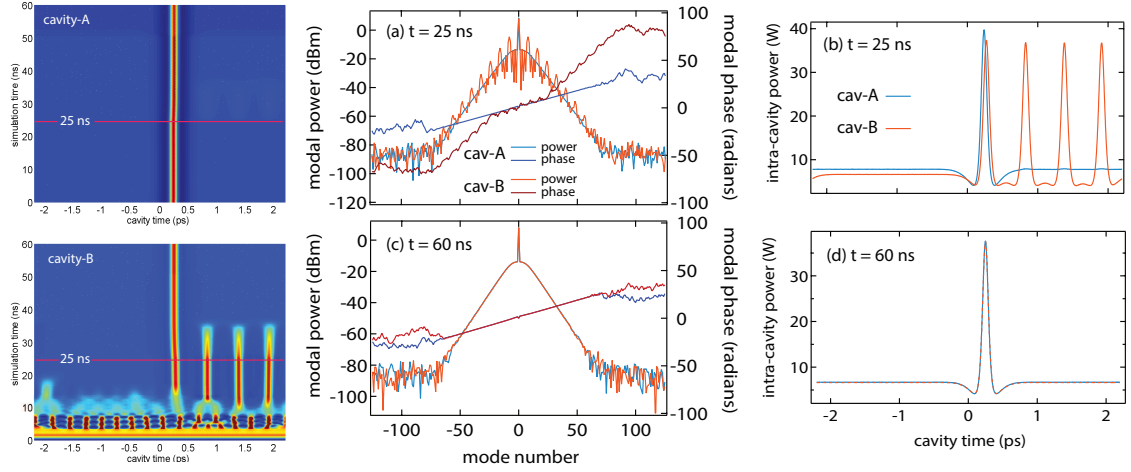
Figure 4.6: Demonstration of pulse selection interaction. Cavity-B undergoes a soliton generation protocol which results in a stable 4 soliton state. At 25 ns the it is coupled to cavity-A which has a single soliton state. The interaction selects the left most soliton in cavity-A and suppresses the other solitons.

the round-trip time of the two cavities leading to unsynchronized pulses (Fig. 4.5(a)). Figure 4.5(b) shows the inter-soliton distance after 100 ns of propagation as a function of the frequency detuning between the two cavities. For total frequency offset less than a critical value of 17 MHz we find that the solitons are able to stay locked to each other with a stable delay between the two solitons whereas for offsets greater than this critical value the two solitons are not able to stay locked to each other. The inset shows the trajectory for a locked and unlocked pair of cavity solitons. The critical threshold of 17 MHz is set by the strength of the inter-cavity coupling and increases for stronger inter-cavity coupling.
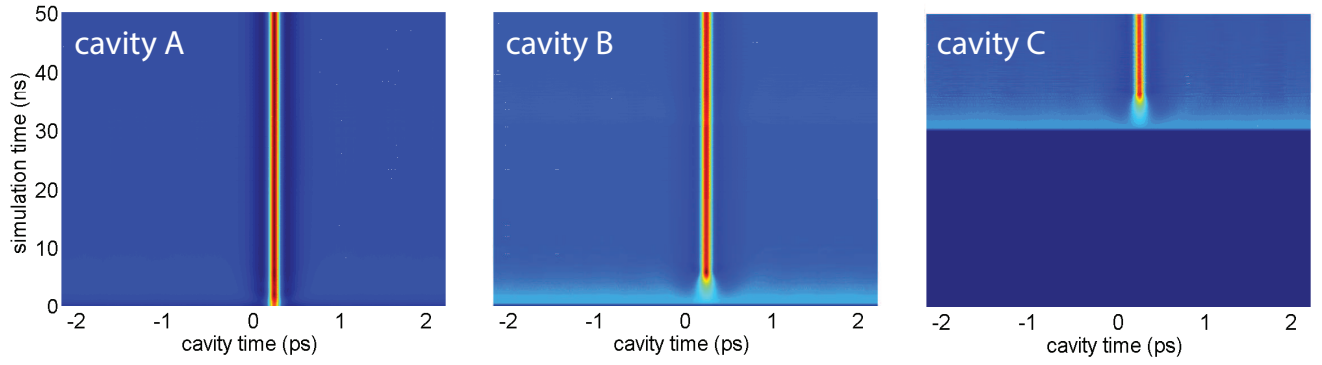
Figure 4.7: Synchronization of three cavity solitons. Each cavity is initialized by a brief chaotic stage before being tuned into the soliton regime at which point the previous cavity seeds the formation of a synchronized soliton in the new cavity.

4.6 Other coupling protocols

A wide range of interaction are available in the two-cavity system by bringing together cavites with non-trivial initial states. A simple example of this extension is shown in figure 4.6 where we show the interaction between a cavity-B that is allowed to freely evolve into a multi-soliton state and which is then brought into coupling with a cavity-A that has a single soliton state. The coupling is between the two cavities are turned on at 25 ns. Cavity-A is not noticeably affected but the soliton in cavity A has the effect of preferentially supporting the soliton with which it overlaps in time and suppressing the other thus bring cavity-B into a single soliton state that is synchronized with cavity-A. Figure 4.6 compares the spectral power and phase at initial coupling to the final spectral power and phase. It is possible to imagine such interactions forming the basis of various types of multi-bit computational gate with the pulse pattern in each cavity representing a bit pattern.

4.7 Synchronization of three or more frequency combs

The scability of the system and the large number of controllable degrees-of-freedom allows the exploration of an extensive breadth of coupling topologies and operational regimes. As a first step we extend the protocol to a three-cavity system and show that synchronized solitons can in principle be generated in an arbitrary number of neighbor-to-neighbor coupled cavities. Figure 4.7 shows the temporal evolution of a system with A-to-B-to-C coupling. Here we employ a 4 stage protocol where cavity B is first synchronized to cavity A as mentioned above and is allowed to stabilize. Then at the 30 ns mark the pump in cavity C is turned on in identical fashion to the initialization of cavity B, and likewise the synchronized soliton is generated as the cavity exits the chaotic stage.

4.8 Topological nonlinear optics and soliton dynamics

We believe that this system is an ideal platform for extending topological photonics into the nonlinear regime. Several demonstrations have shown the ability of topologically designed photonic systems to have protected paths and exhibit novel states of light in the linear regime. Adding nonlinearity may reveal new paths towards on-chip non-reciprocal propagation and schemes for switching and routing based on nonlinear mode conversion. In the soliton regime this system may be amenable to ideas from collision-based computation where the interactions between solitons with many degrees of freedom become the basic units of computation. Also, exploitation of the subcritical and "excitatbility" dynamics of cavity solitons in a network context could allows models of

neuro-networking previously unavailable. Experimental demonstration of the schemes proposed in this chapter could open up many areas of new research.

CHAPTER 5

ZENO-BASED ALL-OPTICAL CONTROL OF MICRORESONATOR DEVICES

In this chapter we investigate an approach for wavelength-selective control of a silicon micro-ring using the narrowband Raman induced optical loss in silicon. We demonstrate theoretically the system as a wavelength-selective reconfigurable all-optical add-drop filter (WS-ROADM) and perform experimental demonstrations that show strong single resonance control and wavelength-selective switching capability. We theoretically show that in certain schemes picojoule control pulses can selectively modulate and "erase" a single cavity resonance from full extinction to greater than 97% transmission while leaving adjacent resonances undisturbed. Full switching is achievable in less than 300 ps with only a few hundred femtojoule energy dissipation.

Integrated silicon photonics has for the last 20 years been the leading choice for chip-based, high-speed optical signal processing due to its compatibility with CMOS technology, transparency to standard telecommunications wavelengths and strong nonlinear optical coefficients[70]. Two of the key components to an chip-based optical network are low-loss all-optical switches and router [71]. Efficient all-optical switching in silicon has been demonstrated primarily in resonant devices using the Kerr nonlinearity or free-carrier refraction [72, 73, 22, 24]. However, these nonlinear refractive effects are broadband and simultaneously affect all resonances of a cavity [24]. While this is desirable in many applications, the full functionality of an all-optical router is realized only if separate channels can be modulated independently.

Active modulation of on-chip optical cavities is typically achieved via a refractive index shift through free-carrier effects or the Kerr-nonlinearity [24, 22].

However the broadband nature of such index-shifts alters all of the resonance wavelengths and does not permit control of individual frequency channels of the cavity. This limits its full functionality as a multi-channel router and limits access to other important cavity parameters such as cavity Q, linewidth and on-resonance transmission, which are important for both active operation and post-fabrication fine-tuning of the cavity properties [74].

5.1 The Zeno effect and classical analogues in optical cavities

In resonant structures it is possible to achieve all-optical switching by changing the coupling condition through optically induced loss. Increasing the loss of a critically coupled resonator will significantly increase transmission on-resonance, and this has been termed "Zeno" switching [20]. It is therefore possible to achieve wavelength-selective switching and routing using a narrowband absorption feature in a multi-port resonator.

Raman-induced loss in silicon is ideal for wavelength-selective all-optical switching. Inverse Raman scattering in silicon produces strong loss at the anti-Stokes wavelength [75] with a bandwidth much narrower than the free spectral range of a typical microring cavity but wider than the resonance linewidth. It is tunable simply by changing the control wavelength. This allows the Raman loss to modulate a single resonance while leaving adjacent resonances undisturbed. Loss-based switches have also been proposed using TPA in atomic vapor [20] or DFG in III-V materials [76] as the loss mechanisms and subsequently demonstrated.

We proposed that these previously unaccessible functionalities can be

achieved through all-optical control of a narrowband loss in the cavity at the signal wavelength by stimulating Raman loss through the inverse Raman scattering (IRS) process [77]. In silicon, IRS produces a 105-GHz-wide (1-nm) spectral loss at the anti-Stokes wavelength which is blue-detuned by 15.6 THz with respect to the control beam. For a typical micro-resonator, this stimulated Raman loss (SRL) is spectrally wider than the cavity linewidth but narrower than the free spectral range (FSR), allowing it to alter a single resonance and leaving the adjacent resonances undisturbed. This resonant interaction enhances the coupling of the signal into the cavity making it far more efficient than a direct absorption switch. Furthermore, the coupled signal light continues to circulate in the ring cavity and can be re-routed with an adjoining drop waveguide [78].

Precision control of optical loss in optical cavities has also attracted recent interest for fundamental studies of light-matter interactions as coherent perfect absorption and time-reversed lasing in a fabry-perot cavity [79]. Additionally, optical resonators provide an optical analog for the quantum Zeno and anti-Zeno effects wherein the transition between two photonic states can be inhibited or enhanced through decoherence (*i.e.* optical loss) of the second state [20, 80].

5.2   Theory: description and predictions

Consider a weak anti-Stokes signal (blue) and strong control (red) both resonant with the ring and coupled into their respective in-ports (Fig. 5.1). For both the control and signal to be simultaneously resonant, the ring's free spectral range (FSR) must be equal to an integer fraction of the Raman shift Ω_R. Transmission on resonance ($\phi(\lambda) = m2\pi$) can be solved from Eq.1.1 as a function of the
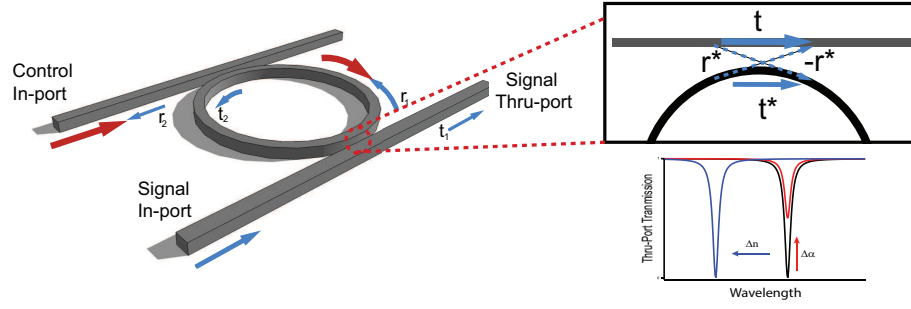
Figure 5.1: Add-drop filter with counter-propagating control (red) and anti-Stokes signal (blue). Transmission is observed as the signal through-port. The control in-port also serves as the signal drop-port.

waveguide coupling and the intrinsic resonator loss.

$$T_{\mathrm{N}}(\lambda_{\mathrm{res}}) = \left[\frac{t_1 - \alpha t_2}{1 - \alpha t_1 t_2} \right]^2, \tag{5.1}$$

where $\alpha = e^{-a(\lambda)L/2}$, L is the circumference of the ring, $a(\lambda)$ and $n(\lambda)$ are the loss coefficient and the refractive index, respectively.

In the absence of the control, the total loss is the intrinsic loss of the ring, $a(\lambda) = a_1$. Critical coupling is obtained for $\alpha = |t_1|/|t_2|$, when the round trip loss is matched by the ratio of the bus waveguide and drop waveguide coupling rates. The through-port transmission $T_{\mathrm{N}}(\lambda_{\mathrm{res}}) = 0$, and the drop-port transmission is unity. The through-port transmission spectrum of the add-drop filter with Q = 200,000 is plotted in Fig. 5.2(a). Since the linewidth is extremely narrow the resonances appear as single lines.

In the presence of the control, the ring becomes lossier due to Raman-induced loss $a_{\mathrm{R}}(\lambda)I_c$. The control also introduces a Kerr index shift and generates free carriers through TPA. The free-carriers lead to free-carrier absorption (FCA) and free-carrier refraction (FCR). However, all the deleterious effects can be significantly reduced by using a *p-i-n* diode to shorten the carrier lifetime, as we

will discuss later. The loss and refractive index have the following form, with the Raman loss being the dominant term:

$$a(\lambda) = a_{\mathrm{l}} + a_{\mathrm{fca}} + a_{\mathrm{R}}(\lambda)I_c,$$

$$n(\lambda) = n_0(\lambda) + n_{\mathrm{fcr}} + n_2 I_c. \tag{5.2}$$

As the Raman-induced loss increases (smaller α), the transmission increases from full extinction to the maximum value of t_1^2. For low intrinsic loss, t_1^2 is nearly unity and T_{N} is a sensitive function of I_c. Thus the transmission on resonance can be modulated for a critically coupled resonator between total extinction and full transmission (Fig. 5.3 inset), with no change to the transmission of the other resonances.

The magnitude of the induced Raman loss depends linearly on the intensity
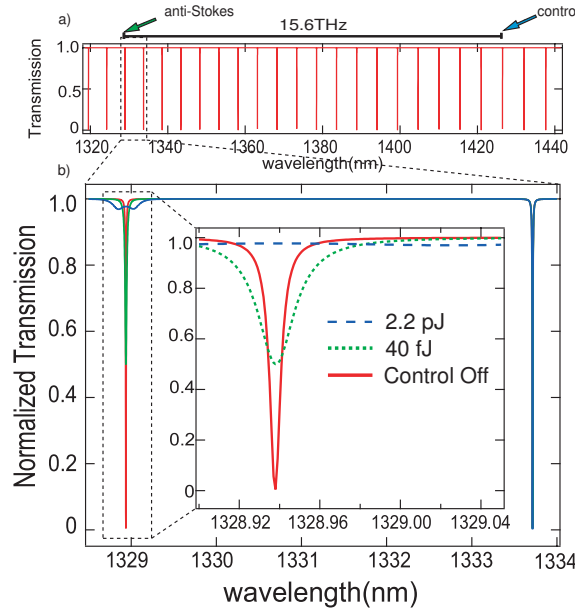
Figure 5.2: (a) Passive transmission spectrum of high-Q silicon add-drop filter. The control and anti-Stokes signal are tuned to resonances 15.6 THz apart. (b) Transmission at the anti-Stokes resonance for several control pulse energies. Adjacent resonances are undisturbed.

of the control field inside the ring, and the loss is blue-shifted from the control

by the Raman frequency Ω_R of the material with a bandwidth of Γ_R. For silicon the Raman frequency $\Omega_R = 15.6$ THz and bandwidth $\Gamma_R = 105$ GHz [75]. The strength of the Raman loss in silicon is found by normalizing the peak of the Raman gain at the Stokes wavelength to the experimentally obtained values for peak Raman gain $g_R = 76$ cm/GW for $\lambda_c = 1430$ nm [81]. The highest Raman gains were observed for shorter control wavelengths and control pulses longer than the Raman ring-down time of 10 ps [82]. Here we consider control pulses in the range of 200-300 ps at 1430 nm and the anti-Stokes signal near 1330 nm. Close to the anti-Stokes frequency $\omega_a = \omega_c + \Omega_R$, Raman loss in silicon is

$$a_R(\omega) = \frac{g_R \Gamma_R^2}{(\omega - \omega_a)^2 + \Gamma_R^2},\tag{5.3}$$

We assume a waveguide dimension of 250 nm X 450 nm and ring diameter of 32 μm ($L = 100\,\mu$m) which corresponds to a FSR equal to an integer fraction of the Raman shift so that the control and anti-Stokes wavelengths are simultaneously resonant. We assume linear loss of 1.74 dB/cm which corresponds to an intrinsic $Q = 400{,}000$. These values have been demonstrated with current fabrication techniques [83]. An output coupling of $t_2 = 0.9998$ is chosen, corresponding to $t_1 = 0.996$ resulting in $Q = 200{,}000$. This provides field enhancement to both the control and anti-Stokes beams in the ring by a nominal factor of F/π where $F = FSR(Q/\nu)$ is the finesse of the cavity. The free-carrier density can be calculated according to the rate equation, $\partial N_e/\partial t = \beta_{TPA} I_c^2/2\hbar\omega_0 - N_e/\tau_c$ [85] where $\beta_{TPA} = 0.5$ cm/GW. We assume a *p-i-n* diode swept free-carrier lifetime of $\tau_c = 12$ ps [84], in which case FCA becomes negligible compared to the Raman-induced loss. FCR is still sufficient to blue-shift the resonance by more than a linewidth, but this effect becomes comparable to the red-shift from the Kerr nonlinearity. For the control intensities under consideration, these two effects effectively can-
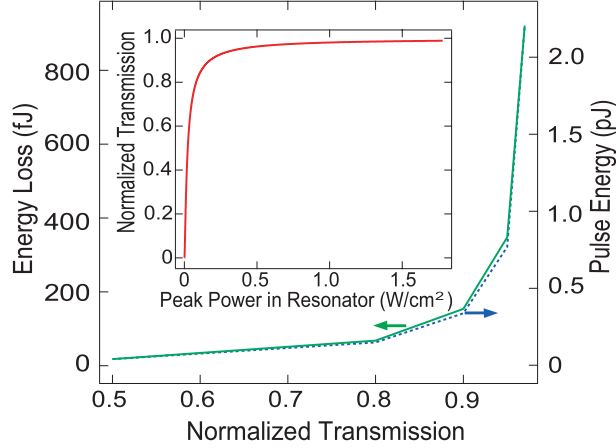
Figure 5.3: Control pulse energy and energy dissipation required to achieve certain transmission. (inset) Transmission as function of power inside cavity. Switching is most efficient for transmission values below 90%.

cel out.

The transmission at the anti-Stokes wavelength is plotted for 1427.7 nm control pulses at several energies (Fig. 5.2b). On-resonance transmission of 50% (90%) is achievable with control pulse of 40 fJ (340 fJ)/bit with energy dissipation of 18 fJ (154 fJ)/bit. Transmission of >97% (<.1 dB loss) is achievable with control pulses of 2.2 pJ/bit and energy dissipation of 921 fJ/bit (Fig.5.3). These values are comparable with carrier and Kerr-based switches in silicon microrings [22, 72]. It is noteworthy that the narrowband Raman response leaves adjacent resonances essentially undisturbed, which opens up the possibility of independent routing or modulation of multiple signals on a single resonator.

Switching is most efficient for transmission below 90% but rolls off for higher transmission (Fig.5.3). The roll-off value increases for lower intrinsic loss, thus higher-Q resonators yield better switching performance. At higher control energies, cavity enhancement decreases due to FCA and TPA. The enhancement F/π has a nominal value of 250 but decreases with increasing control pulse energy and is 4 times lower for the 2.2 pJ pulse than for the 40 fJ pulse. Thus, operating
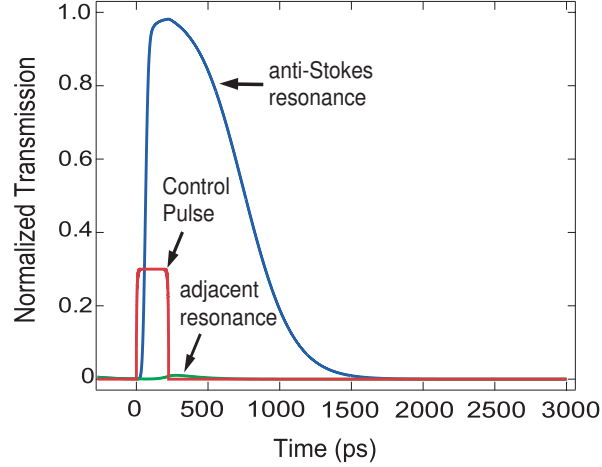
Figure 5.4: Response of anti-Stokes signal at through-port to 2.2 pJ, 300 ps control pulse. 97% transmission is achieved with adjacent resonance essentially undisturbed.

below 90% transmission will significantly reduce power consumption.

Time-domain switching dynamics confirm the independent switching of a single resonance at GHz rates (Fig.5.4). A 2.2-pJ control pulse achieves maximum transmission of 97%, matching the results of the frequency-domain analysis (Fig.5.4). The adjacent resonance sees an 1% increase in transmission due to broadband FCA. The switch-on time, defined as the time required for the signal to be fully switched from the drop-port to the through-port, is less than 300 ps, and the total response time for a full switching cycle is roughly 1.5 ns. This corresponds to data rates of >500 MHz on a single channel with rates of >1 GHz possible at lower switching contrasts.

A SRL-based add-drop filter would enable the device envisioned in figure 5.5, a wavelength-selective reconfigurable all-optical add-drop multiplexer (WS-ROADM). Such device in a compact and chip-based platform would be a significant technological advanced for datacom application, especially in wide area and metro area networks that require a large degree of reconfigurability to be able to respond to change bandwidth demand and unpredictable traffic
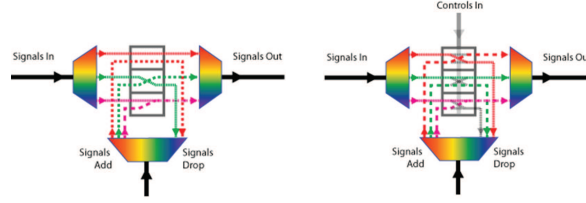
Figure 5.5: Non-reconfigurable vs. reconfigurable add-drop filter. (left) The data paths of the non-reconfigurable devices are preset whereas (right) the data paths of the reconfigurable device can be controlled in real-time allowing dynamis allocation of bandwidth resources.

spikes.

5.3 Experiment: Zeno switching using inverse Raman scattering in silicon micro-rings

In this section we describe the experimental demonstration of the wavelength-selective control of single resonances described in the previous section in a singly-coupled micro-rings resonator in the over-coupled regime. A strongly over-coupled resonance is brought into critical coupling with continuous tuning of the on-resonance transmission by 9 dB (87%) and reduction of the intrinsic Q factor by more than a factor of five (from 82,130 to 15,812) via the Raman loss induced by 13 pJ, 200 ps control pulses. This is achieved without shifting the resonance wavelength and with minimal disturbance to adjacent resonances. Adjacent signal resonances are controlled with similar efficiencies by tuning the control pulse to the adjacent control resonance. Lastly, we show that the resonance can be tuned from the over-coupled regime through the critical coupling state and into the under-coupling regime.
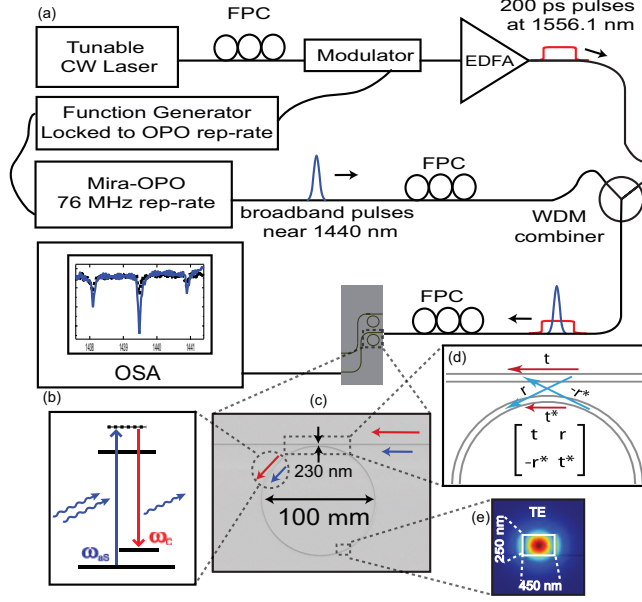
Figure 5.6: (a) Schematic for all-optical control of a single resonance. 200 ps control pulses at 1556.1 nm are generated at the rep-rate of the optical parametric amplifier (OPO) which generates the broadband signal pulses near 1440 nm. The low power signal pulse does not cause nonlinear effects. The two pulses are combined and synchronized in time and injected into the silicon waveguide using a free-space objective. The through-port transmission is coupled out using a lens-tipped fiber and characterized by an optical spectrum analyzer with resolution of 0.01 nm. (b) Energy level diagram of IRS, (c) SEM image of ring-resonator, (d) Model of the coupling region using the scattering matrix formalism (e) simulation of TE mode cross-section.

A ring resonator coupled to a single bus waveguide [Fig. 5.6(c)] has coupling region modeled by a coupling matrix given in Fig. 5.6(d), with field coupling-rate of $r = i\sqrt{1 - t^2}$ and a field transmittance t, which is close to unity for a weakly coupled cavity. The on-resonance transmission at the through-port is given by,

$$T_{\mathrm{N}}(\lambda_{\mathrm{res}}) = \left[\frac{t - \alpha}{1 - \alpha t}\right]^2, \tag{5.4}$$

71

where $\alpha(\lambda) = e^{-a_i(\lambda)L/2}$ is the round-trip field transmission of a ring cavity of circumference L, and $a_i(\lambda)$ is the intrinsic loss coefficient [77, 86]. The related Q factors provide an equivalent analysis of the system where $Q_{i,l} = \lambda/(a_{i,l}(\lambda) \cdot FSR \cdot R_{ring})$, FSR is the free-spectral-range and R_{ring} is the ring radius. We define the loaded loss coefficient $a_l(\lambda) = a_i(\lambda) - 2 \cdot ln(t)/L$, where the out-coupling is included as a loss process in the cavity. The on-resonance transmission in terms of the Q factors is $T_N(\lambda_{res}) = (1 - 2Q_l/Q_i)^2$. However, the $a(\lambda)$-t picture is the more natural basis with which to analyze the performance of the system since $a(\lambda)$ and t correspond directly to the controllable parameters of intra-cavity loss and coupling gap, respectively.

Figure 5.7 (inset) plots Eq. (1.2) as a function of α for $t = 0.93$ and shows that the transmission is most sensitive for values of α in the over-coupled regime, where the round-trip intra-cavity loss is less than the waveguide-cavity coupling-rate (i.e. $\alpha(\lambda) < |t|$). Without the control beam, only the linear loss contributes to the loss coefficient (i.e. $a(\lambda) = a_L$). The control beam stimulates Raman loss $a_R(\lambda, I)$ and generates several undesirable broadband nonlinear effects. Degenerate two-photon absorption (D-TPA) of the control grows quadratically with control power and generates free-carriers which causes free-carrier absorption (FCA). Non-degenerate TPA from control plus anti-Stokes photons adds to broadband loss of the signal, which grows linearly with control power. These two losses are represented as a lumped broadband loss $a_{NL}(I, I^2)$ such that $a(\lambda, I) = a_L + a_R(\lambda, I) + a_{NL}(I, I^2)$, where $I = \mathcal{F}_{eff} \cdot E_c/(\pi \cdot \tau_c \cdot A_{eff})$ is the intra-cavity intensity, $\mathcal{F}_{eff}$ is the effective finesse at the control wavelength, E_c is the control pulse energy, τ_c is the control pulse width and A_{eff} is the effective mode area of the waveguide. D-TPA of the signal is negligible due to the low signal powers in use. The broadband nonlinear losses and the associated refractive effects
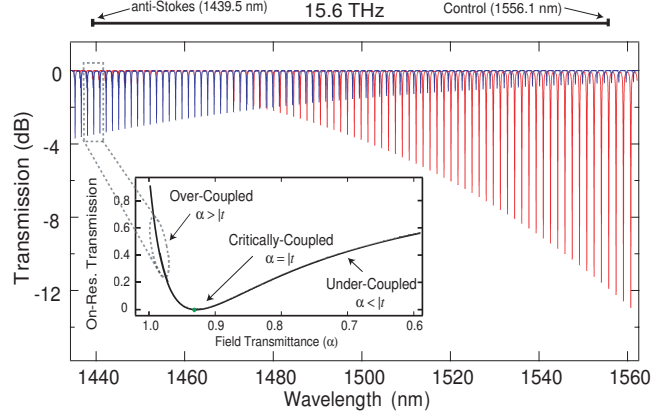
Figure 5.7: Theoretical transmission of the TE (red) and TM (blue) modes across the relevant spectral range. Control (TE at 1556.1 nm) is near critical-coupling, anti-Stokes signal (TM at 1439.5 nm) is in strongly over-coupled. The two are separated by exactly Ω_R of silicon and are both resonant with the cavity. (Inset) Through-port transmission for a cavity as a function of the intra-cavity field transmission.

become a limiting process on the overall control efficiency and wavelength selectivity.

Inverse Raman scattering is a stimulated stokes scattering process wherein an anti-Stokes photon is scattered into a pump photon and the energy difference is deposited as an optical phonon in the material. Previously measured IRS in silicon nanowaveguides is consistent with the known Raman gain coefficient of $g_R = 7$ cm/GW at the control wavelength 1550 nm [?]. The SRL near the anti-Stokes frequency ω_a is given by,

$$a_R(\omega, I) = \frac{g_R \Gamma_R^2}{(\omega - \omega_a)^2 + \Gamma_R^2} I, \tag{5.5}$$

where $\Gamma_R = 105$ GHz is the Raman loss linewidth for silicon. The FSR is chosen to be an integer fraction of $\Omega_R=15.6$ THz such that the transverse electric (TE) control beam at 1556.1 nm and the transverse magnetic (TM) anti-Stokes signal beam at 1439.5 nm are simultaneously resonant with the ring. Figure 5.7 shows

the theoretical transmission spectra of the TE (red) and TM (blue) modes and the spectral placement of the control and signal.

Simulations reveal that the cross-sectional dimensions of TE mode at 1439 nm is 15% shorter and 20% narrower than that of the TE mode at 1556 nm. This mode size difference leads to a significant difference in coupling rates for the control and signal. Using the more delocalized TM mode for the shorter anti-Stokes wavelength alleviates this difference for the disparate wavelengths. The Raman interaction in silicon is also stronger for orthogonally polarized control and signal beams. For waveguides fabricated on a wafer grown in the [001] direction and traveling in the [110] direction, the Raman interaction for TE-TM or TM-TE control-signal combination is enhanced by a factor of 3 over the TE-TE combination. In a circular ring cavity the control and signal fields sample all 2π of lattice directions which reduces the enhancement to a factor of 1.5 for the TE-TM combination over the TE-TE combination [87, 82]. This suggests that the Raman interaction can be increased by using racetrack cavities that extend the portions of waveguide which prefer the TE-TM combination.

The ring-resonators are fabricated on a 250-nm SOI wafer with 3 μm of buried oxide using standard CMOS fabrication processes. The rings have a radius of 50 μm, and are coupled to a straight waveguide separated by a gap of 230 nm. All waveguides have cross-section of 450-nm wide by 250-nm tall and have an effective mode area A_{eff} = 0.25 μm^2. The anti-Stokes wavelength the field coupling rate is estimated to be r = 0.55 (t = 0.83) with an intrinsic loss of a_L = 10.77 dB/cm, which results in cavity resonances with an intrinsic Q_i = 82,130 but a loaded Q_l = 12,613. The large linear loss is due to the delocalized nature of the TM polarized mode and the large field coupling rate achieves initial over-coupling for the signal resonance. The control pulses are 200 ps which is close
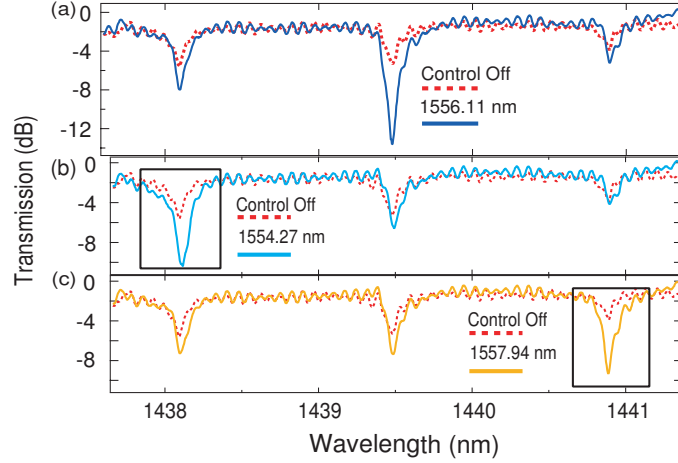
Figure 5.8: Through-port spectra of three resonances near the anti-Stokes wavelength (TM) as the control pulse (TE) is tuned to the corresponding control resonances. The control pulses have an energy of 13 pJ. (a) Control: 1556.1 nm, anti-Stokes: 1439.54 nm; (b) Control: 1554.27 nm, anti-Stokes: 1437.97 nm; (c) Control: 1557.94 nm, anti-Stokes: 1441.11 nm

to the lifetime of the cavity. This reduces the effective finesse ($\mathcal{F}_{eff}$) from the steady-state value of 63 to 36. The optical transmission of the cavity was characterized using a low-power broadband pulse near the anti-Stokes wavelength (Fig. 5.6).

Figure 5.8 shows the narrowband SRL acting on single resonances. The affected resonance is exactly 15.6 THz blue-shifted from the control wavelength. The adjacent signal resonances can likewise be controlled by tuning the control wavelength to an adjacent control resonance such that the anti-Stokes loss shifts to the corresponding signal resonance [Figs. 5.8(b) and 5.8(c)]. This indicates that Raman loss is the dominant process affecting the resonances. The non-anti-Stokes resonances are not affected by the Raman loss, however the broadband TPA and FCA loss does result in modulation of their transmission by 1-2 dB for a 13-pJ control pulse. The contribution of the nonlinear losses to the system is further discussed in Fig. 5.10. A micro-resonator with flat dispersion can have
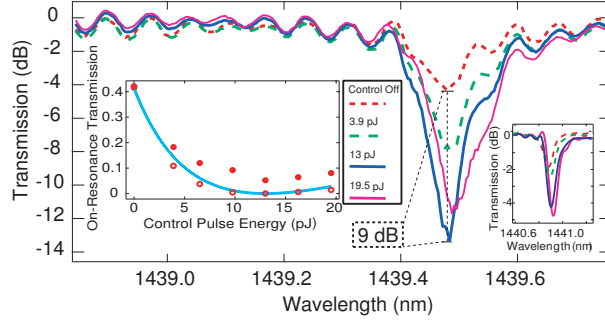
Figure 5.9: Transmission of the anti-Stokes signal resonance (1439.5 nm, TM) with increasing control pulse energy (1556.1 nm, TE). (left inset) Comparison of the on-resonance transmission (solid dots) with Eq. (1.2) (blue line) and with a full-spectrum coupled-mode model (circles). (right inset) Response of adjacent resonance to increasing control pulse energy.

100's of doubly resonant pairs [39].

From Fig. 5.8 alone it is not conclusive whether the modulation is due to loss-induced resonant coupling, as we claim, or to SRL of the signal in the straight waveguide. Figure 5.9 shows the power dependance of the central resonance. The on-resonance transmission drops sharply from -4.3 dB to -13.3 dB (blue) for 13-pJ control pulse, equal to 4.7% transmission and >87% switching contrast. For control pulses greater than 13 pJ, the anti-Stokes transmission increases (purple, 19.5 pJ control pulse) indicating that the modulation cannot be due to direct absorption of the signal. Rather, the increase in transmission is consistent with a resonant cavity as described by Eq. (1.2) (Fig.5.9 left inset). This is further confirmed by the continued decrease in transmission of the adjacent resonance (Fig. 5.9 right inset) and by the broadened linewidths of both resonances. Both observations indicate that the spectra for 19.5 pJ control pulse corresponds to greater loss, and hence greater power, inside the cavity. The signal loss due to SRL in the straight waveguide is less than 0.1 dB. An off-resonant measurement of the Raman absorption at the anti-Stokes frequency in the straight waveguide

reveals 0.25 dB of loss for a 20-pJ control pulse, but the loss is much less for resonant control and signal since the signal experiences Raman absorption for only 5% of the entire length of the straight waveguide.

Additionally, the linewidth, and therefore the Q, can be continuously tuned with increasing control energy. Figure 5.10 shows the single resonance intra-cavity loss and Q extracted from the resonance linewidth and extinction [88]. The initial Q_l is 6.5 times smaller than the initial Q_i of the cavity, but should be exactly 2 for a critically-coupled cavity. This ratio drops to 2.3 for a 13-pJ control pulse, indicating that the cavity is tuned close to critical coupling. For a 19.5 pJ control pulse, the Q_i decreases by a factor of 5.19, from 82,130 to 15,1812. Correspondingly, the intra-cavity loss increases by 45.2 dB/cm. Comparing the intra-cavity loss of the anti-Stokes resonance (Fig. 5.10, blue circle) with that of an adjacent resonance (green diamond) indicates that TPA and FCA contributes 16% (7.24 dB/cm) of the total loss of the anti-Stokes cavity, the other 84% (38.0 dB/cm) is due to Raman loss. TPA and FCA makes an appreciable contribution at high control powers due to its quadratic growth with control intensity. The sub-linear increase of the intra-cavity loss with the control pulse energy is consistent with broadband TPA and FCA reducing the Q factors for the control wavelength. The nonlinear losses measured from the adjacent resonance corresponds to a 45% decrease in both Q_l and $\mathcal{F}_{eff}$ at the control wavelength, in agreement with theoretical predictions (Fig. 5.10).

In the current scheme the passive signal transmission can be increased to greater than -0.2 dB (95%) by using a more over-coupled cavity. Routing applications require a drop waveguide to couple out the signal from the cavity where it would be advantageous to use an initially critically-coupled cavity and use the loss to push the cavity into under-coupled regime as described in [77]. The
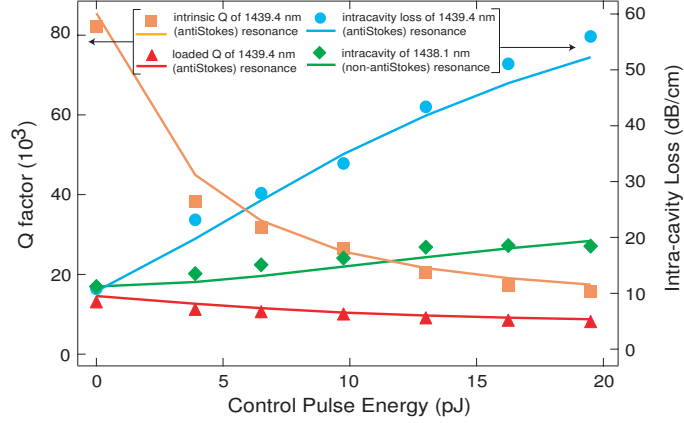
Figure 5.10: Experimentally extracted values of the cavity loaded Q_l and intrinsic Q_i factors for the anti-Stokes resonance and intra-cavity loss for the anti-Stokes resonance and an adjacent resonance. A control pulse of 13 pJ corresponds to the condition closest to critical-coupling. Comparison of the intra-cavity loss of the two resonances reveals the contribution of TPA and FCA to loss in the system.

under-coupled regime allows complete isolation of the bus and drop waveguide in the on-state, which is not possible for the over-coupled cavity. For high-Q cavities (Q_l > 200,000), signal routing can be achieved with <0.1 signal loss (>97% transmission) for picojoule control energies. Selective routing of single channels dramatically increases the degrees-of-freedom and data density of the system. Networks of such devices with multiplicative degrees-of-freedom can easily be envisioned [89].

It was recently noted that a resonant beam coupled into a critically-coupled cavity is equivalent to a single channel time-reversed laser at threshold [79]. In a time-reversed laser optical gain is replaced with optical loss, coherent light is coupled into the cavity, and the equivalent threshold is reached when the net intra-cavity loss equals the coupling-in rate of the resonant light. Here we use SRL to match the intra-cavity loss to the coupling-in rate such that the conditions for time-reversed lasing are satisfied and resonant light is fully absorbed

within the cavity. We reach a lowest transmission of 4.7%, which is comparable to the lowest transmission obtained at the time-reversed lasing threshold in [79]. Both systems exhibit the counterintuitive behavior that increasing the loss beyond the "threshold" actually decreases the net absorption, an observation consistent with the resonant nature of the cavity. Thus, the current system is a demonstration of the time-reversed process of stimulated Raman lasing in silicon micro-rings [70].

The dynamics shown here are also the optical analogue of Zeno effects observed in decoherence-driven atomic ensembles and quantum two-level systems where the natural evolution of the system is strongly perturbed by frequent measurement or decoherence on the upper state [80, 91]. This relation has been well established and is a current topic investigation by several groups [20, 76, 90]. In atomic systems [80, 91] measurement-induced decoherence enhances (anti-Zeno) the transition between two states for infrequent measurement and inhibits (Zeno) the transition for more frequent measurement. Here, the mode of the bus waveguide and the resonant mode of the cavity at the anti-Stokes wavelength represent the two photonic states, and the stimulated Raman absorption of anti-Stokes photons constitutes the measurements of the "upper" cavity state by coupling it to the phonon bath of the waveguide. The strength of the induced decoherence is directly (inversely) proportional to the frequency of (delay between) the loss events. For control pulses below 13 pJ, the cavity experiences anti-Zeno enhancement of the photonic transition but for higher control energies the cavity experiences Zeno inhibition of the transition. The current scheme provides a robust and sensitive platform for exploring the effects of loss on the thermodynamics of classical and quantum photonic states.

Stimulated Raman loss in silicon allows the manipulation of single cavity
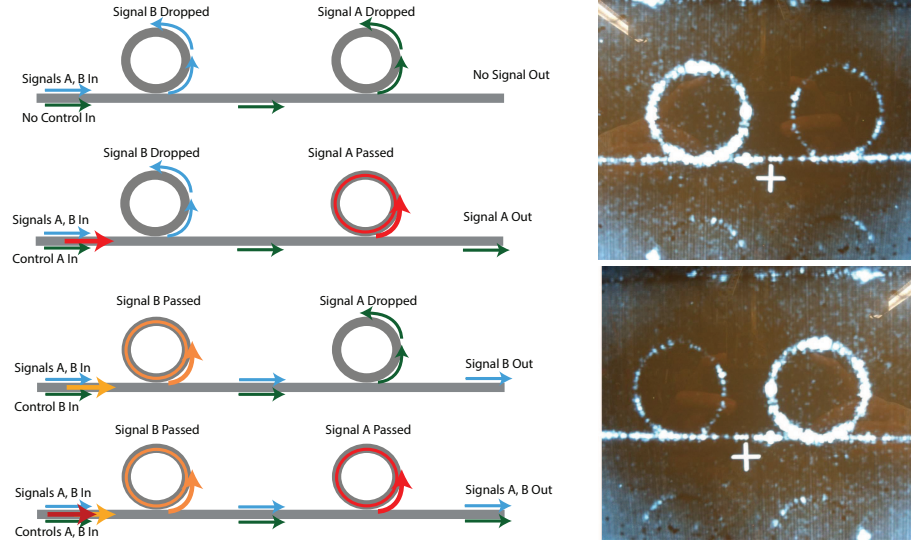
Figure 5.11: Two ring devices where ring resonances are offset slightly to clarify the individual cavity responses. The left diagram shows the four output states of the two-ring, two-signal system. The right micrographs show the two rings excited by a resonant pump field.

resonances in silicon micro-resonators. This system enables on-chip optical micro-cavities to achieve their full potential as multi-channel all-optical routers on a monolithic, CMOS compatible platform. This dramatically increases the degrees-of-freedom for design of both hardware and software for on-chip optical processing. Finally, it also demonstrates the universality of the effects of decoherence on resonant systems and their usefulness in controlling the system's dynamics.

5.4 Cascaded Raman-Zeno switching in multi-rings systems

In this section we extend the single SRL to a multi-ring system and demonstrate selective control of individual resonances of two silicon micro-ring resonators
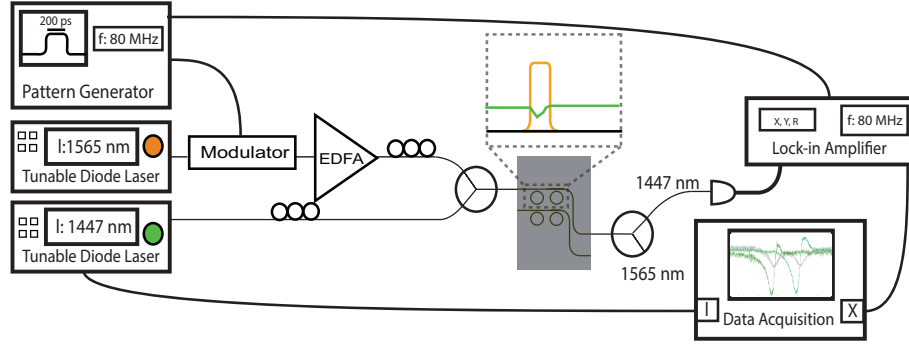
Figure 5.12:   Experimental setup of cascaded Raman-Zeno switching. Control pulse generate by electro-optic modulation of a CW 1550 nm laser and amplified by EDFA. Control pulse combined with CW signal at the anti-Stokes wavelength and injected into cavity. Signal is lock-in detected at the modulation frequency of the control pulse

in a cascaded configuration on the same chip, showing the potential of this platform to enable a new class of switching fabrics where the number of unique output states scales exponentially with the number of signals as $(N + 1)^s$, where N is the number of resonators and S is the number of signals. This scaling law far exceeds the data density of refractive index based switches for which the number of unique output states scale as $(N + 1)$.

The double ring system consists of two silicon micro-ring resonators coupled to a common bus waveguide without drop waveguides (Fig.5.11). The drop waveguide is excluded to simplify the coupling conditions of the disparate control and signal wavelengths. This simplified system does not allow add-drop functionalities but is sufficient for modulation and switching of individual resonances. The ring circumferences are slightly offset such that the ring resonances are spectrally distinguishable but the free spectral ranges are such that the control and signal wavelengths are simultaneously resonant.

Control pulses near 1565 nm are co-propagated with a CW signal at the anti-Stokes wavelength near 1447 nm (Fig. 5.12). The control pulses are 200-ps long

and generated from a CW diode laser modulated by an electro-optic modulator at a repetition rate of 5 GHz and then amplified by an EDFA. The probe signal is detected using a lock-in amplifier locked to the control pulse repetition rate.

The lock-in signal measures the amplitude of the modulation the signal experiences due to the control pulses mediated through the micro-ring. When the control is tuned 1565 nm, it is resonant with the left ring and Raman loss is induced only in the left ring at the anti-Stokes wavelength of 1447.2 nm. Likewise, when the control is tuned to 1565.3 nm Raman loss is induced only in the right ring at the anti-Stokes wavelength of 1447.4 nm. Figure5.13(a) shows the modulation response of the two cavity system when the control wavelength is resonant with the left ring (dark green) and the right ring (light green). The optical isolation of the two cavities is evident from the fact that no crosstalk is observed in either modulation response.

The Raman loss has been induced at 1447.2 nm, to overlap with the central resonance at 1447.2 nm. This has the effect of increasing the modulation depth of the central resonances by 35% compared to the two adjacent resonances. Although modulation due to two-photon absorption and induced free-carrier effects is present, the anti-Stokes resonance experiences stronger modulation due to the addition of the stimulated Raman loss, whereas the two adjacent resonances do not (Fig.5.13(a)). Figure 5.13(b) zooms in on the central resonance and compares its modulation strength due to free-carrier effects alone (red) and due to the addition of the Raman loss (green). When the control wavelength is tuned to that adjacent control resonances such that the Raman loss shifts to the adjacent signal resonances (Fig.5.13(c)). This confirms that the additional modulation is indeed due to stimulated Raman loss.

This proof-of-concept demonstration can be extended to show that a net-
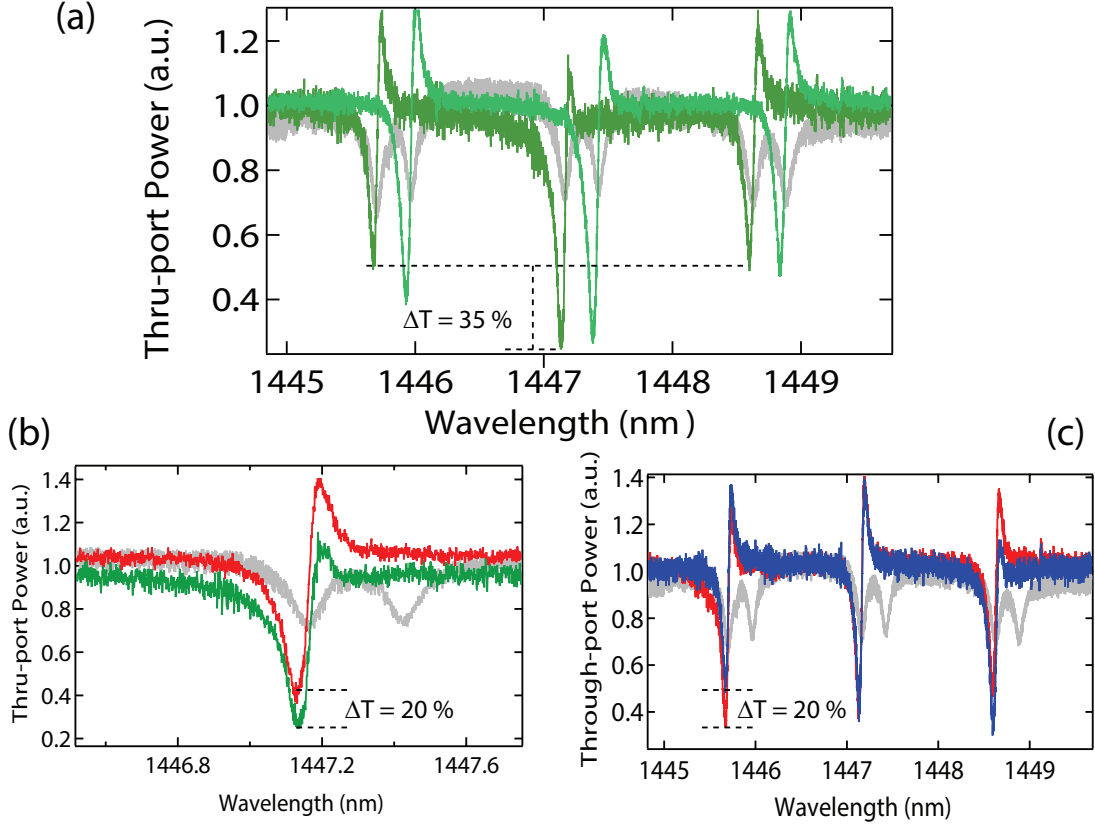
Figure 5.13: Response of cavity at anti-Stokes signal. (a)Dark(light) green traces show lock-in response of the two cavity system when the pump is resonant with the left(right) cavity. The clear spectral separation of the resonance response show good optical isolation of the two cavities. The Raman loss is active at the center resonance of each cavity which experiences a 35% transmission contrast compared to the two adjacent resonance which experience modulation due to free-carrier effects. (b)Red traces shows the response of the central resonance when it only experiences free carrier effects while the green shows response when Raman loss is active. (c) Red(blue) trace shows response of the three resonances when the Raman loss is active on the left(right) resonance

work of add-drop filters with control of individual resonances allows each ring to have as many degrees of freedom as it has number of operable resonances. For example, for two rings with two signals, the Raman switch has 9 distinct output states compared to 3 for a broadband nonlinear-index-based
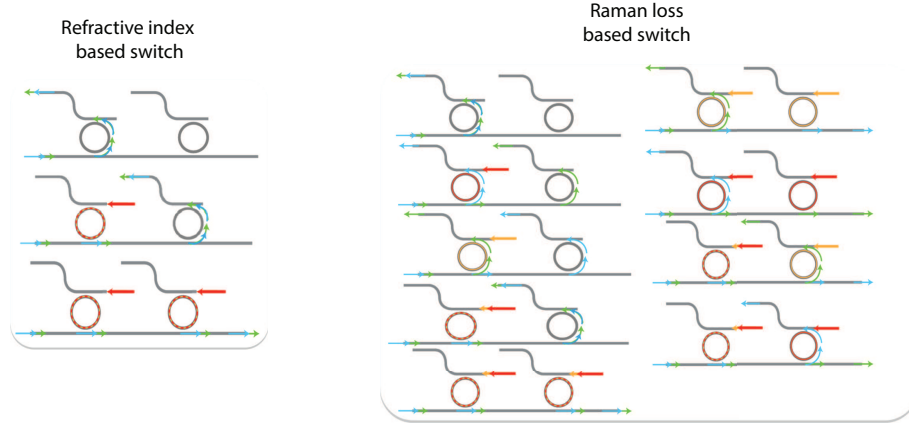
Figure 5.14: Comparison of unique output states for a two-ring (N=2), two-signal (s=2) system based on (left) broadband refractive index effect and (right) narrowband loss effect. The former scales as (N+1) while the latter scales at $(N+1)^s$

switch (Fig.5.14). This advantage increases exponentially for increasing number of resonators.

CHAPTER 6

ZENO EFFECT USING TWO-PHOTON ABSORPTION IN ORGANIC POLYMERS

In this chapter we turn to a second approach for resonant loss switching based on the two-photon absorption process in organic dye molecules engineered to have large nonlinear susceptibilities. These molecules are embedded into a transparent polymer such as PMMA and deposited directly onto an unclad or thinly-clad micro-ring resonator. Figure 6.1 shows in the top inset panels the unclad micro-ring resonator with a sample of the nonlinear dye-embedded polymer (green strip) along with its chemical structure. The top right panel shows the final device where the green strip covers the row on rings on the silicon chip.

6.1   High optical nonlinearities in π-conjugated carbon chains

The dye used in these experiments is call 7C-tricyanofurane (7C-TCF) indicating that it is formed by 7 carbon pi-conjugated chain terminated tricyanofurane groups. The long chain which is host to several delocalized electrons in a quantum well-like structure gives rise to the strong nonlinear susceptibility of the molecule. The in-solution TPA absorption coefficient has a peak of 22 cm/GW at 1550 nm and is largely maintained once embedded in the polymer (Fig.6.1). However, the linear loss of the polymer was measured to be 6 dB/cm. The linear index of the polymer is 1.69 which required the use of high index material like silicon to ensure guiding of the optical mode. A material such as silicon nitride would have been preferred on the grounds that it has lower Kerr non-
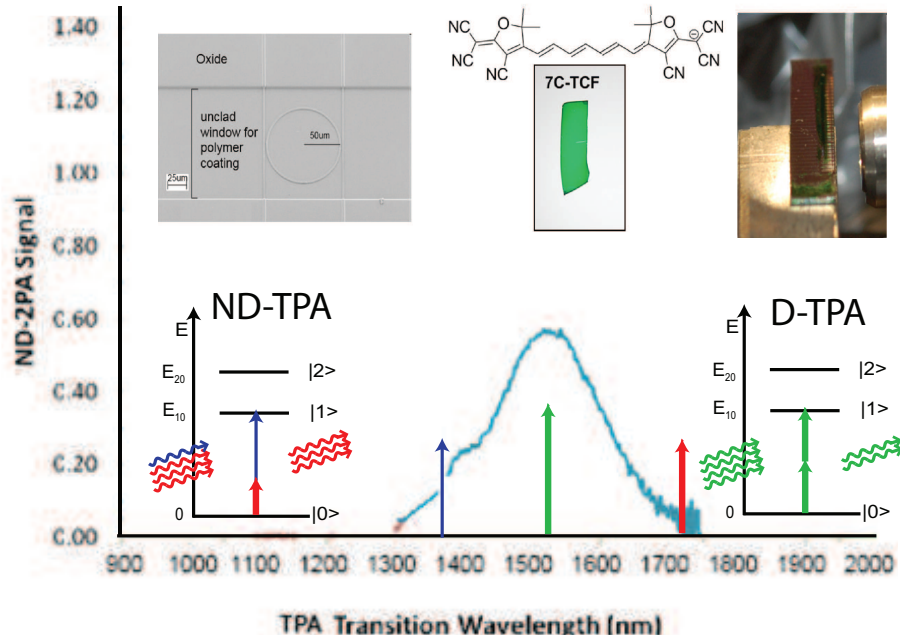
Figure 6.1: (main plot) Two-photon absorption spectrum of the 7C-TCF molecular system. Red and blue (green) arrows indicate wavelength for a non-degenerate (degenerate) switching scheme shown to the left (right) of the main spectrum. (top left) Micrograph of the unclad micro-ring. (top center) Molecular structure of the 7C-TCF molecule and a polymer embedded with 7C-TCF. (top right)Picture of polymer coated chip on the testing platform.

linearity than silicon and intrinsic two-photon absorption and no free-carrier generation, however the linear index of silicon nitride was too low to guide the optical mode when clad with the nonlinear polymer.

The two-photon absorption (TPA) process is diagrammed in degenerate (D-TPA) and nondegenrate (ND-TPA) schemes in the lower right and left insets, respectively. The degenerate case corresponds to excitation at the peak of the TPA spectra with a single high peak-power pulse (green arrow). The strong TPA response will effective make the cavity highly lossy to the pulse thus rejecting most the pulse from the cavity. This scheme can be considered a form of intensity switching where low peak power signals are extracted while high
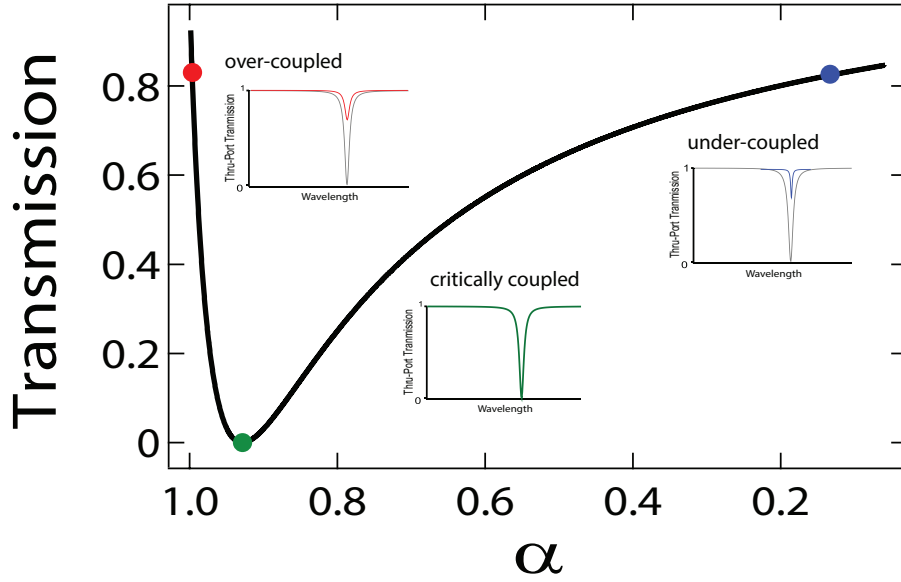
Figure 6.2: Diagram of the different coupling regimes. When loss is less(greater) than the coupling rate the system is over(under)-coupled indicated by the red(blue) dot. When the loss and coupling rates are exactly equal the system is critically coupled (green dot)

peak power signals are passed. The nondegenerate allows the definition of control (red arrow) and signal (blue arrow) fields where the nonlinear response only occurs when both control and signal fields are present. This allows the presence of the control field to switch the response of the micro-ring to the signal field. The ND-TPA scheme is operationally equivalent to the SRL scheme since they both have spectral different control and signal fields.

6.2 Degenerate characterization of organo-silicon hyrbid micro-resonator

In the current device it was prohibitively difficult to perform the nondegenerate scheme due to the different coupling rates between two fields that are separated by more than 300 nm. The differing coupling rates between disparate wavelengths is due to the differing sized waveguide optical modes, the volume of which scales as λ^2. If the cavity is optimized to critically couple the signal the control with be strongly over-coupled, if the control is critically coupled the signal will be under-coupled.

Figure 6.2 shows the position along the on-resonance transmission curve corresponding to various types of coupling and the insets show the qualitative feature of a resonance in each particular coupling regime. Both under-coupling and over-coupling of the signal has the effect of setting the initial state of the cavity at a high transmission state and either reduces the amount of control light that can be coupled into the cavity or reduces the range over which transmission can be tuned.

The system was characterized using the degenerate scheme described in figure 6.3. A tunable CW laser operating at 1550 nm is used as the degenerate signal. To test the nonlinear response of the organic-silicon device we send the signal light into the chip first in a low peak power (LP) state and then in a high peak power (HP) state. The low-peak power state is simply a CW field of 10 mW average power while the high-peak power state is a 200 ps pulse with a peak power of 600 mW at 80 MHz repitition rate, which correspond to an average power also of 10 mW given a duty cycle enhancement of 60. The pulses are carved by a high-speed function generator and an electro-optic modulator. The
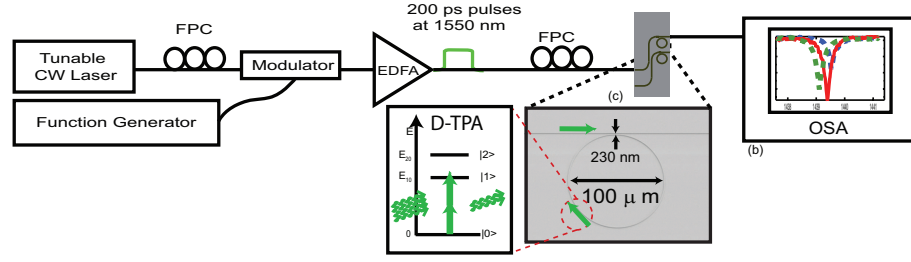
Figure 6.3: Experimental setup of the degenerate switching scheme in the organic-silicon hybrid devices. High power pulses of 200 ps and 600 mW peak power are generated by electro-optic modulation of a CW laser and amplified in an EDFA and used to excite the nonlinear response of the polymer-cavity system. Low power scan of the linear cavity resonance achieve through a non-pulsed CW field at 10 mW power.

signal field is sent into an EDFA and amplified to 10 mW average power and coupled into the chip waveguide using a low-NA objective lens. The device is characterized by scanning the wavelength of the laser across a resonance of the micro-ring at the two difference peak powers and compare the responses.

6.3   Evidence of nonlinear decoupling

Evidence of nonlinearity induced decoupling is shown in figure 6.4. The three resonance traces indicate separate scans of the resonances at the indicated peak powers and labeled (1), (2), and (3). From the linewidth of trace (2) we can deduce the intrinsic linear loss $a = 0.58 cm^{-1}$ which is equivalent to 2.5 dB/cm and coupling rate $t = 0.9927$ assuming the resonance is close to critical coupling. This corresponds to a loaded $Q = 19340$. Traces (1) and (2) show the HP and LP responses, respectively and the noticeable on-resonance transmission difference of 7.26 dB indicates the effect of the nonlinear decoupling.
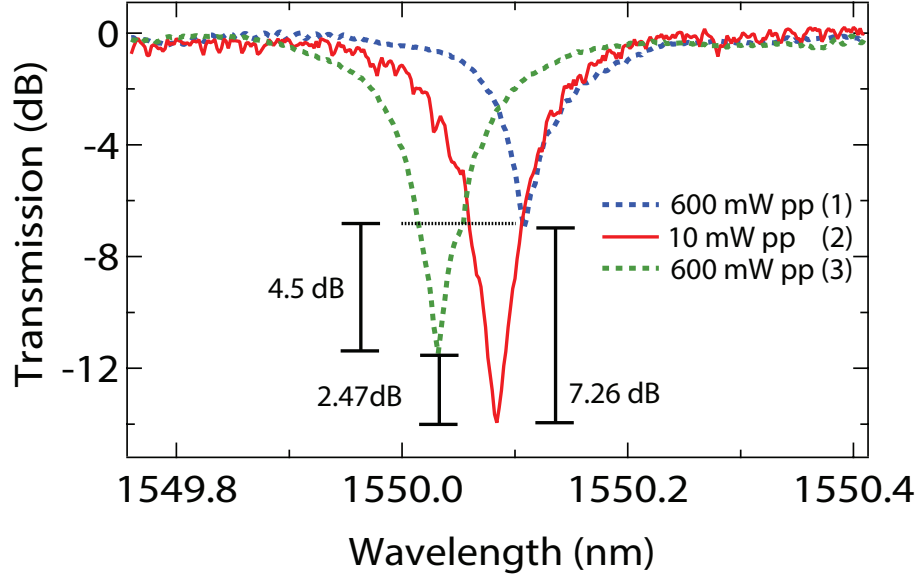
Figure 6.4: Comparison of low power (solid red) and high power (dotted blue and green) resonance scans shows total decoupling of 7.26 dB due to nonlinear polymer. Green trace indicates photobleached high powered response which shows decoupling due to silicon nonlinearities alone. The three scans were taken in the order shown in the figure legend.

However, this decoupling is necessarily the result of every possible nonlinear interaction occuring in the cavity, including the SPM, TPA and FCA of the silicon material itself. This contribution from the silicon would normally have been impossible to resolve experimental since the intra-cavity optical mode is result of the combination of the silicon waveguide and the polymer cladding. However, the organic polymer exhibits photobleaching of the nonlinear response such that after a few scans the organic polymer is not longer photoactive. This phenomenon allows us to measure the nonlinear response of the silicon material alone in trace (3). Comparison of trace (3) with (1) and (2) indicates that 2.47 dB of the decoupling can be attributed to the silicon waveguide while 4.5 dB of the decoupling can be attributed to the nonlinear polymer.

6.4 Measurement of on-chip nonlinear optical loss of molecular system

The absolute intra-cavity nonlinear loss can deduced from the relative decouplings using eq.5.4. The 2.47 dB silicon-only decoupling corresponds to 1.81 dB/cm of nonlinear loss while the 4.5 dB organic-only decoupling corresponds to 7.29 dB/cm of nonlinear loss, giving a ratio of 4.02 between the two. Due to the photobleaching this is corresponds to a lower bound on the organic TPA coefficient of $\beta_{o-TPA} \geq 18.8$ cm/GW assuming a confinement factor of 0.3. We believe that is remarkable that it is only slightly lower than the previously measure value of 22 cm/GW in free-standing organic polymer. The fact that the polymer is almost completely photobleached in the course of one HPP scan suggests that the actual TPA strength is significant greater than the lower bounded determined here.

6.5 Photo-instability of organic polymers

Next we inspect more closely the photobleaching process by taking and extended series of alternating LP and HP scans. Figure 6.5(a) shows the full series of scans taken of the resonance shown in figure 6.4, labeled (1)-(8). The three traces from figure 6.4 correspond to traces (4), (5) and (7), respectively. Figure 6.5(a) shows an addition three initial LPP scans (1)-(3), designated as "Pre-HP*". The first HP scan is designated HP*. The scans after this are designated "Post-HP*". The first observation is a translation of the resonance with every subsequent scan. The translations are largest after the HPP scans but even
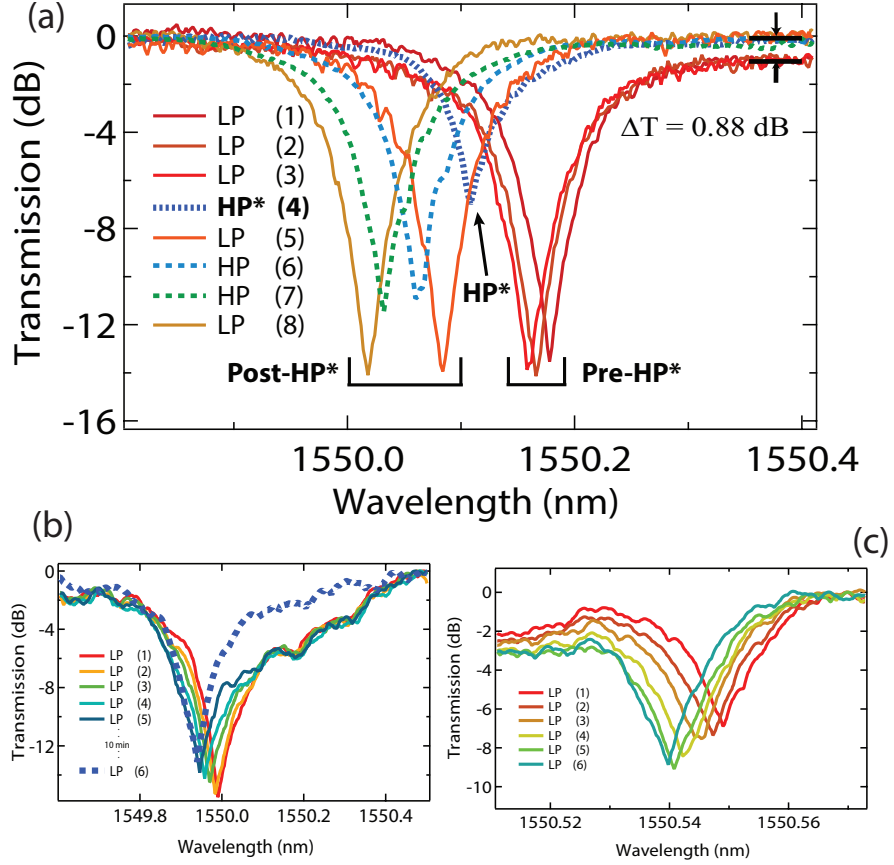
Figure 6.5: Time series scans of polymer-cavity system and high (dotted) and low (solid) powers.(a) Series of 8 scans in time order indicated shows photobleaching effects even at low power and much stronger photobleaching after high power power scan resulting in change in both the linear and nonlinear indices. Highest decoupling seen for first high power scan. Subsequent high power scans see significantly reduced decoupling. (b, c) Shift of linear resonance with low power scans. Final scan at low power after 10 minutes indicate thermal changes in polymer cladding.

the first three LP scans cause a slight drift. This translation is interpreted as a nonreversible photobleaching of the organic polymer which changes both the nonlinear and linear index of the polymer. The nonreversability of the effect is confirmed by the fact that the resonance does not shift back to it original wavelength after waiting an extended amount of time. In addition to the translation of the resonant wavelength, the photobleaching also changes the shape of the resonance evidences by the 0.88 dB offset between the off-resonant backgrounds between the Pre-HP* and the Post-HP* scans.

Figure 6.5(a) lends to a fairly straight forward interpretation of the photobleaching process and its effect on the cavity resonance, which is that the photobleaching changes the nonlinear loss and linear index but doesn't not change the linear loss evidenced by the fact that the LP scans if part (a) all have the same extinction. However this interpretation is not true for every device and resonance. Figures 6.5(b,c) show two resonances where we have only taken LP scans. The resonances shift with the same rate as in part (a) but there is also a associated change in the on-resonance transmission which is not seen in the LPP scans. This suggest that the linear loss is being altered. The direction of the on-resonance transmission change in (b) and (c) suggest that the linear loss is increasing with scans corresponding to the interpretation that in (c) the increasing linear loss is bringing an over-coupled resonance into critical coupling and in (b) that a critically coupled resonances is sent into the under-coupled regime.

However, the full picture could me far more complicated since the change in linear index will also change the mode volume which would change the geometric coupling rate. Finally, the another relevant process is that of heating. This is deduced from the last trace in (b) that is taken 10 minutes after the first 5, which were taken in quick succession. The noticeable change in the shape

of the resonance indicates that heating leads to addition linear losses. Heating may also affect the physical stability of the polymer causing it distort leading to unpredictable effects on the resonance structure.

CHAPTER 7

CONCLUSION

This thesis has focused on the implementation of nonlinear optics in micro-resonator cavities revolving around the two major themes: 1) nonlinear absorption aided Zeno all-optical switching and 2) the generation of broadband phase-locked frequency combs and cavity solitons. The miniaturization of optical cavities has enabled nonlinear dynamics at much lower pump powers and the scalability afforded by integrated fabrication allows complex architectures and functionalities unavailable with bulk- and fiber-based devices with the potential for chip-based optical computation, simulation and signal processing.

7.1 Zeno-based all-optical switching

The demonstration of Zeno-based all-optical switching opens a new path for exploring chip-based optical switching using absorptive processes, complimenting the existing refractive index based devices. There are several paths to explore. For Raman-based Zeno switching first is the integration and simultaneous use of both broadband Kerr-refractive and narrowband Raman-absorptive effects for switching and modulation. Such a device would allow even greater run-time tailoring of a micro-resonator's resonance properties. Second, is the improved implementation of a cascaded multi-ring device. Further engineering of the fabrication process and increased control over the waveguide loss, dispersion and geometric coupling can lead to a new type of compact switching fabric. Also, investigation of other materials with strong narrowband Raman features such as diamond may lead to still better performing Raman-based Zeno

switches.

Organic nonlinear materials, while having much stronger nonlinearities than crystals and glasses suffers from higher linear losses in addition to the perennial issue of photo-degradation and thermal effects. However, encapsulation methods when the polymer is sealed off from oxygen sources may improve stability significantly. Additionally, use of a more rigid host material may relieve the thermal distortion of the PMMA host polymer. An important next step is to demonstrate prolonged stability of nonlinear organic materials in an on-chip platform. In addition to encapsulation and improved hosting a concerted effort should be made within the field of organic nonlinear optics to solve the challenge posed by photo-degradation.

7.2   Micro-resonator comb and cavity solitons

Micro-resonator based frequency combs and cavity soliton is a fairly nascent field but is quickly gaining momentum. The number of material platforms for the generation of combs is steadily increasing with the recent introduction of aluminum nitride, diamond and silicon. Soon we may see combs in silicon carbide and other electro-optically active materials. Furthermore, in the few years since temporal cavity solitons have been observed in fiber cavities and micro-resonator frequency combs they have already demonstrated incredible potential in a wide range of applications ranging from optical to RF conversion, on-chip sensing and metrology, multi-wavelength generation and optical memory functionality. But this likely is only the tip of the iceberg of applications and devices that may arise from cavity soliton based technologies. Still unexplored are the various multi-soliton interactions such as soliton collisions, fusion and

precipitation and condensation processes. The strong phase sensitivity of cavity solitons may allow more exquisite control of these processes than is possible in dissipative laser soliton systems.

The work presented in this thesis is even more nascent with respect to the broader frequency comb and cavity soliton fields. Many of the ideas are still being distilled and many questions unanswered. The synchronization of multiple cavity soliton combs presents the most tangible next steps to take, namely the design and fabrication of two- and three-ring devices to investigate the experimental parameters in which cavity soliton synchronization can occur. Extending naturally from two- and three-ring devices will be N-ring and NxN-ring devices in which to explore topological and transport effects in the nonlinear, chaotic and solitonic regimes.

In particular, it has been shown that cavity solitons are associated with the homoclinic snaking bifurcation in the Lugiato-Lefever equation [43], a type of bifurcation that is closely linked with excitable systems including neural networks. These systems experience large excursions (firings) in phase space for above threshold perturbations before returning to the rest state and experience a refractory period during it cannot fire again. Thus a scalable network of cavity soliton combs is an ideal platform in which to explore neural networks and neuro-memetic computing.

The work in laser-gain driven cavity soliton formation offers important insight into the relation between traditional saturable absorber based laser modelocking and cavity soliton modelocking in parametric oscillators. An important property of cavity soliton is their addressability, i.e. their ability to be written and stably persist for an indefinite amount of time. An important question to answer is whether laser-gain cavity solitons have the same kind of addressability

as parametrically driven cavity solitons. Additionally, our work demonstrates a micro-resonator based laser capable achieving large bandwidth pulses with much narrower gain bandwidths. There is already an effort by several groups to engineer erbium and ytterbium doped silion nitride waveguides with the view of creating micro-ring based lasers. Our work shows that with proper dispersion engineering such a platform can generate even wider spectra that simply the gain bandwidth of the gain medium.

Finally, perhaps the most nuanced of the results presented in this thesis, the synchronization theory of cavity soliton formation and the parametric synchronization equations that describe its dynamics offer new insight into the inner mechanisms of the formation of a cavity soliton. The two key observations, that the comb phases anti-symmetrize before they synchronize and that the pump phase is offset from the rest of the comb phase profile, raise questions of how the system responds when all or select number of modes are perturbed from their steady state and what roles the phase offset and phase anti-symmetrization play in the re-stabilization. There are also unanswered questions about the PSEs themselves, for example the role of the $1/p$ factor in the phase different equations and the role of higher order dispersions terms. Generalizing the PSEs we can add in the effects of the non-pump FWM processes and investigate their role in the formation and stability of cavity solitons. Furthermore, some parameter regimes of the PSEs have produced phase profiles with multiple phase-offset modes and phase-steps, similar to those states that have been measured by Del'Haye *et al.* [31], and are the subject of ongoing work.

Looking beyond optical cavity soliton system, in saturable absorption based modelocked lasers the cosine in Eq.A.6 is replaced by a sine and phase synchronization is possible without a strong coherent pump field. Such a system may

provide insight into the differing phase dynamics of cavity solitons versus dissipative solitons. Broader still, we believe that given the generality of the root equation of the LLE, which is the complex Ginzburg-Landau equation and the intimate link between dissipative solitons with the broader fields of dissipative structures and nonequilibrium thermodynamics, we expect that this synchronization model may provide insight into the phase transition dynamics in a wide range of physical systems.

Coming from the mathematical point of view, frequency comb modelocking constitutes a new form of synchronization that has not been studied before, namely the synchronization of a massively multi-modal distribution of oscillators, such that it is perhaps more appropriate to call this phenomenon syncopation. This observation begs the question whether a generalized multi-modal population of oscillators with nearly equidistantly spaced natural frequencies can spontaneously syncopate and whether their couplings will also be constrained by energy and momentum conservation as is the case with FWM-based cavity soliton formation.

7.3   Closing remarks

It is an exciting time to be working in the field of integrated nonlinear optics. New capabilities in fabrication and numerics is enabling new devices and insights. I trust that this work will be a valuable and timely contribution to the progress of optical science and technology.

DERIVATION OF THE LLE-PHASE EQUATION

Here I use the notation from Chembo & Menyuk's [92] paper on the LL-equation to perform a fully rigorous derivation of a general modal phase equation. From this phase equation and assuming a strong coherent pump I derive a pair of equations which we term the parametric synchronization equations which explained in chapter 3.

The three major insights in the derivation that is not easily seen through the main text are 1) that the PD term has the effect of symmetrizing the phase profile about the injected pump phase and 2) this PD induced symmetrization allows the PND term to be recast in such a way where the two degrees of freedom become separable, which in turns allows the triple sum to be simplified into a single sum and 3) that by normalizing the phase-difference $\delta_p/p \rightarrow \delta_p$ variable allows us to remove the index dependence of the average phase difference order parameter and allows us to define a global order parameter for the average phase difference.

Start of with the LL-equation and the field:

$$\frac{\partial A}{\partial t} = -\frac{\Delta\omega_o}{2}A - i\sigma A + \frac{\Delta\omega_o}{2}F_o - ig_o|A|^2A - \xi_1\frac{\partial A}{\partial\theta} - i\frac{\xi_2}{2}\frac{\partial^2 A}{\partial\theta^2} \tag{A.1}$$

$$\frac{\partial A}{\partial t} = -\frac{\Delta\omega_o}{2}A - ig_o|A|^2A - \xi_1\frac{\partial A}{\partial\theta} - i\frac{\xi_2}{2}\frac{\partial^2 A}{\partial\theta^2} \tag{A.2}$$

$$\boxed{\frac{\partial A}{\partial t} = -i\frac{\xi_2}{2}\frac{\partial^2 A}{\partial\theta^2} - ig_o|A|^2A} - \frac{\Delta\omega_o}{2}A \tag{A.3}$$

$$\boxed{\frac{\partial A}{\partial t} = -i\frac{\xi_2}{2}\frac{\partial^2 A}{\partial \theta^2} - ig_o|A|^2 A} - \frac{\Delta\omega_o}{2}A \qquad (A.4)$$

$$A(t,\theta) = \sum_l^N A_l e^{i(\omega_l - \omega_o)t - i(l - l_o)\theta} e^{i\phi'_l(t)} \qquad (A.5)$$

$$(A.6)$$

θ is the angle around the circumference of the cavity and ξ's correspond to the dispersion coefficients. ω_o and l_o are the frequency and the mode number of the pumped mode, F_o is the amplitude of the pump, σ is the detuning of the pump from the center of the pumped resonance and g_o is the four-wave mixing gain coefficient.

Since we are interested in the phase dynamics of the discrete modes we explicitly pull out the phase of each mode as $\phi'_l(t)$ and assume that A_l is a pure real.

We can transform into the group velocity frame by using $\theta \to \theta - \xi_1 t$, and by expanding the modal frequencies explicitly in terms of the mode number and dispersion ($\omega_l \approx \omega_{l_o} + \xi_1(l - l_o) + \frac{1}{2}\xi_2(l - l_o)^2$) we obtain:

$$\frac{\partial A}{\partial t} = -\frac{\Delta\omega_o}{2}A - i\sigma A + \frac{\Delta\omega_o}{2}F_o - ig_o|A|^2 A - i\frac{\xi_2}{2}\frac{\partial^2 A}{\partial \theta^2}$$

$$\frac{\partial A}{\partial t} = -\frac{\Delta\omega_o}{2}A - ig_o|A|^2 A - i\frac{\xi_2}{2}\frac{\partial^2 A}{\partial \theta^2}$$

101

$$A(t, \theta) = \sum_l^N A_l e^{i\xi_1(l-l_o)t + \frac{i}{2}\xi_2(l-l_o)^2 t - i(l-l_o)\theta} e^{i\phi'_l(t)}$$

Inject the field into the LEFT HAND SIDE of the LL-equation, we begin to use different indices to keep the notation clear:

$$\frac{\partial A}{\partial t} = \frac{\partial}{\partial t}\left[\sum_p^N A_p e^{i\xi_1(p-l_o)t + \frac{i}{2}\xi_2(p-l_o)^2 t + i(p-l_o)\theta} e^{i\phi'_p(t)}\right]$$

$$= \sum_p^N e^{-i(p-l_o)\theta} e^{i\xi_1(p-l_o)t + \frac{i}{2}\xi_2(p-l_o)^2 t + i\phi'_p(t)}\left[\frac{\partial A_p}{\partial t} + A_p[2i\xi_1(p-l_o) + i\frac{\partial}{\partial t}\left(\phi'_p(t) + \frac{1}{2}\xi_2(p-l_o)^2 t\right)]\right]$$

Here we assume a slowly varying envelope approximation and drop the time derivative of A_p. We also notice that the dependance on the second order dispersion can be lumped with the $\phi'(t)$ term without loosing generality, thus we make the transformation $\phi'_p(t) + \frac{1}{2}\xi_2(p-l_o)^2 t \to \phi_p(t)$.

$$LHS = \sum_p^N A_p e^{i\xi_1(p-l_o)t - i(p-l_o)\theta + i\phi_p(t)}\left[2i\xi_1(p-l_o) + i\dot{\phi}_p(t)\right]$$

The RIGHT HAND SIDE:

$$-\frac{\Delta\omega_o}{2}A - i\sigma A + \frac{\Delta\omega_o}{2}F_o - ig_o|A|^2 A - i\frac{\xi_2}{2}\frac{\partial^2 A}{\partial\theta^2}$$

$$RHS = -\frac{\Delta\omega_o}{2}A - ig_o|A|^2 A - i\frac{\xi_2}{2}\frac{\partial^2 A}{\partial\theta^2}$$

We will ignore the pump terms for now. We'll address each term one by one, again using different indices for each term:

1)

$$-\frac{\Delta\omega_o}{2}A = -\frac{\Delta\omega_o}{2}\sum_f^N A_f e^{i\xi_1(f-l_o)t+\frac{i}{2}\xi_2(f-l_o)^2t-i(f-l_o)\theta}e^{i\phi'_f(t)}$$

2)

$$ig_o|A|^2A = ig_o\sum_l^N\sum_m^N\sum_n^N A_lA_mA_n e^{2i\xi_1[(l-l_o)-(m-l_o)+(n-l_o)]}e^{\frac{i}{2}\xi_2[(l-l_o)^2-(m-l_o)^2+(n-l_o)^2]}\times$$

$$e^{-i\theta[(l-l_o)-(m-l_o)+(n-l_o)]}e^{i[\phi'_l-\phi'_m+\phi'_n]}$$

We will leave this term unsimplified for now because the simplification will be much more apparent when we combine the two sides of the equation.

3)

$$-i\frac{\xi_2}{2}\frac{\partial^2 A}{\partial\theta^2} = -i\frac{\xi_2}{2}\sum_q^N A_q e^{i\xi_1(q-l_o)t+\frac{i}{2}\xi_2(q-l_o)^2t}e^{i\phi'_q(t)}\frac{\partial^2}{\partial\theta^2}(e^{-i(q-l_o)\theta})$$

$$= i\frac{\xi_2}{2}\sum_q^N A_q e^{i\xi_1(q-l_o)t+\frac{i}{2}\xi_2(q-l_o)^2t-i(q-l_o)\theta}e^{i\phi'_q(t)}(q-l_o)^2$$

When we combine the LHS and the RHS we notice that we can factor from each term a quantity equal to the field $A(t)$. This is true even though we used different indices for each term since the sums are not coupled to each other (i.e. $f, q = p$). The only term we have to be careful with is the kerr terms since the sums are coupled. Here we "factor" by dividing by the same quantity.

$$\sum_p^N A_p e^{i\xi_1(p-l_o)t-i(p-l_o)\theta+\frac{i}{2}\xi_2(p-l_o)^2t+i\phi'_p(t)}[2i\xi_1(p-l_o)+i\dot\phi_p(t) = -\frac{\Delta\omega_o}{2}+i\frac{\xi_2}{2}(p-l_o)^2$$

$$-ig_o\frac{|A|^2A}{A_p e^{i\xi_1(p-l_o)t-i(p-l_o)\theta+\frac{i}{2}\xi_2(p-l_o)^2t+i\phi'_p(t)}}]$$

$$\sum_p^N A_p e^{i\xi_1(p-l_o)t-i(p-l_o)\theta+\frac{i}{2}\xi_2(p-l_o)^2t+i\phi'_p(t)}[2i\xi_1(p-l_o)+i\dot\phi_p(t) = -\frac{\Delta\omega_o}{2}+i\frac{\xi_2}{2}(p-l_o)^2$$

$$-ig_o\frac{|A|^2A}{A_pe^{i\xi_1(p-l_o)t-i(p-l_o)\theta+\frac{i}{2}\xi_2(p-l_o)^2t+i\phi'_p(t)}}]$$

Here we come back to the kerr term and simplify it:

$$-ig_o\frac{|A|^2A}{A_pe^{i\xi_1(p-l_o)t-i(p-l_o)\theta+\frac{i}{2}\xi_2(p-l_o)^2t+i\phi'_p(t)}}$$

$$= ig_o\sum_l^N\sum_m^N\sum_n^N\frac{A_lA_mA_n}{A_p}e^{2i\xi_1[(l-l_o)-(m-l_o)+(n-l_o)-(p-l_o)]}e^{\frac{i}{2}\xi_2[(l-l_o)^2-(m-l_o)^2+(n-l_o)^2-(p-l_o)^2]}\times$$

$$e^{-i\theta[(l-l_o)-(m-l_o)+(n-l_o)-(p-l_o)]}e^{i[\phi'_l(t)-\phi'_m(t)+\phi'_n(t)-\phi'_p(t)]}$$

Energy conservation requires $l - m + n - p = 0$ thus the first and third exponentials both equal unity. Again, combine the second order terms with the ϕ' terms and making the transformation $\phi'_{l,m,n,p}(t) + \frac{1}{2}\xi_2(l, m, n, p - l_o)^2t \rightarrow \phi_{l,m,n,p}(t)$

$$= ig_o\sum_l^N\sum_m^N\sum_n^N\frac{A_lA_mA_n}{A_p}e^{i(\phi_l(t)-\phi_m(t)+\phi_n(t)-\phi_p(t))}$$

Putting this back in the full equation we obtain:

$$\dot{\phi}_p(t) = i\frac{\Delta\omega_o}{2} - 2\xi_1(p - l_o) + \frac{\xi_2}{2}(p - l_o)^2 - g_o\sum_l^N\sum_m^N\sum_n^N\frac{A_lA_mA_n}{A_p}e^{i(\phi_l(t)-\phi_m(t)+\phi_n(t)-\phi_p(t))}$$

A.1   Derivation part II

In the part I we were able to derive this expression for the phases:

$$\dot{\phi}_p(t) = i\frac{\Delta\omega_o}{2} + \frac{\xi_2}{2}p^2 + O(\frac{\xi_3}{3}p^3) - g_o \sum_l^N \sum_m^N \sum_n^N \frac{A_l A_m A_n}{A_p} e^{i(\phi_l(t)-\phi_m(t)+\phi_n(t)-\phi_p(t))}$$

$$\dot{\phi}_p(t) = i\frac{\Delta\omega_o}{2} - 2\xi_1 p + \frac{\xi_2}{2}p^2 + O(\frac{\xi_3}{3}p^3) - g_o \sum_l^N \sum_m^N \sum_n^N \frac{A_l A_m A_n}{A_p} e^{i(\phi_l(t)-\phi_m(t)+\phi_n(t)-\phi_p(t))}$$

Our collaborator Steve Strogatz pointed out that this expression results in a complex value for the phases, which is not physical. My advisor Alex Gaeta suggested that we separate the real and imaginary parts of the equation and solve for the real part of the phase, which is what we were really looking for in the beginning. First, I will solve for the real and imaginary parts of the equation. Also, I've included the existence of higher order dispersion terms; as it turns out they eventually play a meaningful role.

A.2   The Real Part of the Phase Equation

First, let

$$\phi_{lp}(t) = \phi_l(t) - \phi_m(t) + \phi_n(t) - \phi_p(t)$$

$$\mathcal{A}_{lp}^2 = \frac{A_l A_m A_n}{A_p}$$

Also,

$$\phi_p(t) = \phi_p(t) + i\alpha_p(t)$$

and

$$-g_o \sum_l^N \sum_m^N \sum_n^N \frac{A_l A_m A_n}{A_p} e^{i(\phi_l(t)-\phi_m(t)+\phi_n(t)-\phi_p(t))} = -g_o \sum_{lmn}^N \mathcal{A}_{lp}^2 exp(i\phi_{lp} - \alpha_{lp})$$

105

Focusing on the coupling term, the exponential can be split into two parts

$$= -g_o \sum_{lmn}^{N} \mathcal{A}_{lp}^2 [Cos(\phi_{lp}) + iS in(\phi_{lp})] exp(-\alpha_{lp})$$

Putting all the terms together:

$$\dot{\phi}_p^r + i\dot{\phi}_p^i = i\frac{\delta\omega_o}{2} - 2\xi_1 p + \frac{\xi_2}{2}p^2 + O(\frac{\xi_3}{3}p^3) - g_o \sum_{lmn}^{N} \mathcal{A}_{lp}^2 [Cos(\phi_{lp})exp(-\alpha_{lp}) + iS in(\phi_{lp})exp(-\alpha_{lp})]$$

Equating the real and imaginary terms:

$$REAL : \dot{\phi}_p = -2\xi_1 p + \frac{\xi_2}{2}p^2 + O(\frac{\xi_3}{3}p^3) - g_o \sum_{lmn}^{N} \mathcal{A}_{lp} Cos(\phi_{lp})exp(-\alpha_{lp})$$

$$IMAG : \dot{\alpha}_p = \frac{\delta\omega_o}{2} - g_o \sum_{lmn}^{N} \mathcal{A}_{lp}S in(\phi_{lp})exp(-\alpha_{lp})$$

$$REAL : \dot{\phi}_p = \frac{\xi_2}{2}p^2 + O(\frac{\xi_3}{3}p^3) - g_o \sum_{lmn}^{N} \mathcal{A}_{lp} Cos(\phi_{lp})exp(-\alpha_{lp})$$

$$IMAG : \dot{\alpha}_p = \frac{\delta\omega_o}{2} - g_o \sum_{lmn}^{N} \mathcal{A}_{lp}S in(\phi_{lp})exp(-\alpha_{lp})$$

The REAL equation can be further simplified by going into the rotating wave frames of ALL of the modes $\phi_p \rightarrow \phi_p - 2\xi_1 pt$, and by assuming that there is uniform loss. Also, to simplify the notation we drop the r superscript with the understanding that we are looking at the real phases.

$$\dot{\phi}_p = \frac{\xi_2}{2}p^2 + O(\frac{\xi_3}{3}p^3) - g_o \sum_{lmn}^{N} \mathcal{A}_{lp}^2 Cos(\phi_l - \phi_m + \phi_n - \phi_p)$$

A.3 Stable Solution with a Strong Pump

This equation does not have globally stable solutions. The Cosine coupling term has the effect of pulling its argument towards a value of $-\pi/2$, but this criterion cannot be satisfied by all energetically appropriate combinations of phases at the same time. However, if we introduce a strong pump the system becomes simplifiable!

By strong pump I mean let mode 0 be γ $(10\rightarrow100)$ times stronger than every other mode. This does two things: 1) It makes it reasonable to approximate the strength of every other comb mode as A, in which case the pump is γA, and 2) it separates the sum of FWM terms into different classes of terms based on how many pump photons are involved in it.

Pump degenerate (PD) processes, where two pump photons annihilate to create two symmetric comb mode photons, have a relative strength of γ^2 compared to processes that do not involve the pump at all. Similarly pump nondegenerate (PND) processes, where one pump photon and one comb photon annihilate to generate yet two other energetically appropriate comb photons, has relative strength of γ. The inverse of these processes have relatives strengths of 1 and γ^{-1}, respectively. In order the 5 classes of process have relative strengths γ^2, γ, 1, γ^{-1} and 1. Since we are concerned with only net flow of phase information (i.e. photons/energy) we neglect all process with relative strengths of unity and less.

$$\dot{\phi}_p = \frac{\xi_2}{2}p^2 + O(\frac{\xi_3}{3}p^3) - g_o A^2 \gamma^2 cos(2\phi_0 - (\phi_p + \phi_{-p})) - g_o A^2 \gamma \sum_{m=1-p}^{p-1} Cos(\phi_0 + (\phi_m - \phi_{m-p}) - \phi_p)$$

We notice several things from this simplification:

1) First, we've restricted the sum from $m = 1 - p$ to $p - 1$ to make the algebraic manipulations clearer. This restriction will be relaxed at the end so that all the terms are accounted for.

2) There is only one PD term and it has the value $(\phi_p + \phi_{-p})$, a phase average of the pth modes symmetric about the pump, in the argument of the coupling term. This suggests that we may get somewhere by solving for the phase averages of the pth symmetric pair of modes.

3) If the phase averages are a meaning variable of the system then it makes sense that the orthogonal variable of the phase differences $(\phi_p - \phi_{-p}))$ are also meaningful. We see that if we take this difference in phases the PND terms simplify using a few trig identities.

A.4 Phase Average Equation

Let's consider the phase averages first. We define the average phase of the pth modes symmetric on either side of the pump as: $\bar{\phi}_p = (\phi_p + \phi_{-p}))/2$. Adding the above equation in such a way:

$$\frac{\dot{\phi}_p + \dot{\phi}_{-p}}{2} = \boxed{\dot{\bar{\phi}}_p = \tfrac{\xi_2}{2}p^2 - 2g_oA^2\gamma^2Cos[2(\phi_0 - \bar{\phi}_p)]}$$

$$-g_oA^2\gamma \sum_{m=1-p}^{p-1} [Cos(\phi_0 + (\phi_m - \phi_{m-p}) - \phi_p) + Cos(\phi_0 + (\phi_{-m} - \phi_{p-m}) - \phi_{-p})]$$

The equation has contributions from both the PD and PND terms but the early evolution is dominated by the PD term. This is because 1) the PD term is

γ times stronger and more importantly 2) in the early evolution the phases are still random and the PND terms sum to zero on average. The effect of the term is to symmetrize the phases of symmetric modes such that $(\phi_p - \phi_o) \approx -(\phi_{-p} - \phi_o)$. Also, this term also predicts that the pump phase will be offset from the rest of the phase profile by $\pi/4 < \phi_{off} < \pi/2$ in order to create a Sine-like coupling term and to compensate for dispersion. We pause from the $\dot{\phi}_p$ equation for now and consider the phase difference equation.

A.5 Phase Difference Equation

We define the phase difference of the pth modes symmetric on either side of the pump as: $\delta'_p = (\phi_p - \phi_{-p}))/2$. Adding the above equation in such a way:

$$\frac{\dot{\phi}_p - \dot{\phi}_{-p}}{2} = \dot{\delta}'_p = \frac{\xi_3}{3} p^3 - 2 g_o \mathcal{A}^2 \gamma \sum_{m=1}^{p-1} [Cos(\phi_0 + (\phi_m - \phi_{m-p}) - \phi_p) - Cos(\phi_0 + (\phi_{-m} - \phi_{p-m}) - \phi_{-p})]$$

The PD terms cancel each other out along with every other even term. We are only left with the odd terms and the PND terms. Since the terms are also symmetric for $\pm m$ we can begin the sum at $m = 1$ and put a factor of 2 in front. Looking at the PND terms carefully we see that we have a sum of the form $Cos(a+b-d) - Cos(a+c-e) = -2 Sin(\frac{b-c}{2} - \frac{d-e}{2}) Sin(a - \frac{b+c}{2} - \frac{d+e}{2})$. Letting $(\phi_m - \phi_{m-p})$ and $(\phi_{-m} - \phi_{p-m})$ be δ'_{mp} and δ'_{-mp}, respectively and $\delta'_p = (\phi_p - \phi_{-p}))/2$, the sum of the two Cosine terms becomes:

$$-2 Sin(\frac{\delta'_{mp} - \delta'_{-mp}}{2} + \delta'_p) Sin(\phi_0 - \frac{\delta'_{mp} + \delta'_{-mp}}{2} - \bar{\phi}_p)$$

We recall from the phase average equation that $(\phi_p - \phi_o) \approx -(\phi_{-p} - \phi_o)$. This means that $\delta_{-mp} \approx -\delta_{mp}$, and since $\delta'_{mp} = \delta'_m - \delta'_{m-p}$, the equation for the phase average simplifies to:

$$\dot{\delta}'_p = \frac{\xi_3}{3}p^3 + 2g_o\gamma A^2 S\,in(\phi_0 - \bar{\phi}_p)\sum_{m=1}^{p-1} S\,in(\delta'_m + \delta'_{p-m} + \delta'_p)$$

We see that the coupling terms can now be further simplified by writing it the form of an order parameter.

$$R(t)e^{i(\delta'_{po}-\delta'_p)} = \frac{1}{p-1}\sum_{m=1}^{p-1} e^{i(\delta'_m + \delta'_{p-m}-\delta'_p)}$$

The value δ'_{po} is given by the average of the values $(\delta'_m + \delta'_{m-p})$ for $m = 1$ to $(p-1)$, but each δ'_m occurs twice the expression for δ'_{po} simplifies to:

$$\delta'_{po} = \frac{2}{p-1}\sum_{m=1}^{p-1} \delta'_m$$

The function $R_d(t)$ is:

$$R(t) = \frac{2}{p-1}|\sum_{m=1}^{p-1} e^{i(\delta'_m - \delta'_{m0})}|$$

The average phase difference δ'_{m0} appears in the argument because it indicates a linear phase shift across the modes and needs to be subtracted out in order to get the correct value for the phase coherence. This allows us to write

$$\dot{\delta}'_p = \frac{\xi_3}{3}p^3 + 2g_o\gamma A^2 R(t)S\,in(\phi_0 - \bar{\phi}_p)S\,in(\delta'_{po} - \delta'_p)$$

But we're not done! This equation has all the functional forms of the Kuramoto model, however, it still has the annoying problem that the order parameter depends on p and is not, in it current form, a function of the entire system. Next we make two manipulations that will both simplify the notation and allow us to write the order parameter independently of the mode number p.

1) We let $\delta_p = \delta'_p / p$ such that

$$p\dot{\delta}_p = \frac{\xi_3}{3} p^3 + 2 g_o \gamma A^2 R(t) S\,in(\phi_0 - \bar{\phi}_p) S\,in[p(\delta_o - \delta_p)]$$

and,

$$\delta_o = \frac{2}{p(p-1)} \sum_{m=1}^{p-1} m\delta_m$$

2) We let the sum upper limit go to $N/2$ to include all the terms and to make δ_o independent of p, for large N.

$$\delta_o = \frac{8}{N^2} \sum_{m=1}^{N/2} m\delta_m$$

Likewise

$$R(t) = \frac{2}{N} |\sum_{m=1}^{N/2} e^{im(\delta_m - \delta_0)}|$$

Finally, we can write the final form of the phase difference equation and the order parameter:

$$\boxed{\dot{\delta}_p = \frac{\xi_3}{3} p^2 - \frac{2 g_o \gamma A^2}{p} R(t) S\,in(\phi_0 - \bar{\phi}_p) S\,in[p(\delta_p - \delta_o)]}$$

$$\boxed{R(t) = \frac{2}{N} |\sum_{m=1}^{N/2} e^{im(\delta_m - \delta_0)}|}$$

$$\boxed{\delta_o = \frac{8}{N^2} \sum_{m=1}^{N/2} m\delta_m}$$

A.6   Phase Average Equation Cont'd

$$\dot{\bar{\phi}}_p = \frac{\xi_2}{2} p^2 - 2 g_o A^2 \gamma^2 Cos[2(\phi_0 - \bar{\phi}_p)] - g_o A^2 \gamma \sum_{m=1-p}^{p-1} [Cos(\phi_0 + (\phi_m - \phi_{m-p}) - \phi_p) + Cos(\phi_0 + (\phi_{-m} - \phi_{p-m}) - \phi_{-p})]$$

We return to the phase average equation to clear up the PND part of the equation. We can tell by inspection that the same analysis that worked for the phase

111

difference equation will apply here, the only difference being the addition of the Cosines resulting in a product of Cosines.

$$\dot{\bar{\phi}}_p = \frac{\xi_2}{2}p^2 - 2g_o\mathcal{A}^2\gamma^2 Cos[2(\phi_0 - \bar{\phi}_p)] - g_o\gamma\mathcal{A}^2 R(t)Cos(\phi_0 - \bar{\phi}_p)Cos(p(\delta_p - \delta_o))$$

A.7   Summary

All the equations together:

$$\boxed{\dot{\bar{\phi}}_p = \frac{\xi_2}{2}p^2 - 2g_o\mathcal{A}^2\gamma^2 Cos[2(\phi_0 - \bar{\phi}_p)] - g_o\gamma\mathcal{A}^2 R(t)Cos(\phi_0 - \bar{\phi}_p)Cos(p(\delta_p - \delta_o))}$$

$$\boxed{\dot{\delta}_p = \frac{\xi_3}{3}p^2 - \frac{2g_o\gamma\mathcal{A}^2}{p}R(t)S\,in(\phi_0 - \bar{\phi}_p)S\,in[p(\delta_p - \delta_o)]}$$

$$\boxed{R(t) = \frac{2}{N}|\sum_{m=1}^{N/2} e^{im(\delta_m - \delta_0)}|}$$

$$\boxed{\delta_o = \frac{8}{N^2}\sum_{m=1}^{N/2} m\delta_m}$$

BIBLIOGRAPHY

[1] Genesis 1:1-3, The Holy Bible, English Standard Version, Crossway Bibles (2001).

[2] J.C. Maxwell, A Dynamical Theory of the Electromagnetic Field, Philosophical Transactions of the Royal Society of London, **155,** 459 (1865)

[3] A. Nitkowski, A. Baeumner, M. Lipson, On-chip spectrophotometry for bioanalysis using microring resonators, Optics Express **2,** 138424 (2011).

[4] T. Fortier, M. Kirchner, F. Quinlan, J. Taylor, J. Bergquist, T. Rosenband, N. Lemke, A. Ludlow, Y. Jiang, C. Oates, A. Diddams, Generation of ultrastable microwaves via optical frequency division, Nat. Photon. **5,** 425 (2011).

[5] S. Ashley, Beam Weapons Get Real,Sci. American **296,** 28 (2007) Nat. Photon. **5,** 425 (2011).

[6] O. Svelto, Principles of Lasers, 5th Ed. Springer-Verlag (2010).

[7] B. Saleh, M. Teich, Fundamentals of Photonics. Wiley (2007).

[8] M. Lipson, Silicon photonics: An excercise in self control. Nat. Photon, **1,** 18, (2007).

[9] K. J. Vahala, Optical microcavities, Nature **424,** 839 (2003).

[10] M. A. Foster, J. Levy, O. Kuzucu, K. Saha, M. Lipson, A. Gaeta, Silicon-based monolithic optical frequency comb source, Opt. Express **19**, 14233 (2011).

[11] H. A. Haus, Modelocking of lasers IEEE Quant. Electr. **6**, 1173 (2000).

[12] K. Saha Y. Okawachi, B. Shim, J. Levy, R. Salem, A. Johnson, M. Foster, M. Lipson, M. Lamont, M. Lipson, A. Gaeta, Modelocking and femtosecond pulse generation in chip-based frequency combs. Opt. Express **21**, 1335 (2013).

[13] T. Herr, V. Brasch, J. Jost, C. Wang, N. Kondratiev, M. Gorodetsky, T. Kippenberg, Temporal solitons in optical microresonators, Nat. Photon. **8**, 145 (2014).

[14] F. Leo, S. Coen, P. Kockaert, S.-P. Gorza, P. Emplit, M. Haelterman, Temporal cavity solitons in one-dimensional Kerr media as bits in an all-optical buffer, Nat. Photon. **4**, 471 (2010).

[15] A. E. Motter, S. Myers, M. Anghel, T. Nishikawa, Spontaneous synchrony in power-grid networks, Nature Phys. **9,** 191 (2013).

[16] S. H. Strogatz, From Kuramoto to Crawford: exploring the onset of synchronization in populations of coupled oscillators, Physica D **143,** 1 (2000).

[17] G. Engel, T. Calhoun, E. Read, T. Ahn, T. Mancal, Y. Cheng, R. Blankenship, G. Fleming, Evidence for wavelike energy transfer through quantum coherence in photosynthetic systems, Nature **446,** 7137 (2007).

[18] S. Foreman, K. Holman, D. Hudson, D. Jones, J. Ye, Remote transfer of ultrastable frequency references via fiber networks, Rev. Sc. Instr. **78,** 021101 (2007).

[19] L.Lu, J. Joannopoulos, M. Saljacic, Topological photonics, Nat. Photon. **8,** 821 (2014).

[20] B. C. Jacobs and J. D. Franson, Phys. Rev. A **79,** 063830 (2009).

[21] Y. Chembo, N. Yu, Modal expansion approach to optical-frequency-comb generation with monolithic whispering-gallery-mode resonators, Phys. Rev. A **82,** 033801 (2010).

[22] V. R. Almeida, C. A. Barrios, R. R. Panepucci, M. Lipson, Nature **431,** 1081 (2004).

[23] K. Nozaki, T. Tanabe, A. Shinya, S. Matsuo, T. Sato, H. Hideaki, M. Notomi, Sub-femtojoule all-optical switching using a photonic-crystal nanocavity, Nature Photon. **4,** 477 (2010).

[24] B. G. Lee, A. Biberman, P. Dong, M. Lipson, and K. Bergman, All-optical comb switch for multiwavelength message routing in silicon photonic networks, IEEE Photon. Tech. Lett.**20,** 767 (1998).

[25] J. Cardenas, M. Foster, N. Sherwood-Droz, C. Poitras, H—. Lira, B. Zhang, A. Gaeta, J. Khurgin, P. Morton, M. Lipson, Wide-bandwidth continuously tunable optical delay line using silicon microring resonators, Opt. Express **18**, 26525 (2010).

[26] F. Xia L. Sekaric, Y. Vlasov, Ultracompact optical buffers on a silicon chip, Nat. Photon **1**, 65 (2007).

[27] Q. Fang, T. Liow, J. Song, K. Ang, M. Yu, G. Lo, D. Kwong, WDM multi-channel silicon photonic receiver with 320 Gbps data transmission capability, *et al.*, Opt. Express **18**, 5106 (2010).

[28] J. Levy, A. Gondarenko, M. Foster, A. Turner-Foster, A. Gaeta, M. Lipson, CMOS-compatible multiple-wavelength oscillator for on-chip optical interconnects, Nat. Photon. **4**, 37 (2010).

[29] A. Guarino, G. Poberaj, D. Rezzonico, R. Degl'Innocenti, P. Gunter, Electrooptically tunable microring resonators in lithium niobate, Nat. Photon. **1**, 407 (2007).

[30] P. Del'Haye, A. Schliesser, O. Arcizet, T. Wilken, R. Holzwarth, T. Kippenberg, Optical frequency comb generation from a monolithic microresonator, Nature **450**, 1214 (2007).

[31] P. Del'Haye, A. Coillet, W. Loh, K. Beha, S. Papp, S. Diddams, Phase Steps and Hot Resonator Detuning in Microresonator Frequency Combs, arXiv:**1405**.6972 (2014).

[32] C. Wang, T. Herr, P. Del'Haye, A. Schliesser, J. Hofer, R. Holzwarth, T. Hansch, N. Picque, T. Kippenberg, Mid-infrared optical frequency combs at 2.5m based on crystalline microresonators, Nat. Comm. **4**, 1345 (2012).

[33] B. Hausmann, I. Bulu, V. Venkataraman, P. Deotare, M. Loncar, Diamond nonlinear photonics, Nat. Photon. **8**, 369 (2014).

[34] A. Griffith, R. Lau, J. Cardenas, Y. Okawachi, A. Mohanty, R. Fain, Y. Lee, M. Yu, C. Phare, C. Poitras, A. Gaeta, M. Lipson, Silicon-Chip Mid-Infrared Frequency Comb Generation, arXiv:**1408**.1039 (2014).

[35] G. Agrawal, Nonlinear fiber optics, 3rd Ed., Elsevier (2007).

[36] M. Foster, A. Turner, J. Sharping, B. Schmidt, M. Lipson, A. Gaeta, Broadband optical parametric gain on a silicon photonic chip, Nature **441**, 960 (2006).

[37] Y. Okawachi, M. Lamont, K. Luke, D. Carvalho, M. Yu, M. Lipson, A. Gaeta, Optics Lett. **39**, 3535 (2014).

[38] A. M. Turing, The chemical basis of morphogenesis Phil. Trans. Royal. Soc., **237**, 37 (1952).

[39] Y. Okawachi, K. Saha, J. Levy, Y. Wen, M. Lipson, A. Gaeta, Octave-spanning frequency comb generation in a silicon nitride chip, Opt. Lett **36**, 3398 (2011).

[40] M. R. E. Lamont, Y. Okawachi, A. Gaeta, Route to stabilized ultrabroad-band microresonator-based frequency combs, Opt. Lett. **38**, 3478 (2013).

[41] T. Herr, K. Hartinger, J. Riemensberger, C. Wang, E. Gavartin, R. Holzwarth, M. Gorodetsky, T. Kippenberg, Universal formation dynamics and noise of Kerr-frequency combs in microresonators, Nat. Photon. **6**, 480 (2012).

[42] S. Coen, H. Randle, T. Sylvestre, M. Erkintalo, Modeling of octave-spanning Kerr frequency combs using a generalized mean-field LugiatoLefever model, Opt. Lett. **38**, 37 (2013).

[43] P. Parra-Rivas, D. Gomila, M. A. Matas, S. Coen, L. Gelens, Dynamics of localized and patterned structures in the Lugiato-Lefever equation determine the stability and shape of optical frequency combs, Phys. Rev. A **89,** 043813 (2014).

[44] N. Akhmediev, A. Ankiewicz, Dissipative Solitons: From Optics to Biology and Medicine, Springer (2008).

[45] P. Grelu, N. Akhamediev, Dissipative solitons for mode-locked lasers, Nat. Photon. **6**, 84 (2012).

[46] C. Godey, I. Balakireva, A. Coillet, Y. Chembo, Stability analysis of the spatiotemporal Lugiato-Lefever model for Kerr optical frequency combs in the anomalous and normal dispersion regimes, Phys. Rev. A **89,** 063814 (2014).

[47] g. Nicolis, I. Prigogine, Self-organization in nonequilibrium systems Wiley-Interscience (1977).

[48] S. Barland, J. Tredicce1, M. Brambilla, L. Lugiato, S. Balle, M.Giudici, T. Maggipinto, L. Spinelli, G. Tissoni, T. Kndl, M. Miller, R. Jger, Cavity solitons as pixels in semiconductor microcavities Nature **419,** 699 (2002).

[49] L. Lugiato, R. Lefever, Spatial Dissipative Structures in Passive Optical Systems, Phys. Rev. Lett **58,** 2209 (1987).

[50] I. Barashenkov, Y. Smirnov, Existence and stability chart for the ac-driven, damped nonlinear Schrdinger solitons, Phys. Rev. E **54,** 5707 (1996).

[51] L. Hargrove, R. Fork, M. Pollack, Locking of HeNe laser modes induced by synchronous intra-cavity modulation, Appl. Phys. Lett.**5,** 4 (1964).

[52] D. Olaosebikan, S. Yerci, A. Gondarenko, Kyle Preston, R. Li, L. Negro, M. Lipson, Absorption bleaching by stimulated emission in erbium-doped silicon-rich silicon nitride waveguides, Optics Lett. **36,** 4 (2011).

[53] Y. Gong, S. Yerci, R. Li, L. J. Vuckovic, Enhanced light emission from erbium doped silicon nitride in plasmonic metal-insulator-metal structures, Optics Express **17,** 20642 (2009).

[54] Y. Kuramoto, Chemical Oscillations, Waves and Turbulence. Springer-Verlag (1984).

[55] T. Wolmelsdorf, J. Schoffelen1, R. Oostenveld, W.Singer, R. Desimone, A. Engel, P. Fries, Modulation of Neuronal Interactions Through Neuronal Synchronization, Science. **316,** 1069 (2007).

[56] I. Kiss, Y. Zhai, J. Hudson *et al.*, Emerging Coherence in a Population of Chemical Oscillators, Science **296,** 5573 (2010).

[57] K. Weisenfeld, P. Colet, S. H. Strogatz, Synchronization Transitions in a Disordered Josephson Series Array, Phys. Rev. Lett. **76,** 3 (1996).

[58] G. Kozyreff, A. G. Vladimirov, P. Mandel, Global Coupling with Time Delay in an Array of Semiconductor Lasers, Phys. Rev. Lett. **85,** 18 (2000).

[59] F. X. Kartner, I. Jung, U. Keller, Soliton Mode-Locking with Saturable Absorbers, IEEE Quant. Electr. **2,** 540 (1996).

[60] A. Coillet and Y. K. Chembo, On phase-locking of Kerr combs, arXiv:**1401**.0930 (2014).

[61] W. Loh, P. DelHaye, S. Papp, S. Diddams, Phase and coherence of optical microresonator frequency combs, Phys. Rev. A **89,** 053810 (2014).

[62] X. Xue, Y. Xuan, Y. Liu, P.-H. Wang, S. Chen, J. Wang, D. Leaird, M. Qi, A. Weiner, Mode interaction aided excitation of dark solitons in microresonators constructed of normal dispersion waveguides, arXiv:**1404**.2865 (2014).

[63] W. J. Firth and C. O. Weiss, Cavity and Feedback Solitons, Opt. Photon. News **13**, 54 (2002).

[64] A. Coillet and Y. K. Chembo, Routes to spatiotemporal chaos in Kerr optical frequency combs, arXiv:**1401**.0927 (2014).

[65] S. Huang, G. Cirmi, J. Moses, K. Hong, S. Bhardwaj, J. Birge, L. Chen, E. Li,B. Eggleton, G. Cerullo, F. X. Kartner, High-energy pulse synthesis with sub-cycle waveform control for strong-field physics. Nat. Photon. **5**, 475 (2011).

[66] N. Akhmediev, A. Ankiewicz, J. Soto-Crespo,Multisoliton solutions of the complex Ginzburg-Landau equation Phys. Rev. Lett. **79**, 4047 (2000).

[67] M. G. Clerc, S. Coulibaly, L. Gordillo, N. Mujica, R. Navarro, Coalescence cascade of dissipative solitons in parametrically driven systems, Phys. Rev. E **84**, 036205 (2011).

[68] J. Jang, M. Erkintalo, S. Murdoch, S. Coen, Writing and erasing of temporal cavity solitons by direct phase modulation of the cavity driving field. arXiv **1501**.05289 (2015).

[69] S. Wabnitz, Suppression of interactions in a phase-locked soliton optical memory. Optics. Lett. **18**, 601 (1993).

[70] H.Rong, R. Jones, A. Liu, O. Cohen, D. Hak, A. Fang, M. Paniccia *et al.*, A continuous-wave Raman silicon laser, Nature., **433**, 725 (2005).

[71] G. T. Reed, G. Mashanovich, F. Y. Gardes, D. J. Thomson, Silicon optical modulators, Nat. Photon. **4,** 518 (2010).

[72] A. Martinez, J. Blasco, P. Sanchis, J. V. Galn, J. Garca-Ruprez, E. Jordana, P. Gautier, Y. Lebour, S. Hernndez, R. Spano, R. Guider, N. Daldosso, B. Garrido, J. M. Fedeli, L. Pavesi and J. Marti, Ultrafast all-optical switching in a silicon-nanocrystal-based silicon slot waveguide at telecom wavelengths, Nano Lett. **10,** 1506 (2010).

[73] M. Belotti, M. Galli, D. Gerace, L. C. Andreani, G. Guizzetti, A. R. Md Zain, N. P. Johnson, M. Sorel, and R. M. De La Rue, All-optical switching in silicon-on-insulator photonic wire nanocavities, Opt. Express **18,** 1450 (2010).

[74] B. E. Little and Sai T. Chu, W. Pan, Y. Kokubun, Microring Resonator Arrays for VLSI Photonics, IEEE Photon. Tech. Lett. **12**, 636 (2000).

[75] D. R. Solli, P. Koonath, and B. Jalali, Inverse Raman scattering in silicon: A free-carrier enhanced effect, Phys. Rev. A **79,** 053853 (2009).

[76] Y.-P. Huang and P. Kumar, Interaction-free all-optical switching in $\chi^{(2)}$ microdisks for quantum applications, Opt. Lett. **35,** 2376 (2010)

[77] Y. H. Wen, O. Kuzucu, T. Hou, M. Lipson, A. Gaeta, All-optical switching of a single resonance in silicon ring resonators Opt. Lett. **36**, 1413 (2011).

[78] B. E. Little, H. A. Haus, J. S. Foresi, L. C. Kimerling, E. P. Ippen, D. J. Ripin, Wavelength switching and routing using absorption and resonance, IEEE Photon. Tech. Lett. **10**, 816 (1998).

[79] W. Wan, Y. Chong,L. Ge, H. Noh, A. Stone, H. Cao, Time-Reversed Lasing and Interferometric Control of Absorption, Science **331**, 889 (2011).

[80] N. Erez, G.Gordon, M. Nest, G. Kurizki, Thermodynamic control by frequent quantum measurements, Nature **452**, 724 (2008).

[81] Z. R. Claps, D. Dimitropoulos, V. Raghunathan, Y. Han, and B. Jalali, Observation of stimulated Raman amplification in silicon waveguides, Opt. Express. **11,** 1731 (2003).

[82] H. K. Tsang and Y. Liu, Nonlinear optical properties of silicon waveguides, Semicond. Sci. Technol. **23,** 064007 (2007).

[83] S. Xiao, M. H. Khan, H. Shen, M. Qi, Compact silicon microring resonators with ultra-low propagation loss in the C band, Opt. Express **15,** 14467 (2007).

[84] A. C. Turner-Foster, M. A. Foster, J S. Levy, C. B. Poitras, R. Salem, A. L. Gaeta, and M. Lipson,

[85] R. Soref, B. Bennett, Electrooptical effects in silicon, IEEE J. Quant. Electron. **23**, 123 (1987).

[86] A. Yariv, Critical Coupling and Its Control in Optical Waveguide-Ring Resonator Systems, IEEE Phot. Tech. Lett., **14**, 483 (2002)

[87] D. Dimitropoulos, B. Houshmand, R. Claps, B. Jalali , Coupled-mode theory of the Raman effect in silicon-on-insulator waveguides, Opt. Lett. **28**, 1954 (2011).

[88] L.-W. Luo, S. Gustavo, J. Cardenas, M. Lipson, High quality factor etchless silicon photonic ring resonators, Opt. Express **19**, 6284 (2011).

[89] S. Maniptruni, K. Preston, L. Chen, M. Lipson, Ultra-low voltage, ultrasmall mode volume silicon microring modulator, Opt. Express **18**, 16858 (2010).

[90] J. Bernu, S. Delglise, C. Sayrin, S. Kuhr, I. Dotsenko, M. Brune, J. M. Raimond, S. Haroche, Freezing Coherent Field Growth in a Cavity by the Quantum Zeno Effect, Phys. Rev. Lett **101**, 180402 (2008).

[91] M. C. Fischer, B. Gutirrez-Medina, M. G. Raizen, Observation of the Quantum Zeno and Anti-Zeno Effects in an Unstable System, Phys. Rev. Lett **87**, 040402 (2001)

[92] Y. Chembo, C. Menyuk, Spatiotemporal Lugiato-Lefever formalism for Kerr-comb generation in whispering-gallery-mode resonators, Phys. Rev. A **87**, 053852 (2013)